High-Resolution Optoelectronic and Photogrammetric 3-D Surface Geometry Acquisition and Analysis

Thesis by

Wen-Jean Hsueh

In Partial Fulfillment of the Requirements

for the Degree of

Doctor of Philosophy

California Institute of Technology

Pasadena, California

1993

(Defended May 19, 1993)

Acknowledgments

I would like to express my deepest gratitude to my advisor Professor Erik Antonsson for giving me an enjoyable project to work on, for the many discussions regarding the directions of this work, and for allowing me to explore these topics at my own pace. I am also grateful to him for the evaluation and review of this thesis. In addition to providing me with technical insights, he has given me valuable instructions on the process of conducting academic research and the oral and written communication of ideas. I thank him for being a supportive advisor who has constantly given me encouragement. Had it not been for him, none of this would have been possible.

I am grateful to my examining committee: Professor Joel Burdick for his suggestions on this thesis and informative robotics classes throughout the years; Professor Fred Culick for his helpful comments and insights on this thesis; Professor Gerard Medioni of U.S.C. for his generosity in letting me scan the Renault part and use his equipment, and for his valuable advice in the data analysis; Professor Pietro Perona for spending time listening to the state of my research, and giving me helpful suggestions as a computer vision expert.

I offer my gratitude to Professor Suming Chen of National Taiwan University. He led me into the world of engineering research and encouraged me to go on.

Many thanks to Beth McKenney for her invaluable suggestions and help in the lab, for proofreading this thesis, and for being a wonderful officemate and a dear friend. Thanks to Yang Chen of U.S.C. for his patience in explaining his algorithms, and his help in processing my data. I also want to thank my fellow graduate students Doug, Kevin, Shu-San, I-Ming, Andy, Ted, and Will, and the resourceful staff Cecilia, Jackie, Dana, and Charmaine of

Thomas Lab. Their friendship and help maintained my sanity and vigor.

I owe much to my parents Erh-Yih and Yun-Shu. The education they provided me and their constant encouragement in pursuing academic achievement have made me what I am. They are always the source of my strength. How can I ever thank them enough? This thesis is dedicated to them. I also want to thank Chien-Li and Shi-Jean for the support from dearest siblings.

Without the continuous challenging brain storming from the physicist Chung-Yu Mou, who happens to be my spouse, I would have stayed longer in the dark and struggled harder to finish. He has spent these most difficult yet most creative years breathing with me, putting me through every difficult moment, and giving me all the support I needed. Chung-Yu, how can I ever done it without you? Our life together begins at Caltech, which for us has been a wonderful academic and living environment that nurtures both academic insights and love.

This material and the work it represents were made possible, in part, by the following: The Institute for Manufacturing and Automation Research (IMAR), which is an NSF Industry-University Cooperative Research Center, Grant No. CDR-8717322; IBM-Caltech Cooperative Research Fund; The Caltech Program in Advanced Technologies, sponsored by Aerojet General, General Motors Corporation, and TRW; An IBM Faculty Development Award for Dr. Antonsson; The Xerox Corporation; The Ford Motor Company; and The National Science Foundation under a Presidential Young Investigator Award for Dr. Antonsson, Grant No. DMC-8552695. Any opinions, findings, conclusions, or recommendations expressed in this publication are my own and do not necessarily reflect the views of the sponsors.

Abstract

A high-resolution, high-speed, automatic, and non-contact 3-D surface geometry measuring system has been developed. It is based on a photogrammetric and optoelectronic technique that adopts lateral-photoeffect diode detectors sensitive in the near-infrared range. Two cameras in stereo positions are both equipped with the large 2-axis analog detectors. A light beam is focused and scanned onto the surface of an object as a very small light spot. Excitations on detectors generated by the reflected light from the spot create photocurrents that are transformed into 2-D position signals in a very short time. A simple set of calculations is done to photogrammetrically triangulate two sets of 2-D coordinates from the detectors into the 3-D coordinates of the light spot. Because only one small light spot in the scene is illuminated at a time, the stereo-correspondence problem is solved in real time. The detectors are able to collect data at 10 KHz with 4,096×4,096 resolution based on a 12-bit A/D converter. The resolution and precision can be improved up to eight times by oversampling. The system is able to resolve, for example, less than 10 μm from 47 cm away with a nominal viewing volume of $(22\ \text{cm})^3$. Its performance is better than contemporary coordinate measuring, range finding, shape digitizing, and machine vision systems, and is comparable to the best aspects of each existing system. The irregular 3-D data it generates can be regularized so that data processing algorithms designed for image systems may be applied. The system is designed for the acquisitions of general surface geometries, such as fabricated parts, machined surfaces, biological surfaces, and deformed parts. The system will be useful in solving a variety of 3-D surface geometry measuring problems in engineering design, manufacturing, inspection, robot kinematics measurement, and vision.

Contents

List of Figures

List of Tables

Chapter 1

Introduction

1.1 Motivation

Three dimensional surface geometry measurement is important for a wide variety of applications. Several classes of macroscopic problems, such as long-distance landscape via radar, and earth surface elevation via satellite laser altimeters, are well-solved. Microscopic problems, such as accurately and rapidly determining the surface geometry of a numerically machined part without contact, however, are not well solved.

Contemporary commercial coordinate measuring machines (CMM) [12, 20] use mechanical profilometers with styli in contact with the object surface. The resolution may approach 1 μm (0.00004 in) and accuracy close to 10 μm (0.0004 in). They are helpful in measuring deep cavities of an object. A portable one [20] facilitates the inspection of giant surfaces such as those of an airplane. Detailed performance evaluation methods for CMM can be found in [7]. Nevertheless, there are plenty of situations where no contact with the object is desired, especially when contact will damage the surface microscopically. In addition, CMMs usually have to be programmed and attended by experienced operators, so automaticity is

hard to achieve.

Researchers have been developing non-contact techniques for range finding in the field of computer vision for many years. Jarvis [30] published a detailed review, in which ten kinds of methods were discussed: striped lighting or grid coding, relative range from occlusion cues, depth from texture gradient, focusing, surface orientation from image brightness, stereo disparity, camera motion, moiré fringe range contours, simple triangulation, and time-of-flight range finders including ultrasonic, laser, and streak camera technologies. He commented that all methods appeared to have one or more of the following drawbacks: missing parts, computational complexity, time-consuming in improvement of signal/noise ratio, limited to indoor application, limited to highly textured or line structured scenes, limited surface orientation, and limited spatial resolution. He also remarked that from the view point of simplicity, it is hard to improve upon triangulation schemes involving one point at a time, and in terms of potential, it would seem that direct laser time-of-flight range finders could, in theory, eliminate all the above problems provided an intense enough energy source could be available. He stressed that capturing the third dimension through non-image-based range finding is of great utility in 3-D scene analysis, since many of the ambiguities of interpretation arising from occasional lack of correspondence between object boundaries and inhomogeneities of intensity, texture, and color can thus be trivially resolved.

Image-based systems are not only extensively used in computer vision, but also have been adopted for surface inspection. The use of video or charge-coupled-device (CCD) cameras to inspect the surface of a rotating/translating part has been studied and commercialized for many years. There are models with color ability [15] or acquiring 2-D and 3-D images

at the same time [41]. Some use ordinary indoor lighting for illumination. Some project a structured line/plane of light [15] onto the object to determine the geometries of silhouettes. Some generate moiré patterns to help CCD cameras determine surface shapes. Others measure individual surface points one by one while a laser beam is focused [34] and/or scanned [19, 41] onto the object. The above systems either do not resolve less than 0.001 in (25 μm) or have small stand-off distances (distances between the camera and the object to be measured) while maintaining 0.001-in resolution at a lower speed.

Several manufacturers [48, 53, 54] developed non-contact systems that measure microns, sub-microns or even nanometers using microscopy technology. Because those systems are mainly designed for measuring surface profiles, the viewing range is limited at the order of hundreds of microns and the stand-off distance is in millimeters, although the resolution is from 0.1 to 0.01 μm (0.4×10^{-6} in).

Scheffer [44] proposed that requirements for a measuring instrument suitable for robot surveying, calibration and control are high accuracy ($\pm$0.1 or $\pm$0.15 mm/ 5 m) and resolution (0.1 or 0.01 mm), broad measuring volume (0.3 m^3 – several or dozens of m^3), non-contacting and portability. Therefore, when it comes to measuring with resolution on the order of 10 μm (0.0004 in) at a comparatively large stand-off distance — in tens or hundreds of centimeters — without contact, prior to the research reported in this thesis there has not been a satisfactory system. Under many conditions, in manufacturing for instance, a minimum stand-off distance cannot be compromised.

A 3-D surface geometry acquisition system (to be referred to as "the SGA system") based on an optoelectronic and photogrammetric technique is developed in this thesis research. It is based on a pair of 2-axis large linear-area lateral-photoeffect diode (LPED) detectors,

and is found to present a substantial improvement over previous methods in resolution, repeatability, and automaticity at comparatively larger stand-off distances.

Besl [8] has compared 59 different range measurement systems. According to the figure of merit he defined, the performance of the SGA system is found to be comparable to the best aspects of each system, while maintaining high repeatability and high speed at the same time, which is not achievable by other systems. (Appendix A).

1.2 Approach

An optoelectronic photogrammetric system to measure the spatial kinematic histories of human motion with 6 degrees of freedom has long been developed and studied at MIT [3, 37]. The system measures the spatial locations of actively illuminated LED markers worn on a human. Three or more markers in a rigid array on each link permit the position and orientation of an embedded body coordinate system to be determined from the individual marker locations. The markers are illuminated one at a time for the stereo LPED detectors to measure the image plane coordinates and then a photogrammetric triangulation is done by the computer to find the 3-D coordinates. Because of the nature of photodiode detectors (see Chapter 2), image plane coordinates are acquired in real time as compared to the time required to scan through every pixel of a CCD camera.

This system is ideal for measuring general 3-D coordinates of a single light spot. Exploiting its non-contact, fast, high-precision advantages, the use of a laser source with scanning devices is proposed by Antonsson [4, 5] to construct a system that measures in stereo the 3-D surface geometry of a stationary object.

The discovery of the physical principle of lateral photoeffect (to be described in Section 2.2) goes back to the original work of Schottky [45] in 1930. Wallmark [50] first recognized the possibility of measuring the position of a light spot on the sensor surface in 1957, and suggested that the detection limit set by the noise of the cell for a light spot movement on the diode could be 0.01 $\mathring{A}$. It is now well-understood and has been analyzed by various authors [1, 2, 11, 14, 17, 23, 24, 25, 29, 35, 52]. Applications of LPED detectors in optical alignment systems [27], remote machine control [32], and human movement tracking [51] were proposed in the 1970's. Light-weight structure deformation measurement (according to [33]) and remote measurement of robot trajectory motion [16] were proposed in the 1980's.

Not until 1981 was the application of LPED to non-contact 3-D ranging devices [31] proposed, but only one detector was used, and the triangulation depended highly on the accuracy of scanners. By adopting a photogrammetric system with two cameras [5], the 3-D reconstruction is only a function of the camera separation and the binocular convergence angles, which are static.

1.3 Applications

The SGA system will be useful in general 3-D surface geometry determinations. Manufactured parts, failed parts, and in-process dimensional inspection problems in manufacturing may be solved with higher resolution at larger stand-off distances. Manufacturers of ceramic computer chips and medicine tablets have shown interests in the SGA system because it can help spot defects early in the manufacturing processes. It may also provide real-time

feedback for adaptive control of CNC machines. In CAD/CAM, precise and fast geometry acquisition of existing parts helps to build a data base for reverse engineering, thus prototyping can be minimal, and various design possibilities can be explored. Other potential applications include robot vision and kinematics measurement.

In fundamental research, it finds applications in fracture mechanics investigations, where precise determination of surface geometry in the near-crack-tip region is critical for increasing the understanding of fracture, and in computational fluid dynamics, where due to the ever increasing complexity of geometries being analyzed, surface topology has become a critical issue for volume grid generation [38].

1.4 Outline

This thesis introduces the SGA system by first describing the apparatus and design concepts in Chapter 2, then explaining its characteristics and performance in Chapter 3. Chapter 4 is devoted to the detailed findings from the calibrations of the SGA systems. Chapter 5 shows the data acquisition results, explains how they are acquired, records work done for the problems of merging and registration of multiple views, and proposes related work to be done in the future. Chapter 6 summarizes and provides an outlook for the system. Appendix A shows comparisons between this system and others. Appendix B clarifies motions of the rotary table and the goniometer. Appendix C displays error maps of one of the cameras not included in Chapter 4. Appendix D is a glossary.

Chapter 2

Apparatus

The SGA system consists of four parts: an optical system, two cameras, a real time computer system, and a two-axis positioning system. Figure 2-1 illustrates the overall scheme and Figure 2-2 shows the system in more detail.

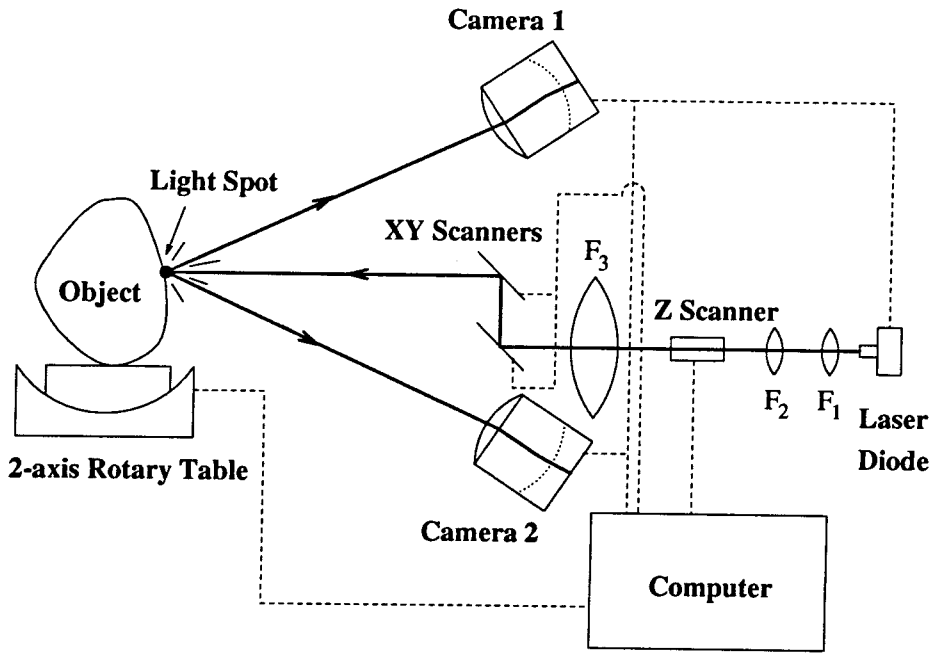

Figure 2-1: Overall scheme

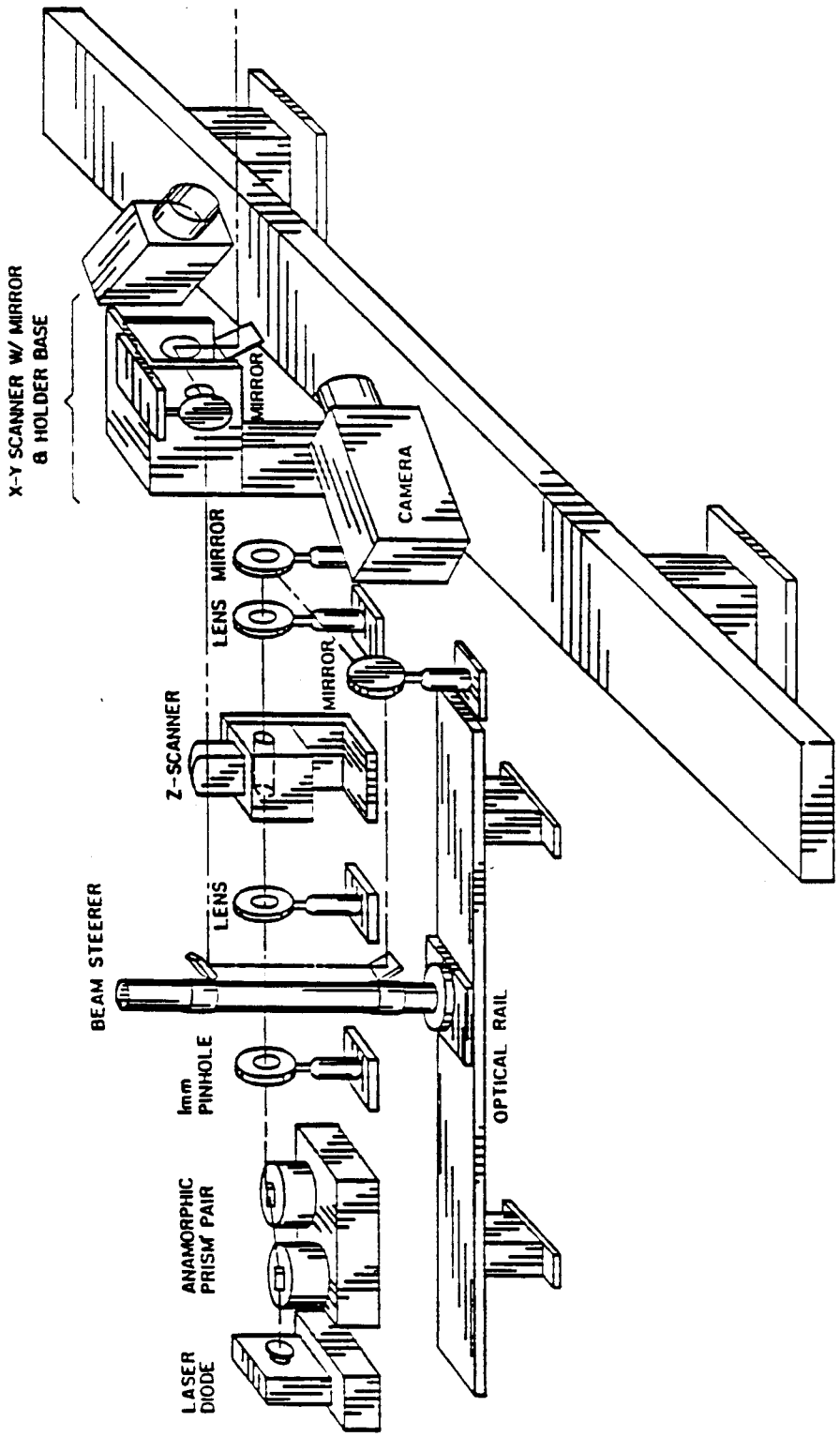

Figure 2-2: 3-D sketch of the system, modified from [5]

- Optical System Specifications
  - An 850-nm, 40-mW near-infrared diode laser.[1]
  - Focusing lenses. The design of the optical setup is based on [36].
  - X/Y-direction step galvanometer scanners[2] with 20-Hz scanning rate, ± 20° projection angles.
  - Z-direction lens translator,[3] also called Z scanner in the following text.
- Camera Specifications
  - Two cameras[4] with f:1.0 50-mm lenses. The viewing angle is 30°.
  - A 24×24 mm^2 active area two-axis lateral-photoeffect diode (LPED) detector[5] with a 12-bit A/D converter (i.e., 4,096×4,096 resolution) mounted on the focal plane of each camera. Its peak performance occurs at wavelength = 940 nm.
  - Analog signals of intensities are digitized from 0 to 15.
  - A feedback system on each camera controls the intensity of the light source and amplitude-modulates it at 10 KHz with a 40% duty cycle.
  - A thermistor is positioned close to each detector to monitor the variation in temperature.
- Computer Specifications

[1] LiCONiX Diolite 800-40, Santa Clara, California 95054
[2] General Scanning DX2103/XY2030, Watertown, Massachusetts 02172
[3] General Scanning DX1100/LT1320
[4] Selcom SELSPOT II, Detroit, Michigan 48226
[5] SiTek 2L24, Partille, Sweden

- Real-time data acquisition and task scheduling.[6]
- File server.[7]

- Positioning System Specifications
  - A 360° rotary table, resolution = 0.001°.[8]
  - A ±45° goniometer, resolution = 0.001°.[9]
  - The rotary table and the goniometer are mounted such that their axes of rotation intersect each other and are perpendicular. The mounting error is less than 0.001°.

2.1 Overview

An infrared diode laser beam is focused by optics and scanned by the XY and Z scanners onto the surface of an object, and a very small[10] light spot is generated. The diffuse reflected light from the spot is then collected by the lenses of both cameras and focused onto the detectors. The detectors are lateral-photoeffect diodes (LPED), which will be described in detail in Section 2.2. The camera system modulates the laser beam into a pulse train at 10 KHz, while the feedback from the cameras controls the intensity of the beam. Synchronously, the detectors take turns measuring the 2-D position of the spot on the

[6]Heurikon HK68/V2FA microcomputer with MC68020 MPU, Madison, Wisconsin 53713; VxWorks 5.0 real-time operating system, Alameda, California 94501

[7]Sun Sparc station, Mountain View, California 94043

[8]KLiNGER RT120PP, Garden City, New York 11530

[9]KLiNGER BG160PP

[10]To get resolution at the order of 10 μm, the diameter of the spot should be equal to or less than 10 μm. Due to the lack of a beam size measuring device while designing and testing the optical system, the size of the spot was found to be more than 100 μm when a device was finally available for the diameter of the beam to be measured shortly before this thesis was written.

image plane at a speed of 10,000 samples/sec. The 2-D azimuth and elevation information of the spot on the image planes are sent to the computer. Knowing the locations and orientations of the two cameras and their intrinsic calibration error maps, the computer performs a photogrammetric triangulation reconstruction to determine the 3-D coordinates of the spot on the object. The scanners can then move the beam to a new location in X or Y direction, and the cycle is repeated as many times as the programmer would like. This way a detailed 3-D data map can be generated for the surface from this specific viewing angle. The object sits on a 2-axis rotary table system so all sides, except for the bottom, may be presented to the cameras, as required. By rotating the object, several data maps can be acquired, one for each viewing angle. Registering and merging all maps together gives an overall description of the object.

2.2 The Detectors

The application of LPED detectors in stereo to measure the shape of an object is what distinguishes this system from others. The detector is a monolithic silicon diode with two axes and a large linear area. Although the popular term "image plane" is adopted here to describe the detector plane, the detector does not detect an "image," in the usual sense. Only the location of the single pulsed infrared light spot is detected.

In Figure 2-3, u and v are the image plane coordinates. When a light beam hits the diode, it induces photocurrents on the four electrodes that can be approximated by

$$\frac{I_{u1}}{I_{u1}+I_{u2}} = \frac{\frac{L}{2}+u}{L}, \qquad \frac{I_{v1}}{I_{v1}+I_{v2}} = \frac{\frac{L}{2}+v}{L}. \tag{2.1}$$

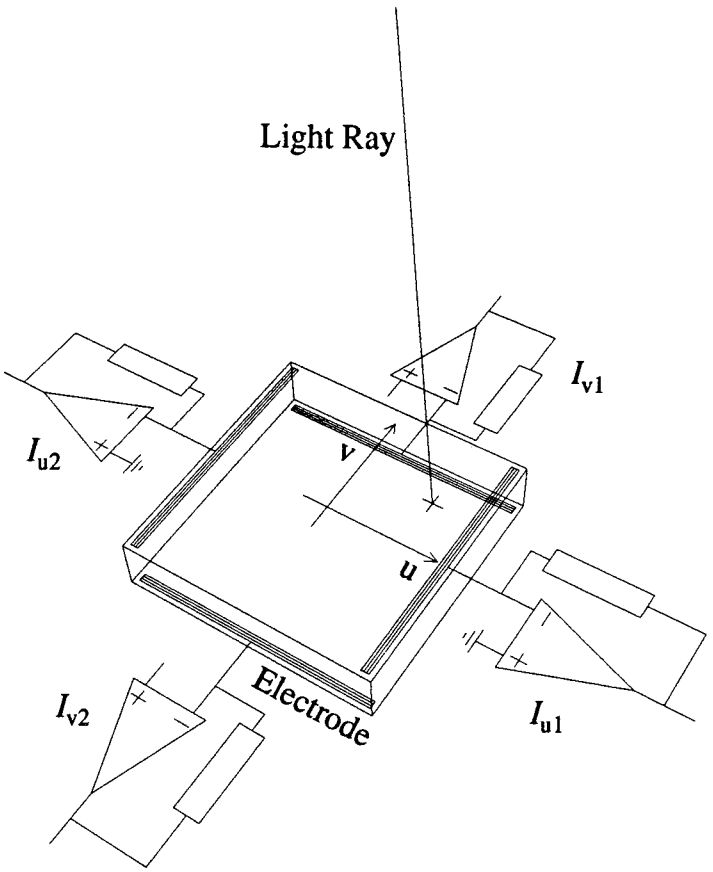

Figure 2-3: Lateral-photoeffect diode (LPED) detector

The position of the light spot is thus determined by

$$\mathrm{u} = \frac{L}{2} \cdot \frac{I_{\mathrm{u1}} - I_{\mathrm{u2}}}{I_{u1} + I_{\mathrm{u2}}}, \qquad \mathrm{v} = \frac{L}{2} \cdot \frac{I_{\mathrm{v1}} - I_{\mathrm{v2}}}{I_{\mathrm{v1}} + I_{\mathrm{v2}}}, \tag{2.2}$$

where L is the dimension of the diode and I's are the currents measured at the electrodes [35]. An important feature here is that what is measured is the position of the intensity weighted centroid of the spot. The analog currents are converted to analog voltages and then are fed into a 12-bit A/D converter where the signals are digitized from 0 to 4,095

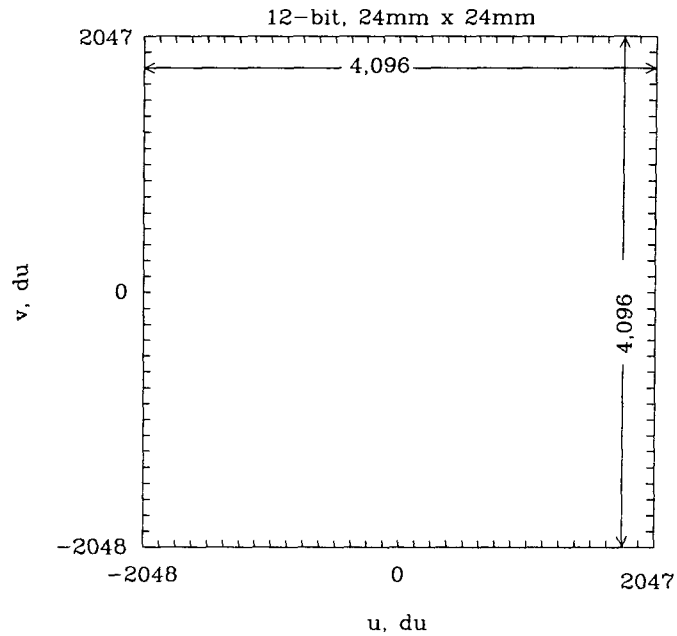

Figure 2-4: Detector units (du)

"detector units (du),"[11] as in Figure 2-4. These discrete units, however, are not "physically" on the detector. The 2-D digital signals from both detectors are then processed by the computer and are converted into 3-D world coordinates of the light spot.

In LPED detectors, the induced photocurrents are collected in a very short time (50 – 100 μsec) compared to the time required to scan through every pixel on a CCD camera. An analog system does not have intrinsic resolution. The resolution is basically determined by the noise of the system and the A/D converter. Because only one spot in the scene is illuminated with the laser at a time, oversampling can be adopted easily to reduce noise. Moreover, this system essentially solves the stereo-correspondence problem in real time, so

[11]The digital signal coming out from the A/D converter is between 0 and 4,095. It is then offset by the computer to range from −2,048 to 2,047, which matches Equation 2.2 and the image plane coordinate system.

there is no need for a complicated image matching process. Focusing optics are not needed for the incoming light because what is measured is the position of the intensity weighted centroid of the spot.

Error analysis of the LPED has been discussed in many references. The linear relationship for currents in (2.1) is the exact limit of

$$\frac{I_{u1}}{I_{u1}+I_{u2}} = \frac{\sinh[a(\frac{L}{2}+u)]}{\sinh(aL)}, \qquad \frac{I_{v1}}{I_{v1}+I_{v2}} = \frac{\sinh[a(\frac{L}{2}+v)]}{\sinh(aL)},$$

as a, the fall-off parameter [35], approaches 0. Therefore, very small a is a characteristic of high-quality LPED that assures good linearity. a is determined by intrinsic physical conditions of the diode such as current density, thickness, resistivity, and temperature, and can vary from location to location on the diode. Generally speaking, this nonlinearity gets stronger towards the sides and corners on the diode. Error also can be caused by disturbances in intensity and reflection. Nonlinearities in electronics and signal noise can contribute to stochastic error [18]. A detailed error analysis can be found in [33]. The influence of intensity was studied carefully in [37].

An intrinsic camera calibration helps to reduce the error caused by nonlinearities in the diode (Chapter 4). It is found that oversampling helps to reduce the error significantly (Section 3.3.2). A "warm-up" effect is described in Section 3.5, and a solution is presented.

2.3 3-D Photogrammetric Triangulation Reconstruction

Photogrammetric triangulation transforms the two 2-D image plane coordinates into one set of 3-D world coordinates.

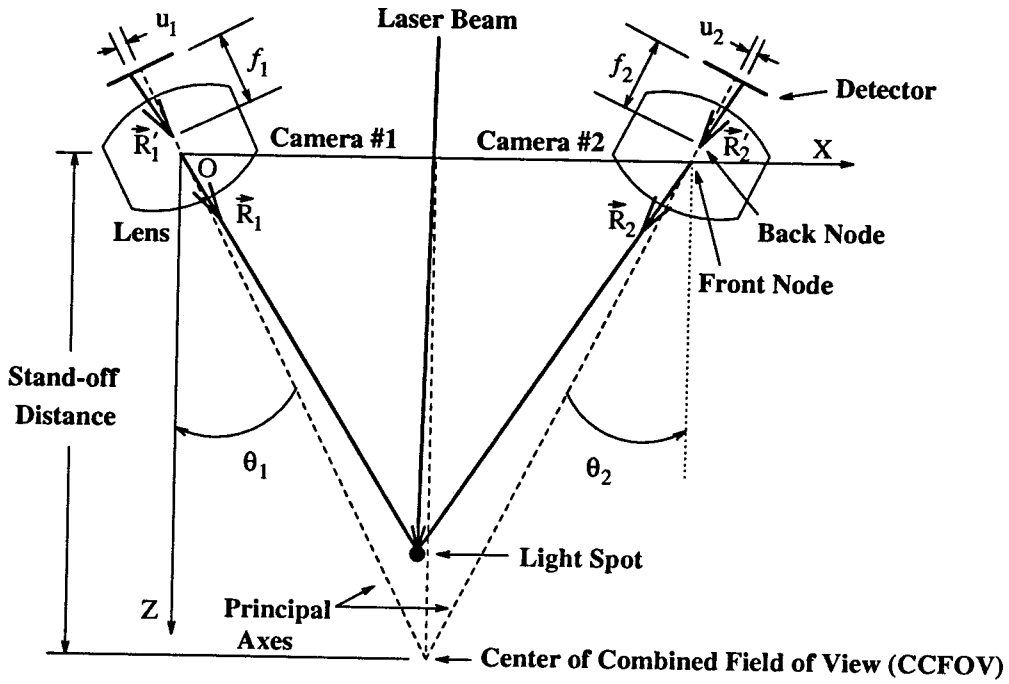

Figure 2-5: Configuration of two cameras, where $-\theta_1 = \theta_2 = \tan^{-1}(\frac{1}{2})$. *Y-axis sticks vertically out of the paper.*

Figure 2-5 is a plan view of the system. The origin of the world coordinate system is set at the front node of the lens of camera #1. The X axis passes through the front node of the lens of camera #2. The Y axis sticks out of the paper vertically. The Z axis is positive in the direction of the laser beam. The v-axis of the detector is assumed to be parallel to the world Y-axis (though this requirement can easily be relaxed). The intersection of the two principal axes is called "center of combined field of view" (CCFOV) here. f:1.0 lenses are used to collect as much light as possible, giving each camera a 30° viewing angle. The binocular convergence angles θ_1 and θ_2 are set to be equal in quantity but opposite in signs. They are set by making the inter-camera spacing equal to the stand-off distance (the distance between the X-axis and the CCFOV), that is, $-\theta_1 = \theta_2 = \tan^{-1}(\frac{1}{2})$. The distances between back nodes of the lenses and the detectors are the principal distances f_1

and f_2. The cameras were assembled such that f_1 and f_2 are as close to the focal distances of the lenses as possible. The 2-D coordinates measured on the image planes are (u_1,v_1) and (u_2,v_2) in the detectors' own coordinate systems. v_1 and v_2 are not shown in Figure 2-5 because they are parallel to the Y-axis.

Knowing the principal distances f_1 and f_2, (u_1,v_1) and (u_2,v_2) can be transformed into vectors $\vec{R}_1$ and $\vec{R}_2$ in world coordinate system with

$$\vec{R}_1 = \mathcal{M}_1 \vec{R}'_1, \qquad \vec{R}_2 = \mathcal{M}_2 \vec{R}'_2,$$

where

$$\mathcal{M}_1 = \begin{bmatrix} cos\theta_1 & 0 & -sin\theta_1 \\ 0 & 1 & 0 \\ sin\theta_1 & 0 & cos\theta_1 \end{bmatrix}, \quad \mathcal{M}_2 = \begin{bmatrix} cos\theta_2 & 0 & -sin\theta_2 \\ 0 & 1 & 0 \\ sin\theta_2 & 0 & cos\theta_2 \end{bmatrix},$$

and $\vec{R}'_1$ and $\vec{R}'_2$ are in the detector coordinate systems:

$$\vec{R}'_1 = \begin{Bmatrix} u_1 \\ v_1 \\ f_1 \end{Bmatrix} \text{ and } \vec{R}'_2 = \begin{Bmatrix} u_2 \\ v_2 \\ f_2 \end{Bmatrix}.$$

Figure 2-6 is a 3-D sketch which demonstrates the triangulation.

In principle, extensions of $\vec{R}_1$ and $\vec{R}_2$ should intersect each other because they are directions of light rays that come from the same light spot located at $\vec{p}$. In practice, any misalignment or error in the system can result in skew. $\vec{e}$ is defined to be the skew vector such that $|\vec{e}|$ is the shortest distance between the two lines (Figure 2-6).

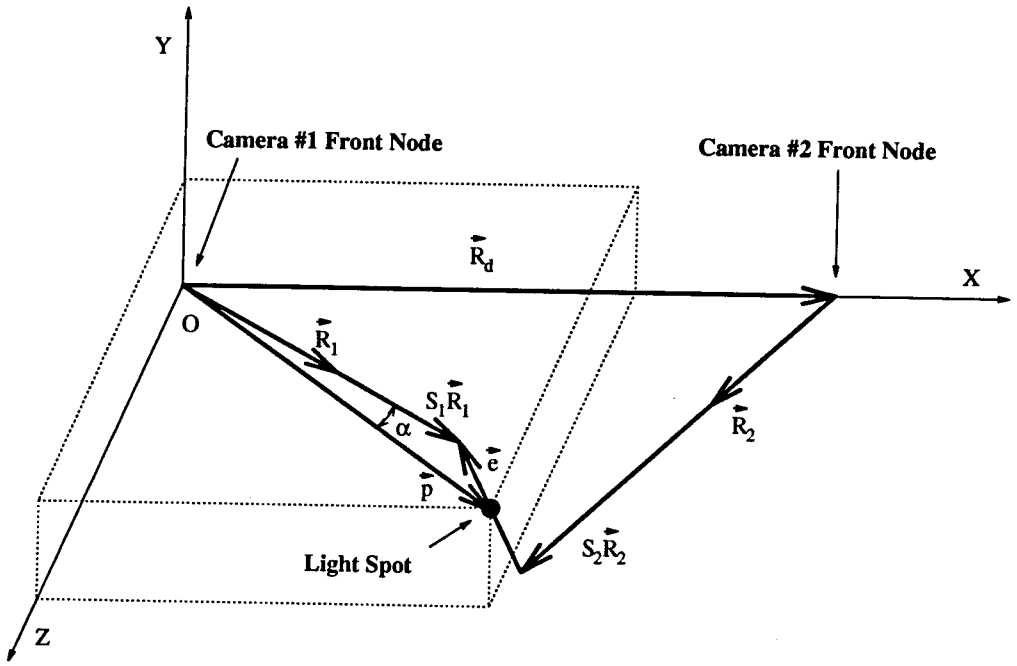

Figure 2-6: Photogrammetric triangulation reconstruction

In order to find $\vec{e}$, we define

$$\vec{e}(S_1, S_2) = S_1\vec{R}_1 - S_2\vec{R}_2 - \vec{R}_d. \tag{2.3}$$

Minimizing $|\vec{e}(S_1, S_2)|$ with respect to S_1 and S_2 gives

$$S_1 = \frac{(\vec{R}_d \cdot \vec{R}_2)(\vec{R}_1 \cdot \vec{R}_2) - (\vec{R}_d \cdot \vec{R}_1)(\vec{R}_2 \cdot \vec{R}_2)}{(\vec{R}_1 \cdot \vec{R}_1)(\vec{R}_2 \cdot \vec{R}_2) - (\vec{R}_1 \cdot \vec{R}_2)(\vec{R}_1 \cdot \vec{R}_2)},$$

$$S_2 = \frac{(\vec{R}_d \cdot \vec{R}_2)(\vec{R}_1 \cdot \vec{R}_1) - (\vec{R}_d \cdot \vec{R}_1)(\vec{R}_1 \cdot \vec{R}_2)}{(\vec{R}_1 \cdot \vec{R}_1)(\vec{R}_2 \cdot \vec{R}_2) - (\vec{R}_1 \cdot \vec{R}_2)(\vec{R}_1 \cdot \vec{R}_2)}.$$

$\vec{e}$ is thus calculated by Equation 2.3. The coordinates of the spot $\vec{p}$ are defined to be at the center of $\vec{e}$:

$$\vec{p} = \frac{1}{2}(S_1\vec{R}_1 + S_2\vec{R}_2 + \vec{R}_d).$$

The above algorithm is described in [6]. It is simple. Even a relatively modest computer can perform this set of calculations faster than the data is being generated.

To evaluate the quality of the triangulation, a parameter α is introduced

$$\alpha = \frac{|\vec{e}|}{|\vec{p}|},$$

which is the angle between $\vec{R}_1$ and $\vec{p}$ when $|\vec{e}| \ll |\vec{p}|$. If α is too large, there is too much noise present in the measurement, so the data should be disregarded. The noise may come from unwanted reflections, or arises because one or both of the cameras do not get enough light intensity to make accurate measurements.

To decide the appropriate tolerance for α, several experiments were conducted to gather empirical data. An example is shown in Figure 2-7. When the flat surface of a wooden board is measured, α varies with the position and the surface feature of the spot on the board, but overall it is not larger than 0.005 for a flat wooden board.

An important advantage of the SGA system is its adaptive scanning capability. Since the system can determine the 3-D coordinates of a point anywhere in the combined FOV, and can measure points in any order, it is possible to analyze the data stream from the system during acquisition and adaptively scan the light spot in response. For example, as the light spot is scanned across an object, when it scans pass an edge, the system can recognize this and modify the scan pattern accordingly. With this general approach it will be possible to locate and scan the edges of objects in real time, and also to collect more spatially dense data in regions of interest.

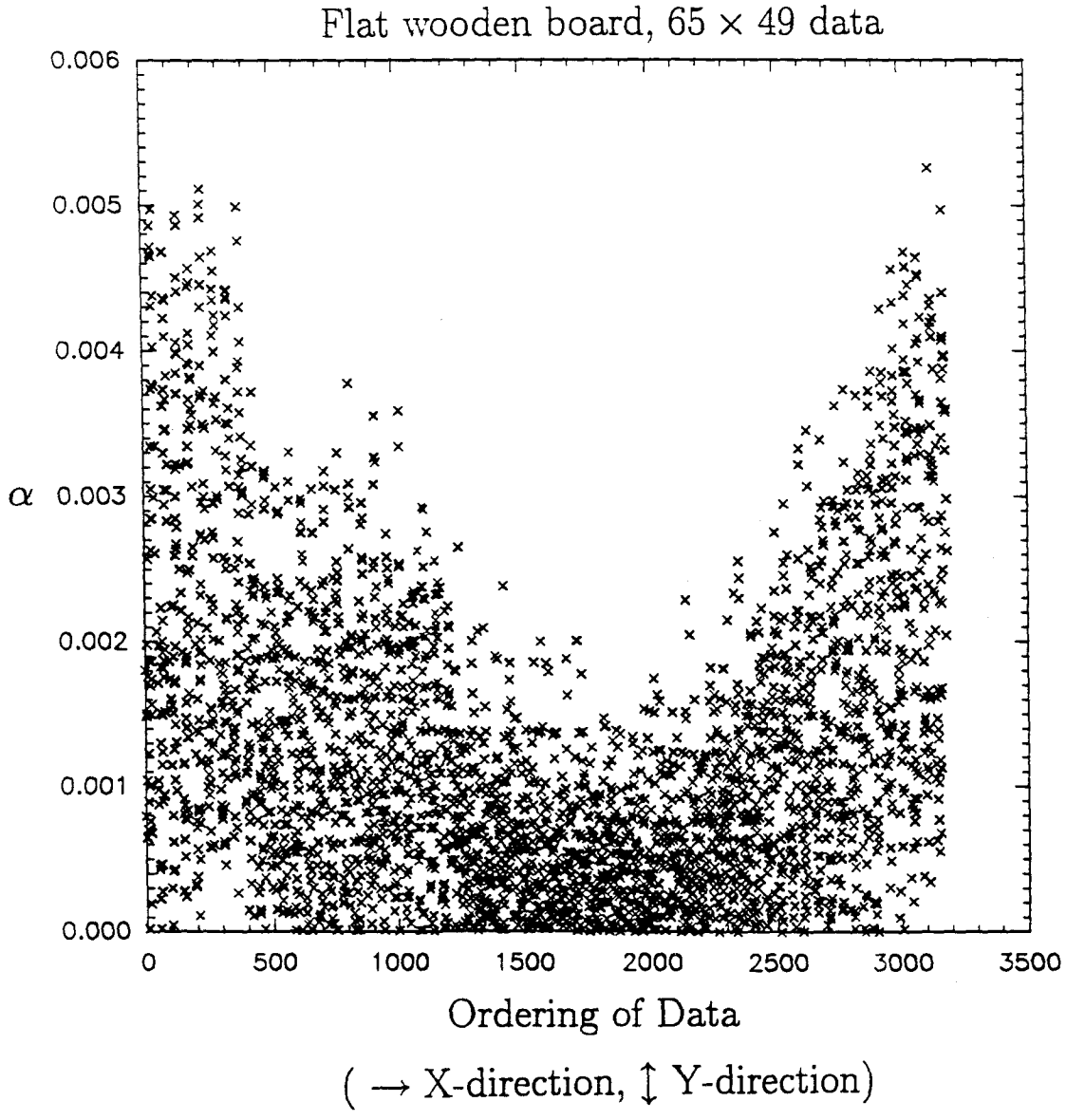

Figure 2-7: Distribution of α

Chapter 3

Characteristics

3.1 Definitions

To clarify the presentation and discussion, relevant terminology is presented below.

3.1.1 Resolution, Repeatability and Accuracy

As it is nicely put in [47], *accuracy* is the "ability to tell the truth". For this application it is the maximum translational or rotational error that can occur when comparing the *measured* quantity to the *desired* quantity in the system's work volume. See Figure 3-1.

Repeatability is the "ability to tell the same story over and over again" [47]. It is the error between a number of successive attempts to measure the same target. One common definition is some constant times the standard deviation of the measurements. Repeatability is defined in this analysis to be the difference between the maximum and the minimum measured values. It can also be called *precision*, but because precision is often mistaken for accuracy, repeatability is used in this thesis to avoid misunderstanding.

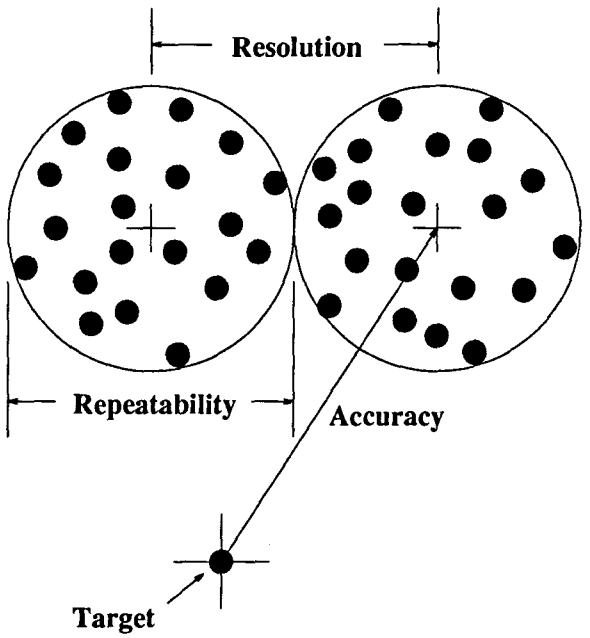

Figure 3-1: Accuracy, repeatability and resolution

Resolution is "how detailed the story is" [47]. It is the smallest step that a system can measure. Resolution gives a lower bound on the repeatability.

Due to the analog feature of LPED described in Section 2.2, oversampling (averaging over multiple samples) is found to be very helpful in improving the resolution of the data. Repeatability and accuracy can thus be improved, too. Some results are discussed in Section 3.2.

A fundamental concern is the following: What is the certainty of the measurements themselves used to characterize the accuracy, resolution and repeatability? A discussion illuminating this question is presented in the following sections.

3.1.2 Speed

An important measure of the system's performance is the *system speed*. It is the number of data points corresponding to different surface locations acquired by the system per second. If higher resolution is desired, system speed often has to be reduced, because more samples have to be taken for averaging for one stationary light spot.

Sampling frequency is the rate at which detectors take measurements. For this application it can be as fast as 10 KHz with a 40% duty cycle. Because two cameras are used sequentially to determine the location of the light spot in order that each one can adjust the intensity of the spot for best measurement, the maximum sampling frequency is half — 5 KHz. They can also be used simultaneously to gain full speed, but the intensity of the light spot will be controlled by one camera only.

The *sampling speed* is the product of the sampling frequency and the number of samples taken for each stationary light spot. It is the basis on which an ideal system speed is decided. Delays in other components of the system can slow down the system speed substantially. This is when a real-time data acquisition and task scheduling computer system comes into play (See Section 5.1.2).

3.1.3 Inter-Camera Spacing and Nominal Viewing Volume

Inter-camera spacing is the distance between front nodes of the two camera lenses. As described in Section 2.3, the binocular convergence angles are customarily $-\theta_1 = \theta_2 = \tan^{-1}(\frac{1}{2})$. Therefore, the system has an inter-camera spacing, $|\vec{R}_d|$, equal to the distance between the X-axis and the CCFOV (Figure 2-5). Because the resolution is at its best at the CCFOV, if an object is located far away from the cameras the inter-camera spacing has

to be as large as the stand-off distance between the cameras and the object in order to get the best resolution.

The cameras' "combined field of view (FOV)" is the volume in which things can be seen by both cameras, as shown in Figure 3-2. It is the intersection of a pair of pyramids, because the shape of the detectors is square. For simplicity, it is sometimes considered to be a cube, called the *nominal viewing volume*, whose sides are approximately half the inter-camera spacing, $|\vec{R}_d|$ / 2. Note that the nominal viewing volume is considerably smaller than the combined FOV.

3.1.4 Nominal System Resolution

Resolution is referred to in two different contexts in this analysis. One is the *detector resolution*, which is 1 du (often referred to as 12-bit resolution according to the A/D converter) if only one sample is collected for each light spot. Also, the field of view of each camera is 30°, as shown in Figure 3-2, thus the detector resolution can also be referred to in degrees (°), which is approximately 30°/4,096 = 0.0073° if only one sample is collected for each light spot. When oversampling is applied, the detector's overall resolution can be improved (Section 3.2). The best resolution achieved by oversampling is about 1/8 du (15-bit resolution) or 0.0009°. Therefore, *detector resolution units* is defined to be the actual integer units that the detector is divided into after oversampling. In the best case it is 4,096×8 = 32,768.

The other resolution is the *nominal system resolution*, which is defined to be the nominal length in the combined FOV per detector resolution unit. Usually, system resolution is specified along the X, Y and Z directions near the CCFOV, as shown in Figure 3-2. Obvi-

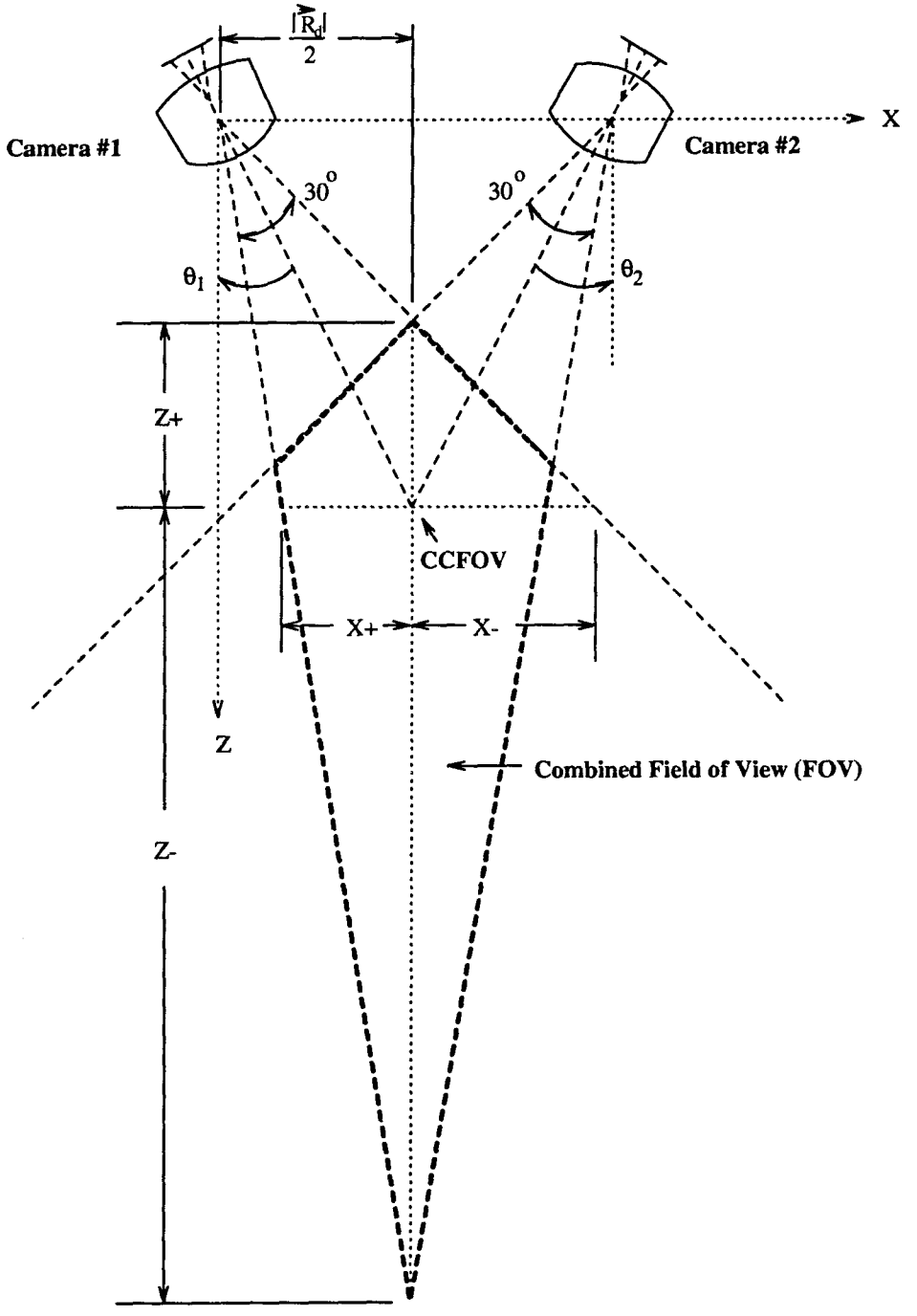

Figure 3-2: Combined FOV and system resolution. Y-axis sticks vertically out of the paper.

ously, the resolutions along X, Y and Z are nonuniformly distributed. For example, both X^+ and X^- correspond to 2,048 du on detector #1 although they are different in length. In this case, one resolution is $X^+/2{,}048$ while the other is $X^-/2{,}048$. Therefore, depending on the location of the spot, the detailed resolutions on all axes may be different.

In order to use a single length scale to characterize the system resolution, the side of the nominal viewing volume, $|\vec{R}_d|/2$, is taken to be the nominal length. As a result, the nominal system resolution is

$$\frac{|\vec{R}_d|/2}{4,096},$$

and is smaller (better) with oversampling.

It can be shown that resolutions in X, Y and Z near CCFOV are usually better than the nominal system resolution, because

$$\frac{|\vec{R}_d|}{2} : X^+ : X^- : Z^+ : Z^- = 1 : 0.59 : 0.77 : 0.87 : 2.92. \tag{3.1}$$

The Y direction is similar to that of X. Because Z^- is usually at the back of the object or cannot usually be seen at the same time by both cameras, it can be neglected.

Since the detector resolution and the nominal system resolution have different units, no confusion will arise. Therefore, no special distinction will be made. For convenience, the nominal system resolution will be simply called *resolution* in following sections. It will be discussed further in Sections 3.2 and 3.3.

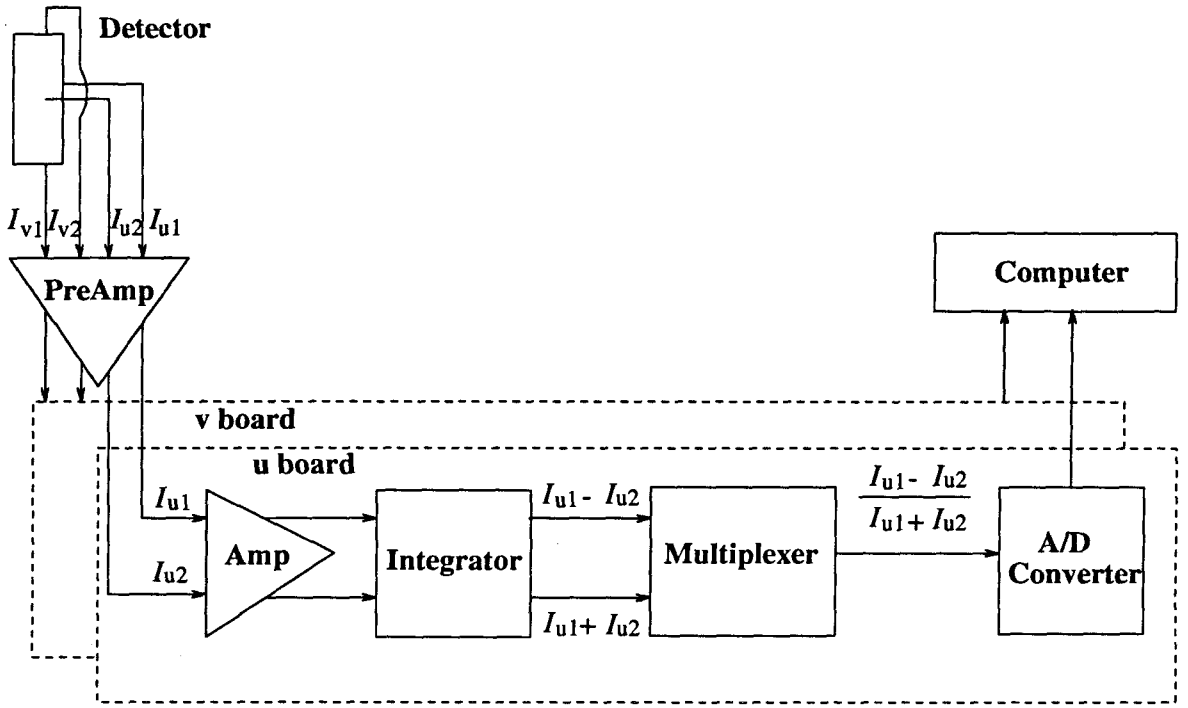

Figure 3-3: Detector signal processing electronics

3.2 Oversampling

As was mentioned in Section 3.1.4, oversampling helps reduce the effects of noise. There is noise coming from the induced currents at the electrodes of diodes. Additionally, there are noises introduced by other sources when the signals are processed by the electronics, as shown schematically in Figure 3-3. Equation 2.2 can thus be modified as

$$\mathrm{u} = \mathrm{Digitize}\left[\frac{L}{2}\cdot\frac{(I_{\mathrm{u1}} \pm n_{\mathrm{u1}} \pm n_{P1} \pm n_{A1}) - (I_{\mathrm{u2}} \pm n_{\mathrm{u2}} \pm n_{P2} \pm n_{A2}) \pm n_{I-}}{(I_{\mathrm{u1}} \pm n_{\mathrm{u1}} \pm n_{P1} \pm n_{A1}) + (I_{\mathrm{u2}} \pm n_{\mathrm{u2}} \pm n_{P2} \pm n_{A2}) \pm n_{I+}} \pm n_{\mathrm{M}}\right] \pm n_{\mathrm{A/D}}, \tag{3.2}$$

where n's are noises introduced by the following:

n_{u1}: detector #1 in u direction, n_{u2}: detector #2 in u direction,

n_{P1}: preamplifier on signal #1, n_{P2}: preamplifier on signal #2,

n_{A1}: amplifier on signal #1, n_{A2}: amplifier on signal #2,

n_{I-}: integrator on subtracting the signals, n_{I+}: integrator on adding the signals,

n_M: multiplexer, and $n_{A/D}$: A/D converter.

v has a similar expression.

Whether oversampling is a fair method to process the digital signals in order to reduce the noise and improve the resolution relies heavily upon the distribution and magnitude of the noise. Equation 3.2 shows that it is very difficult to predict the overall distribution of the digital position signals u and v. Therefore, some data collections are done in order to demonstrate the distribution of overall noise. If the standard deviations are acceptable and the mean values can create finer resolution, then oversampling is regarded as appropriate and useful.

Figure 3-4 shows u and v digital position signal distributions taken from the same stationary light spot projected close to the center of the diode for 1,024 samples. Figure 3-5 shows that there is no apparent time correlation in the time scale of the observation in Figure 3-4.[1] Figure 3-6 shows distributions of a light spot projected away from the center of the diode. Figure 3-7 shows again that no apparent time correlation is present. It is well-known that when the light spot is projected onto locations farther away from the center of the diode, noise increases and the standard deviations go up. The overall noise may not be Gaussian, but the standard deviations are acceptable. Section 3.3.2 will demonstrate how the mean values pick up finer resolution.

Because the analog signals are digitized before they are sent to the computer, a record

[1]The time correlation problem may be examined and calculated further with larger time scale.

of how the analog signals vary when measuring a same stationary spot multiple times is not available, although the variation of digital signals can be recorded. An analog output should be implemented for the detectors in future experiments to provide better understanding of the noise.

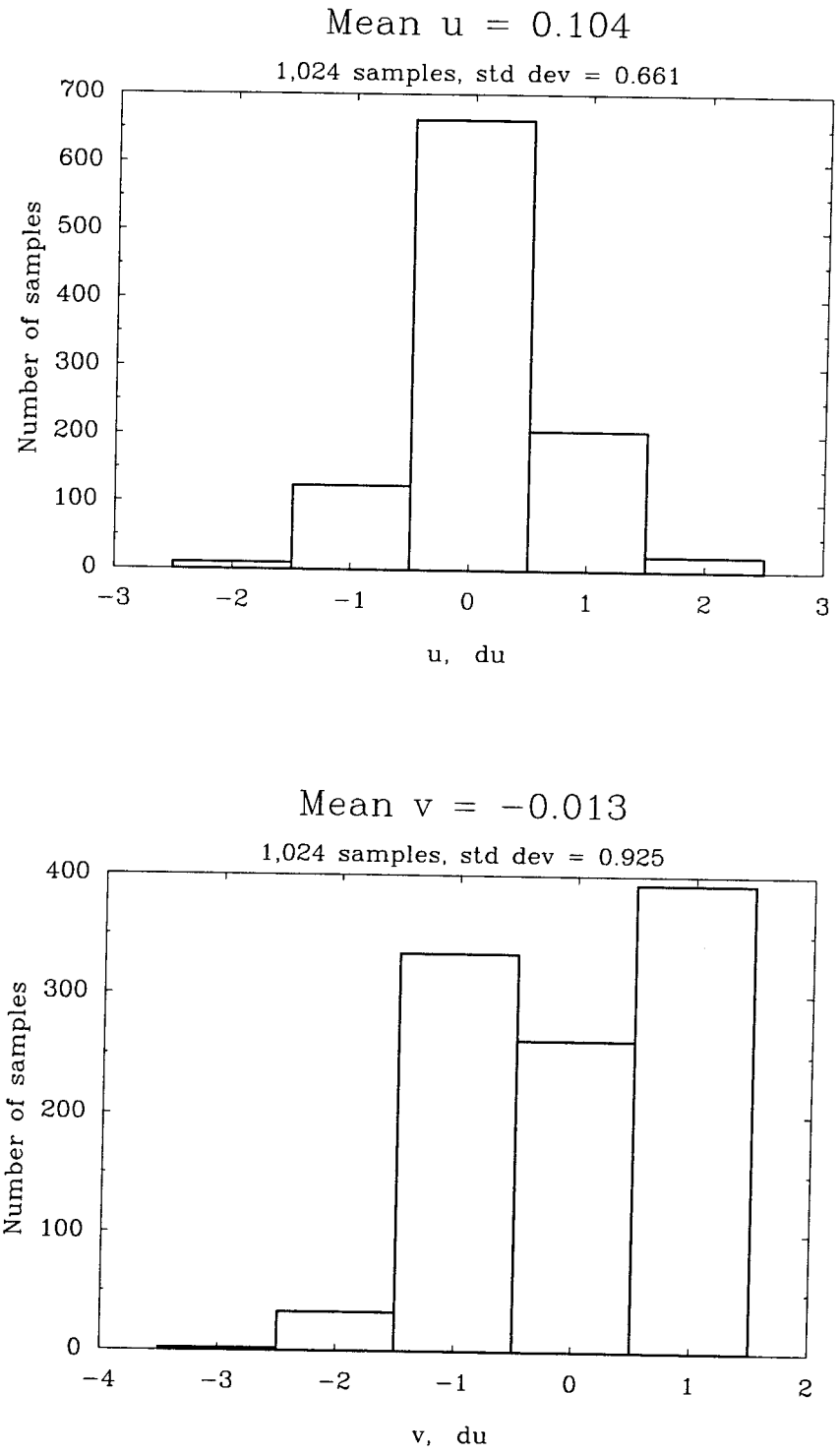

Figure 3-4: Oversampling data distribution near the center of the detector

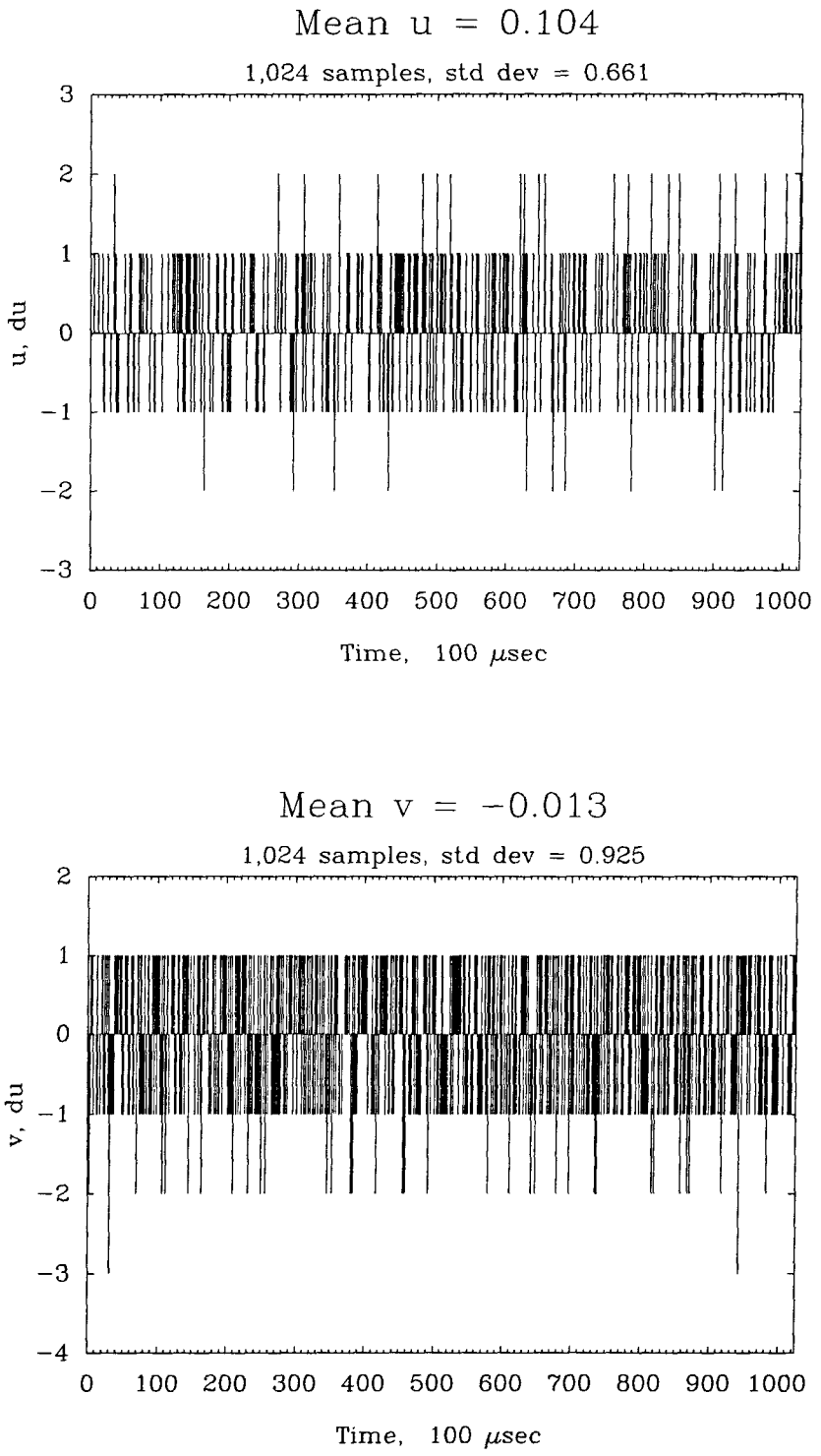

Figure 3-5: No apparent time correlation in the time scale of the observation near the center of the detector

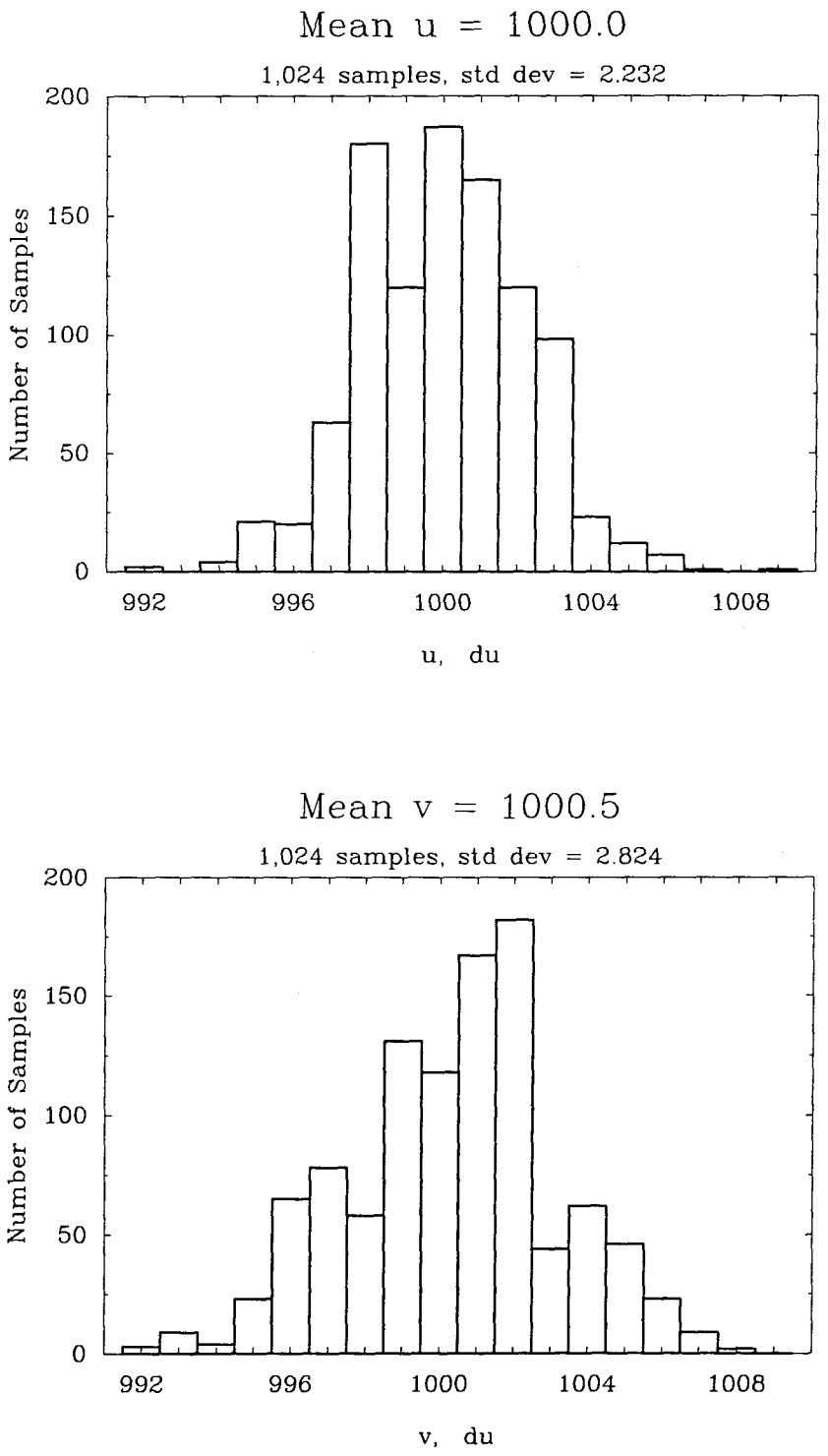

Figure 3-6: Oversampling data distribution away from the center of the detector

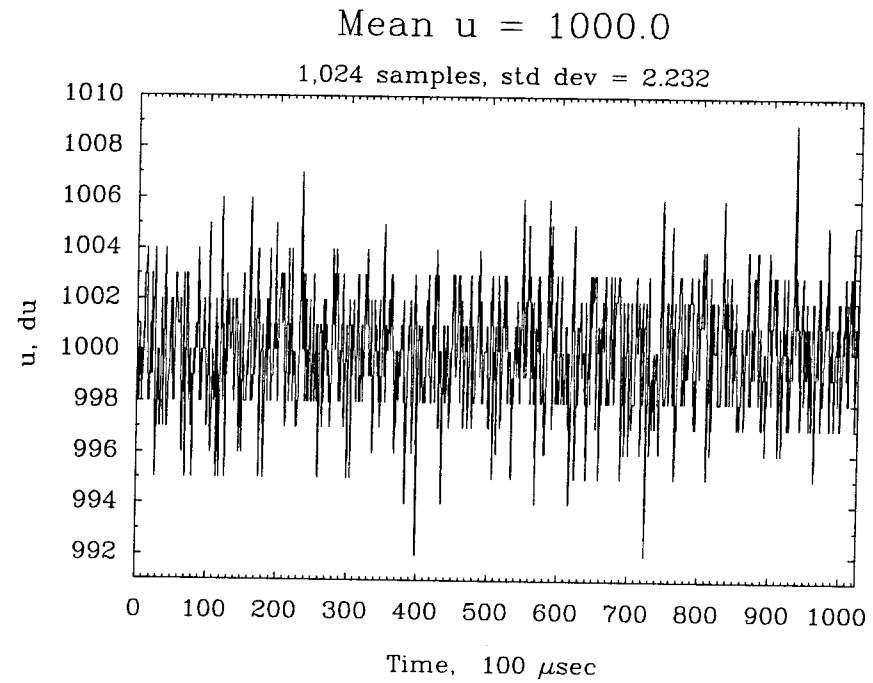

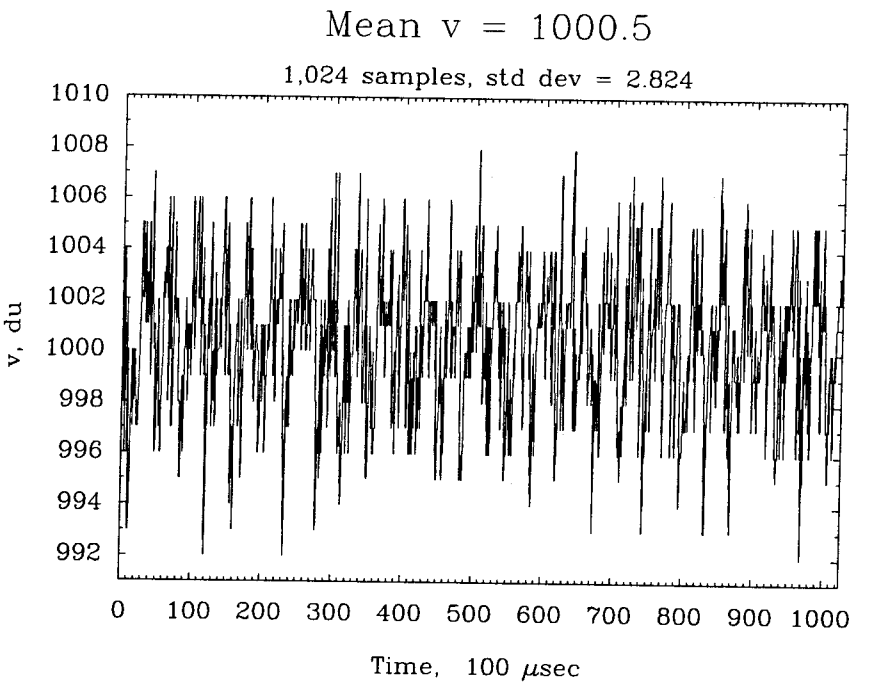

Figure 3-7: No apparent time correlation in the time scale of the observation away from the center of the detector

3.3 Specifications

3.3.1 Inter-Camera Spacing and Resolution

Nominal system resolution is a function of inter-camera spacing and can be calculated by

$$\frac{\left|\vec{R}_d\right|/2}{2^{12}=4,096}, \text{ as shown in Table 3.1.}$$

Inter-camera spacing [cm]	11.0	20.0	47.0	74.0	800	
Side of nominal viewing volume [cm]	5.5	10.0	23.5	37.0	400	
12-bit resolution [μm]	13	24	57	90	1000	(= 1 mm)

Table 3.1: Relationship of inter-camera spacing and resolution

3.3.2 Oversampling vs. Resolution and Repeatability

The detector is divided into 4,096×4,096 du (See Section 2.2), which are analogous to pixels in a CCD array. By oversampling for a stationary spot, higher resolutions can be achieved than those shown in Table 3.1. Roughly speaking, as the number of samples for each light spot is increased by a factor of ten, the resolution of the averaged coordinates becomes two times better than before, as shown in Table 3.2. In terms of bits, this means averaging yields one more "bit" of resolution for each order of magnitude increase in the number of samples.

Repeatability of the averaged data also improves commensurately, i.e., the effective noise is reduced. The repeatability is in most cases approximately the same order of magnitude as σ, the standard deviation of the averaged coordinates. If the data were independent for each sampling, the standard deviation of collecting one sample for each spot would be $\sqrt{N}$ times

Samples/stationary spot	1	16	128	1,024
Resolution [bits]	12	13	14	15
Resolution [du]	1	1/2	1/4	1/8
Resolution [°]	0.0073	0.0037	0.0018	0.0009
Repeatability [du]	4	1	1/4	1/8
Sampling speed [spots/sec]	5,000.0	312.5	39.1	4.9
System speed [spots/sec]	147.8	30.0	19.7	3.9

Table 3.2: Resolution, repeatability and speed

Samples/stationary spot		1	16	128	1,024
Camera #1	σ_u [du]	0.394	0.094	0.067	0.029
	σ_v [du]	0.293	0.115	0.044	0.014
Camera #2	σ_u [du]	0.494	0.140	0.047	0.017
	σ_v [du]	0.709	0.166	0.047	0.019

Table 3.3: Standard deviations of (u_1, v_1) *and* (u_2, v_2) *of 100 averaged stationary spots.* $(u_1, v_1) \simeq (-129, -82)$ *and* $(u_2, v_2) \simeq (298, -90)$. *Standard deviations on other parts of the detector may vary.*

that of data averaged over N samples. Table 3.3 lists the experimental data for standard deviations of 100 averaged stationary spots. Although they get smaller as the number of samples is increased for each spot, they do not follow the $\sqrt{N}$ rule exactly. This likely results from the very high sampling frequency which may make samples slightly dependent on one another. Since the repeatability shows a trend of getting better and approximately following the $\sqrt{N}$ rule as the number of samples for each light spot increases (Table 3.2), it does not seem necessary to compromise the system speed for better σ's.

In Figure 3-8, a 1×1 du area on the image plane of one detector is shown. The inter-camera spacing is 47 cm and an infrared LED[2] is positioned at the CCFOV (47 cm away

[2]Telefunken V194P

from the X-axis) as in Figure 3-2. Keeping the LED stationary, 128 samples were averaged for each dot in the leftmost cloud (Figure 3-8, in which 100 dots are shown) to demonstrate that the repeatability is approximately 1/4 du. The LED was then translated in the X direction by 0.001 in (25.4 μm) using a micrometer stage. The middle cloud shows the data acquired at this LED position. The LED was translated again by 0.0005 in (12.7 μm). The third cloud demonstrates that a 1/4 du resolution is obtained by averaging over 128 samples, which corresponds to 12.7 μm for a light spot 47 cm away. Figure 3-9 shows data acquired from a similar experiment by averaging 1,024 samples for each dot. The resolution is less than 1/8 du which corresponds to 0.00025 in (6.4 μm) from a light spot 47 cm away, and the repeatability is about 1/8 du. Averaging more than 1,024 samples, however, does not give much better results while slowing down the system considerably. It may be a limitation due to noises from both the electronics and the detectors.

3.3.3 Oversampling vs. Speed

As with almost all sensing systems, a trade-off is necessary for each application to determine the combination of detector speeds and resolutions that best fits the requirements. With 12-bit resolution, each spot is sampled at 5 KHz, while with 15-bit, at most 4.9 Hz can be achieved (see Table 3.2). Adding time spent on moving scanners, looking up error tables, calculating averages, doing file I/O, and so on (see Section 5.1.2), the system speed overhead is significant for 12-bit sampling but insignificant for 15-bit, as shown in Table 3.2. The system speed can still be improved to approach the sampling speed, however, with better programming and hardware. Note that the system speed is bounded above by the sampling

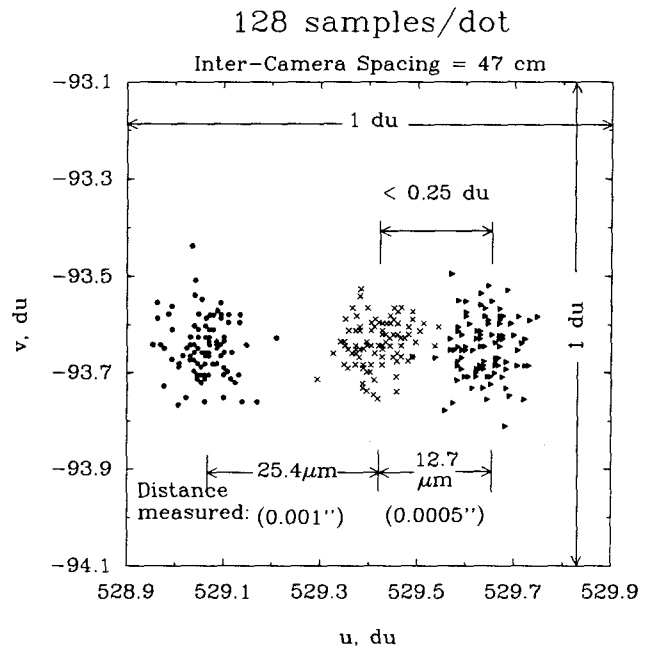

Figure 3-8: Resolution and repeatability: averaging 128 samples

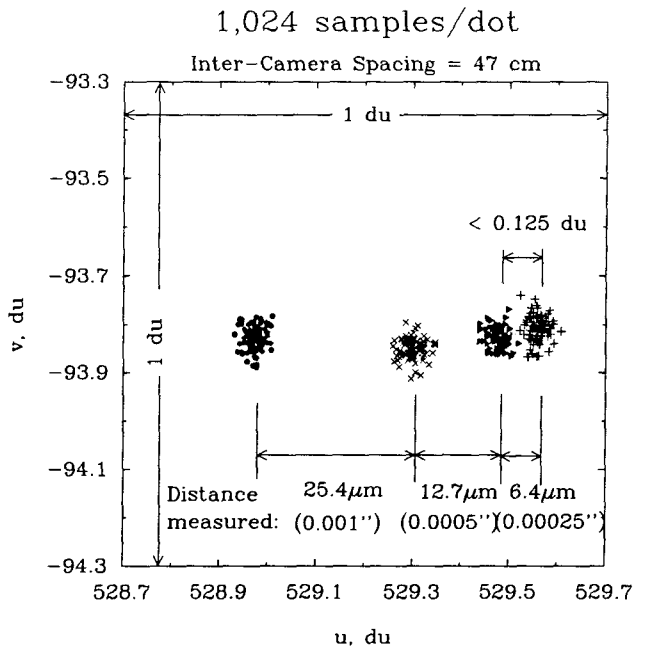

Figure 3-9: Resolution and repeatability: averaging 1,024 samples

speed, although at present the system speed is limited in practice by the 20-Hz scanners.[3]

3.3.4 Accuracy

A 5-cm ($\pm$ 0.09 μm) ceramic gage block was used to test the system accuracy by measuring one side (plane) of the block then turning the rotary table 180° to measure the other side (plane). Assuming the center of rotation is known exactly and the rotation axis is parallel to the Y-axis, one can reconstruct the world coordinates of light spots on both planes. Subtracting the coordinates on both sides gives the width of the block which can be compared to the manufacturer's data.

At inter-camera spacing of 47 cm with 1,024-oversampling, the difference between the measured width of the block and the manufacturer's data is found to be $\pm$ 45 μm, which is more than four times larger than it is desired. It is predictable, however, because at present the scanners produce jitter and wobble about four times larger than the system resolution. A more advanced scanner system is being implemented for the next stage of this project, and it will improve both the stability and speed. Additionally, locating the position of the center of rotation is not trivial (Section 5.1.1), and there are also errors coming from the installation of the rotary table, whose axis of rotation may not be exactly parallel to the Y-axis. These additional sources of error may also be confounding the results of this initial, simple, test of system accuracy.

In fact, the accuracy measured here is "relative" accuracy, because experimental data are compared to "distances" rather than exact coordinates on the object. "Absolute" accuracy will be discussed in Section 4.5. For absolute calibration, a system even more accurate than

[3]Commercial scanning systems capable of 2 – 10 KHz are presently available.

the one developed here will be required. A CMM, for example, could be used to provide an absolute calibration.

3.4 Reflection

One difficulty with optoelectronic systems is that they are sensitive to reflections. The surface of the object to be measured cannot be either too specularly reflective, such that the reflected light is not diffuse enough for both cameras to capture, or too absorptive such that not enough light gets reflected to the cameras. Under such circumstances, if the object can be coated with paint (within the resolution desired), it can still be measured. Empirically, surfaces such as those similar to white plaster are especially good for measuring, while very flat and shiny surfaces and very dark surfaces are hard to measure.

"Self-reflection" is also frequently present. The light spot on one part of the object reflects itself onto another part, producing more than one light spot in the field of view. Sometimes 3-D photogrammetric triangulation (Figure 2-6) can filter these points out because the skew vectors are too long. By rotating the object, the correct coordinates of that point may still be obtained.

To avoid reflections coming from the background, the optical table is enclosed by black infrared absorptive fabric.[4]

[4] Black duvetyne

3.5 "Warm-Up" Effect

For a stationary spot, it is found that in the beginning of the measurement, the detector position signals (u,v) vary quickly with time. Figure 3-10 shows the phenomenon, in which 500 points are shown in a 0.8×0.8 du area, each the result of averaging 1,024 samples of the same stationary spot. Once in steady state (after approximately 2 minutes), as shown in Figure 3-11, the data vary well within the repeatability limit 1/8×1/8 du. Note that only 0.1×0.1 du is shown in Figure 3-11, in which 100 dots are shown, each representing an average of 1,024 samples. Figure 3-12 demonstrates that there is no apparent time correlation in the time scale of the measurement in Figure 3-11.

LPED's are sensitive to temperature, light intensity,[5] spot size, and other effects. They can contribute to this "warm-up," but it is not simple to isolate each factor and find out their behavior. In order to exclude this effect, the detectors run until steady state is reached prior to collecting data.

To help contribute to the future characterization of these detectors, and a deeper understanding of the "warm-up" effect, temperatures are monitored by a thermistor mounted near the back side of each detector; spot size can be adjusted by the optics so it is not larger than the system resolution; intensities are controlled and reported by the cameras.

[5]The influence of intensities has been studied carefully in [37]. The result is not yet incorporated into the error maps (Section 4.1), but will be discussed.

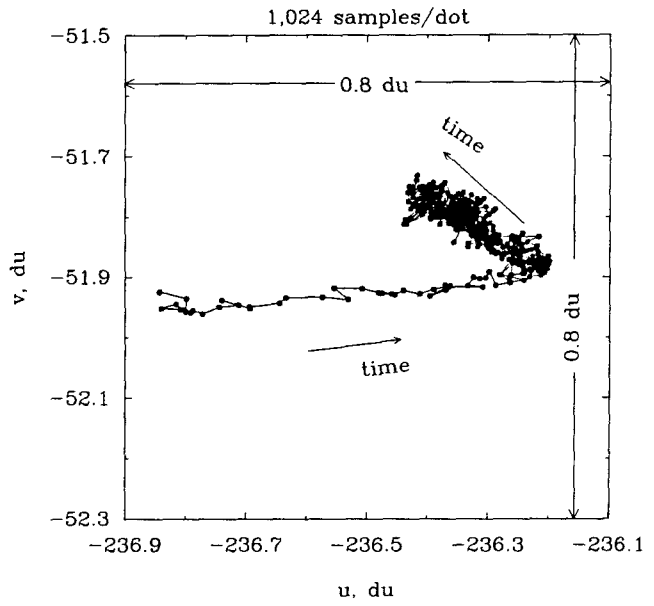

Figure 3-10: "Warm-up" effect on one detector in the beginning of data collection

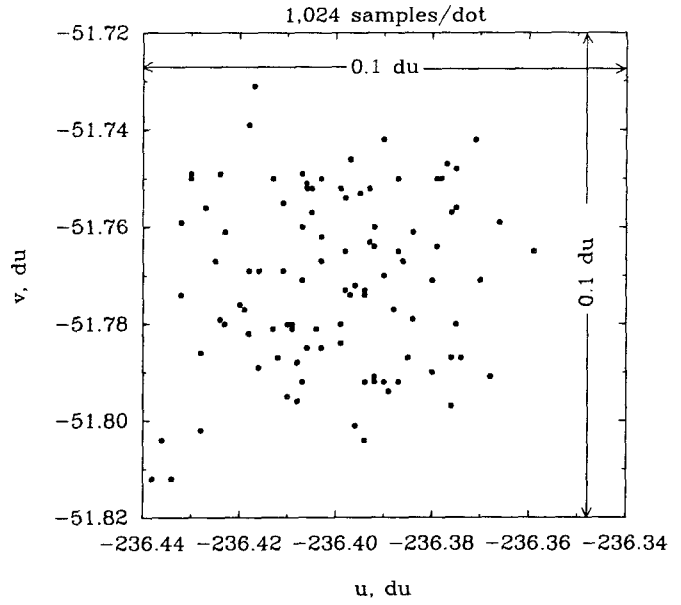

Figure 3-11: After "warm-up," data variation matches repeatability. Compare the scale with that of Figure 3-10.

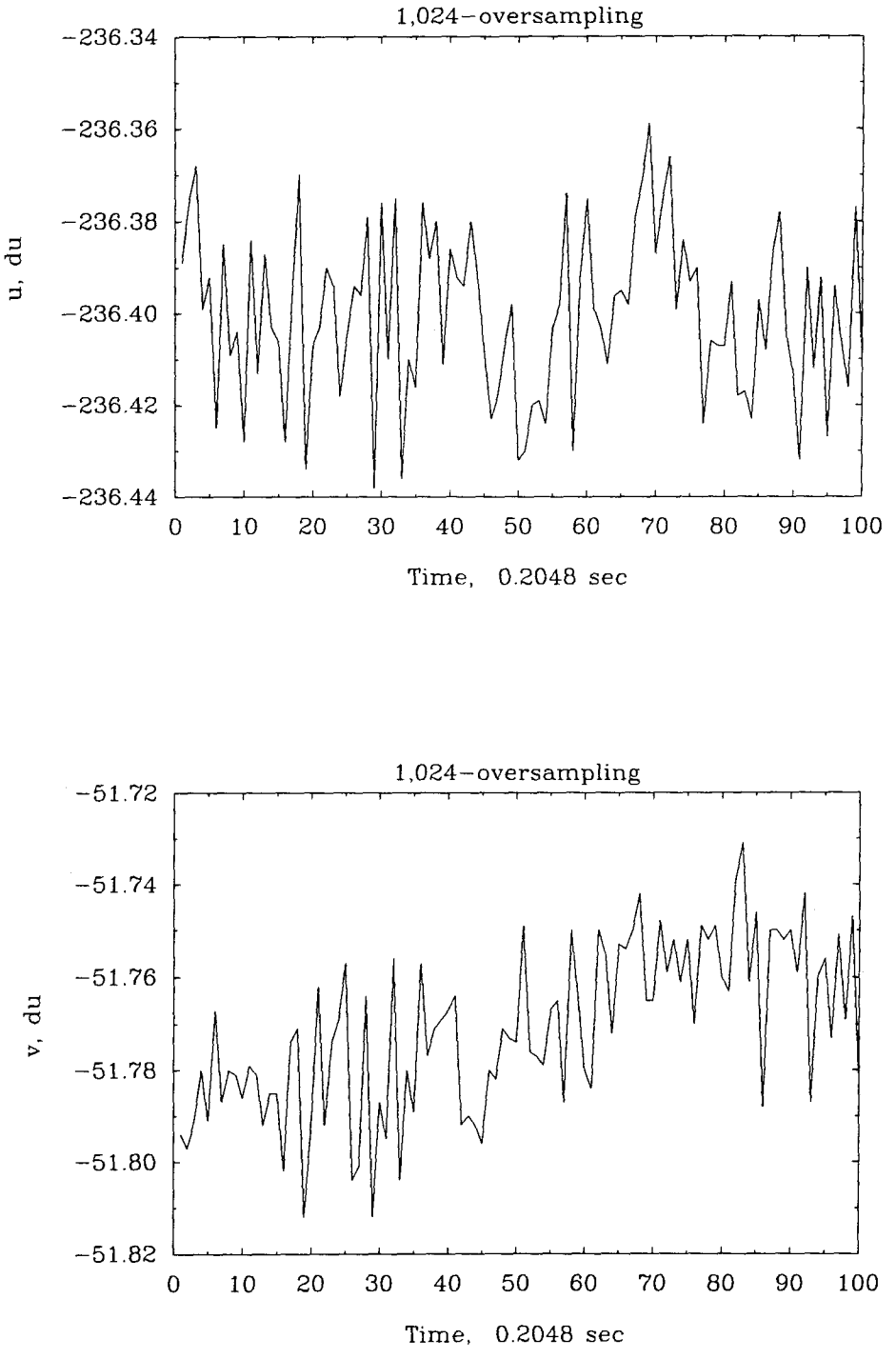

Figure 3-12: No apparent time correlation in the time scale of the observation in Figure 3-11

Chapter 4

Calibration

In order to fully exploit the characteristics discussed in Chapter 3, a detailed camera *intrinsic* calibration has been performed. An intrinsic calibration maps the errors in the image plane coordinates corresponding to various angles between incoming light rays and the principal axis. It is indispensable in high-resolution measurement systems because the errors in the cameras and the electronics can be much larger than the resolution desired. Additionally, a verification of camera positions and orientations has been done to examine the system accuracy.

4.1 Intrinsic Calibration Approach

A perfect lens and a linear LPED detector produce a trigonometric relationship between the angle of an incoming light ray and the image plane coordinates (u,v) of the light source (Figure 4-1). In practice, imperfections in either of the above elements can result in distortion. The purpose of camera *intrinsic* calibration is to find and map errors of image plane coordinates (u,v) generated by the nonlinearities in lenses, detectors, and electronics. These

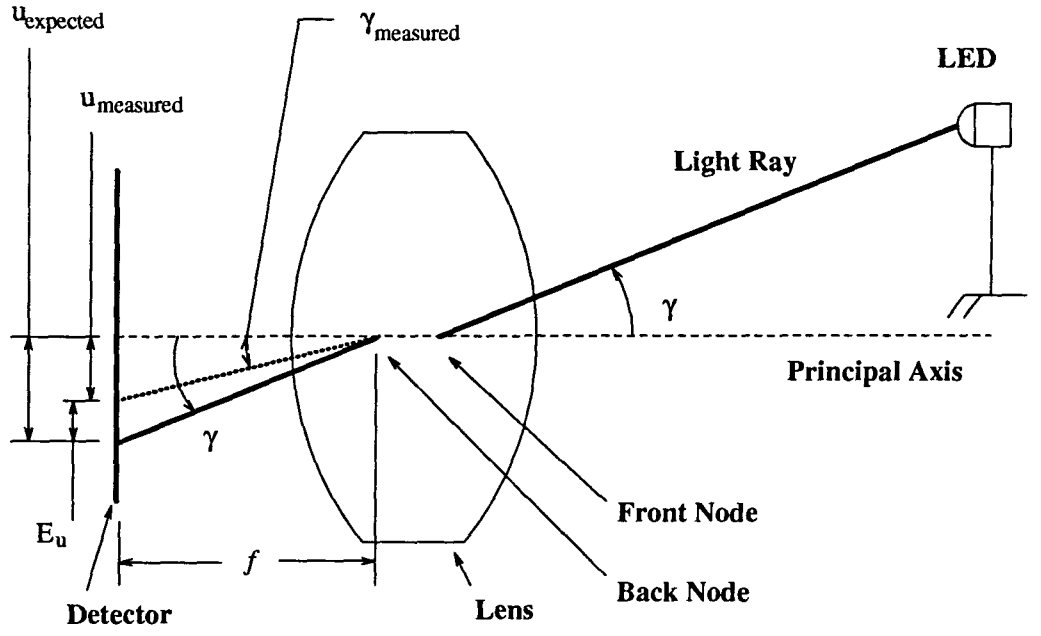

Figure 4-1: Relationship of errors and angles

errors are then subtracted from the measured values in order to produce accuracy equal to the resolution of the system.

In Figure 4-1, given a known incoming angle γ between the light ray and the principal axis, and a known principal distance f, an "expected" image plane coordinate u can be calculated. Subtracting the u actually measured from the "expected" u, the error in u-direction, E_u, can be found. The error in v-direction, E_v, can be found similarly, where the angle is called β.

$$u_{expected} = f \cdot \tan\gamma, \qquad v_{expected} = f \cdot \tan\beta. \tag{4.1}$$

$$E_u = u_{expected} - u_{measured} = f \cdot \tan\gamma - u_{measured}, \tag{4.2}$$

$$E_v = v_{expected} - v_{measured} = f \cdot \tan\beta - v_{measured}. \tag{4.3}$$

This scheme assumes that E_u at $\gamma = 0$ and E_v at $\beta = 0$ are 0. Equations 4.2 and 4.3 depend on f, which is usually not exactly known. An averaged $\bar{f}$ is used as an approximation to the true principal distance f:

$$f \simeq \bar{f} = \frac{1}{n} \sum_{n} \left| \frac{u_{measured}}{\tan \gamma} \right|.$$

Replacing f by $\bar{f}$, E_u and E_v are calculated. Error maps, E_u's and E_v's, are thus generated with respect to $u_{measured}$ and $v_{measured}$. Using bilinear interpolation, evenly-meshed u and v look-up tables are constructed. By using these tables, for any measured pair of (u,v), one first looks up in the tables to find the mesh that encloses (u,v), then bilinearly interpolates to get the corresponding errors. Adding the errors to $u_{measured}$ and $v_{measured}$, more accurate (u,v), $u_{expected}$ and $v_{expected}$, are found. This intrinsic calibration procedure was first described in [6].

The 2-axis rotary table is used to generate many different incoming angles γ and β. Each camera acts as an angle-measuring device, and the angles are recorded on the image plane as coordinates (u,v). In Figure 4-2, the camera is mounted on the rotary table, and the equipment is assembled with very high accuracy such that three assumptions can be made as follows.

1. The principal axis of the camera intersects, and is perpendicular to, the axes of both the goniometer and the rotary table;

2. the three axes intersect at the front node of the lens;

3. u and v image plane axes are mounted perpendicular to the principal axis.

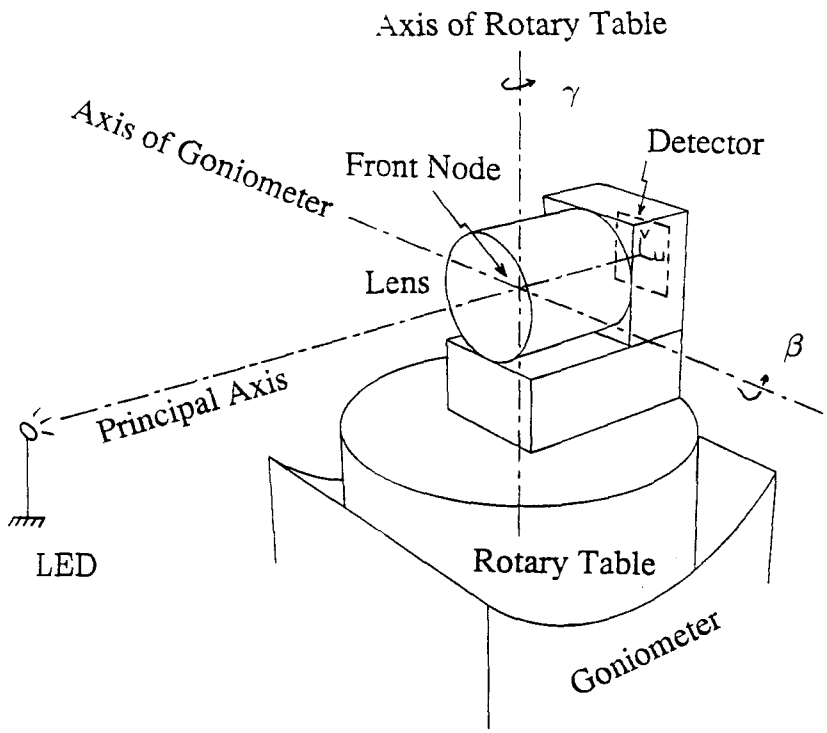

Figure 4-2: Camera intrinsic calibration setup

Perfect alignment, however, is difficult to achieve. The effects of misalignments are assumed to be absorbed into the error maps.

It is also difficult to obtain perfect alignment for laser and optical system at the calibration setting. Scanners could be helpful in doing so, but high jitter and wobble of the galvanometers that control the orientations of the mirrors can produce unpredictable errors. Therefore, to eliminate uninteresting errors from outside of the camera system, a stationary 950-nm infrared LED is used as the light source for calibration. Some slight differences in the calibration maps likely result from the use of the LED for calibration instead of the 850-nm laser diode. This discrepancy is temporarily accepted until better scanners are available.

This intrinsic calibration used 121 × 121 = 14,641 points by stepping the rotary table

or the goniometer 0.25° at a time from $-15°$ to 15°, as shown in Figure 4-3. The β' in the plot is explained in Appendix B. Each look-up table contains $101 \times 101 = 10{,}201$ points. The reason for reducing data points is explained in Section 4.4.

Intrinsic calibrations for this kind of camera have been performed on a previous 10-bit version by Antonsson [6] and a 12-bit version by Mansfield [37] using different methods.

4.2 Zeroing

As mentioned in Section 4.1, u and v image plane axes are assumed to be mounted perpendicular to the principal axis. The principal axis, however, may not pass through the origin of the uv plane. The purpose of zeroing each camera before the intrinsic calibration is thus to find their intersection (u_o,v_o), which can be determined by placing a light ray coincident with the principal axis. (u_o,v_o) is then made the new origin of the image plane for the trigonometric calculations in Equations 4.2 and 4.3. In the calibration process it corresponds to the $\gamma = 0$ and $\beta = 0$ camera position, where E_u and E_v are defined to be 0.

In Figure 4-4, the camera is 90° from the calibrating position on the rotary table so that the principal axis coincides with the axis of the goniometer. The two axes are assumed to intersect (Section 4.1).

With the LED light source fixed, rotating the goniometer produces signals of an arc on the detector. If the motion of the goniometer were circular, this arc would be a segment of a circle. Also, when the incoming ray is adjusted towards coinciding with the principal axis (this is achieved by moving the LED), this arc should approach a point, which is the desired (u_o,v_o). The accuracy of the goniometer, however, does not match that of

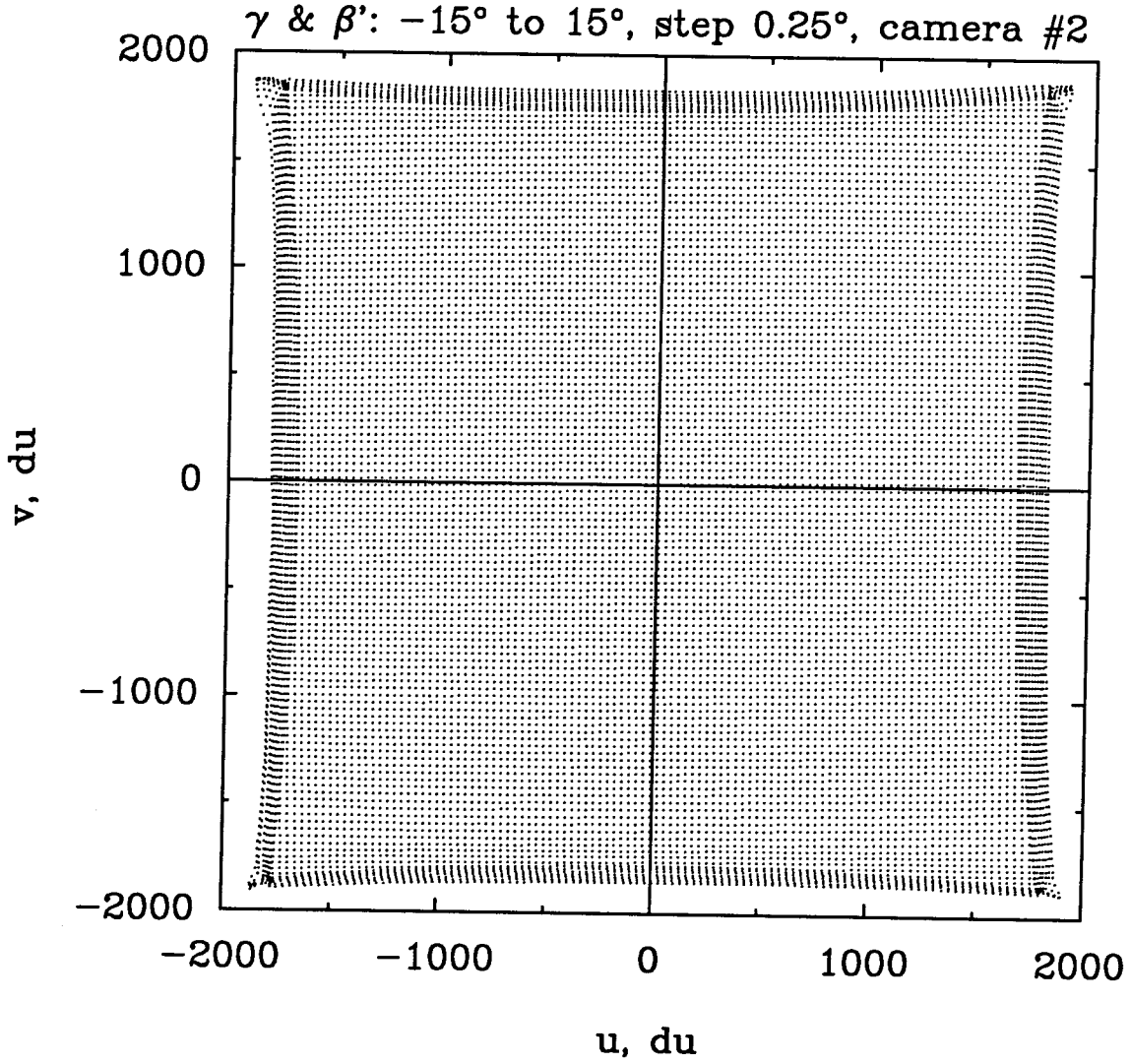

Figure 4-3: Locations calibrated on one of the detectors

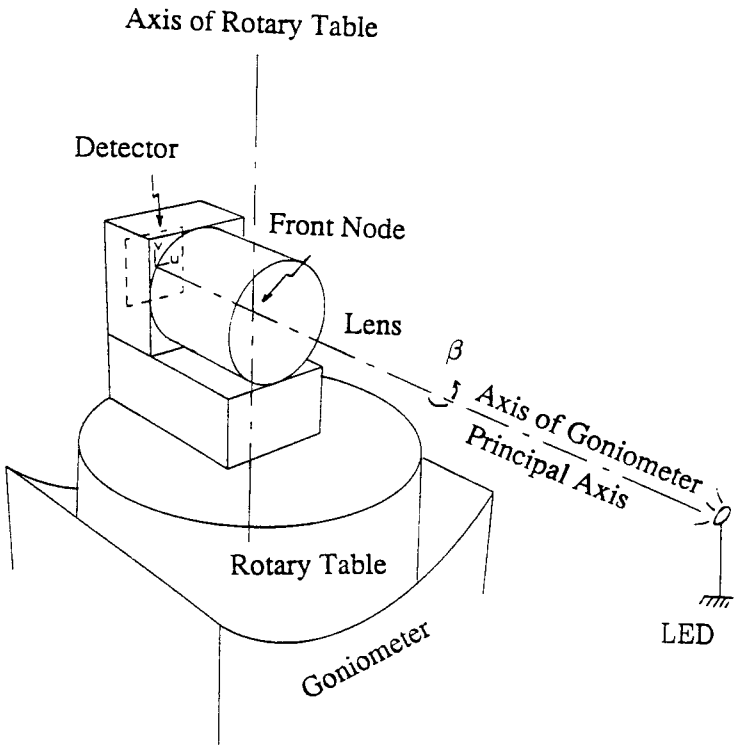

Figure 4-4: Camera zeroing setup

the optoelectronics, so convergence to a point on the detector is seldom possible. As an approximation, several arcs were fit with circles. (u_o, v_o) is taken as the mean of centers of these circles as shown in Figure 4-5 (camera #1) and 4-6 (camera #2).

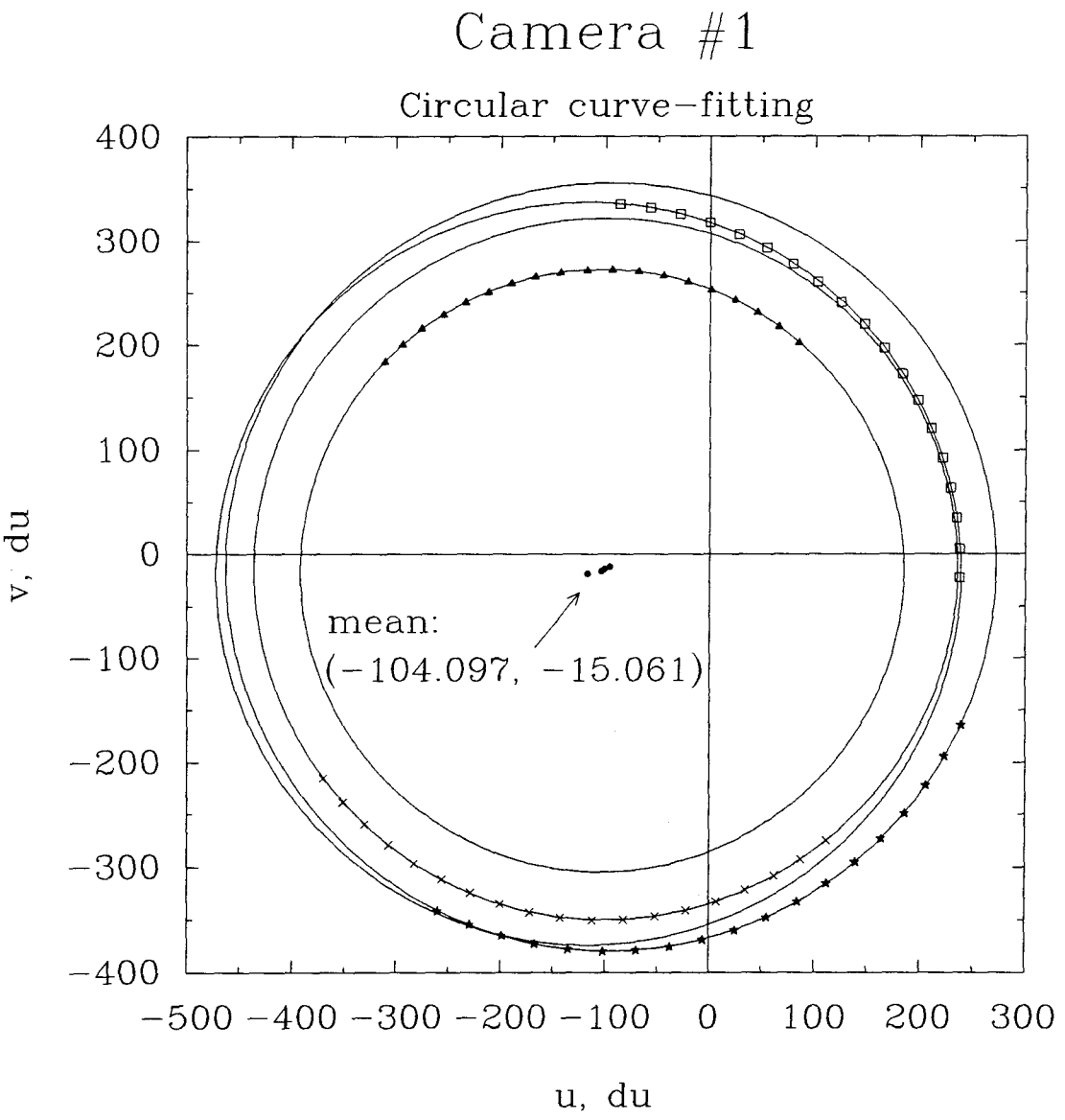

Figure 4-5: Arcs are fitted with circles to find (u_o,v_o) for camera #1.

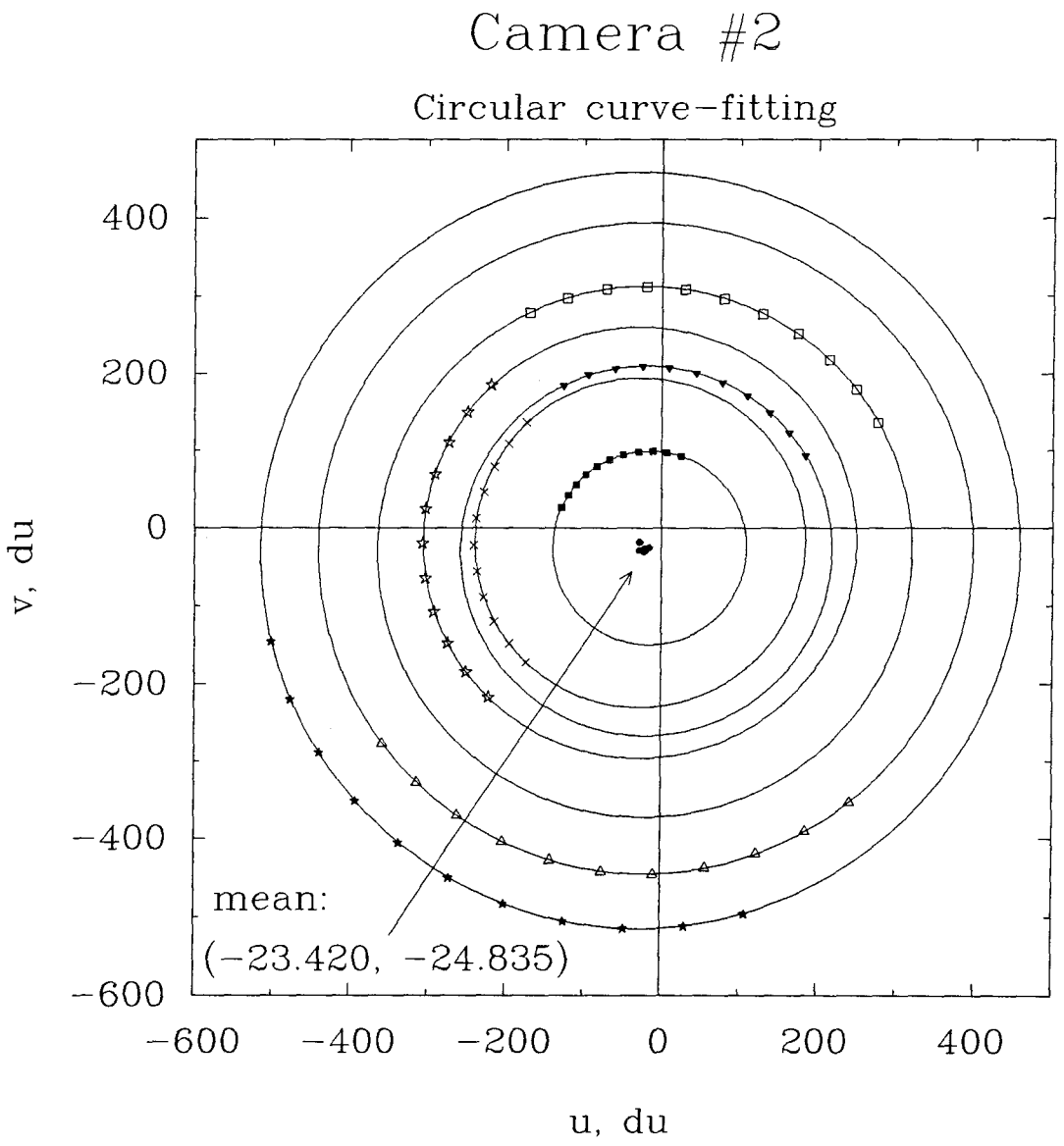

Figure 4-6: Arcs are fitted with circles to find (u_o,v_o) for camera #2.

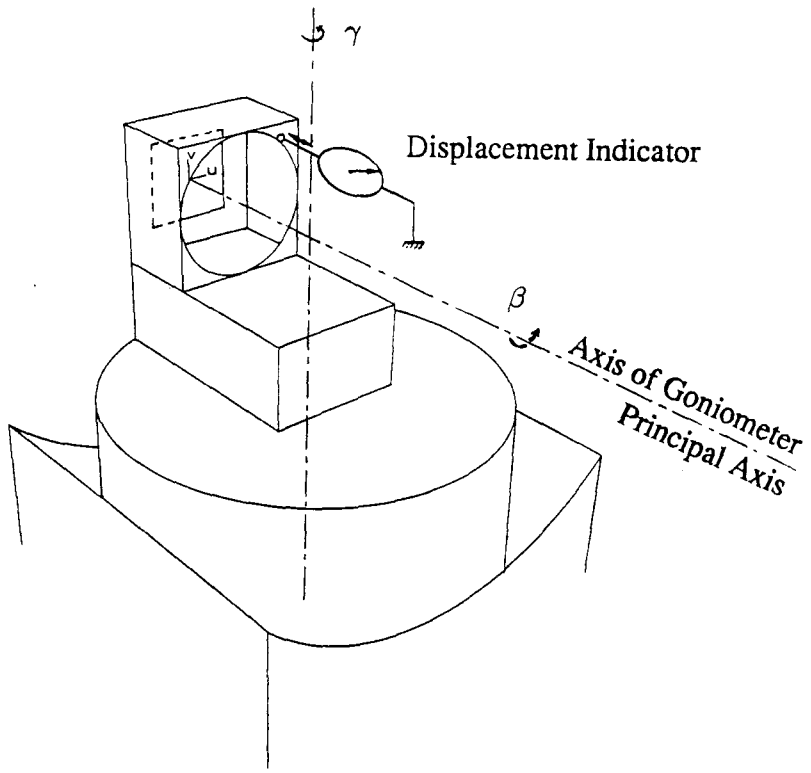

Figure 4-7: Camera zeroing position test

4.3 Some Alignment Problems

The coincidence of the principal axis with the axis of the goniometer must be checked before zeroing, i.e., the angle between them is 0. It is done by finding the exact angular position of the rotary table where the two axes coincide. The lens is taken off, as in Figure 4-7. A high-precision (1 μm) displacement indicator is attached to the circular lens mount. The plane of the lens mount is supposed to be perpendicular to the principal axis. If the two axes coincide, then when the goniometer rotates, the reading on the indicator should not change. If it changes beyond tolerance, then the angle of the rotary table should be adjusted carefully to approach the desired position.

Once the zeroing position is defined, the calibration position is set by rotating the rotary

table by $-90°$ (Figure 4-2). The LED's position is adjusted until the detector reading reaches (u_o,v_o), i.e., the light ray coincides with the principal axis. Thus the original position of calibration, $\gamma = 0$ and $\beta = 0$, is defined.[1]

Another thing to verify is whether the v-axis is mounted parallel to the world Y-axis. It can be checked by rotating the rotary table from -15° to 15° and recording detector readings. Figure 4-8 shows the horizontal trajectory by rotating the rotary table while $\beta = 0$, and the vertical one by rotating the goniometer while $\gamma = 0$. The difference is insignificant, but whether it comes from the detector mountings or the inaccuracy in the rotary table system is hard to determine. This leaves an interesting alignment problem to work on once more precise positioning hardware is available.

4.4 Error Maps

Figure 4-10 shows the E_u map of camera #2. In the upper figure, errors are heights above the detector plane uv and thus form an error surface. For a clear demonstration, only a quarter of the data are displayed. Note that the scales of all u, v, E_{u2} axes are different. The errors are in fact exaggerated. The lower figure is a contour plot of the same data. The largest absolute error shown is 257.361 du, which is 6.76% of the length of u-axis shown, 3805.660 du. Figure 4-11 shows E_v's of camera #2. The largest absolute error is 192.202 du, which is 5.06% of the length of v-axis, 3795.980 du. Figure 4-12 shows combined errors, $E = \sqrt{E_u^2 + E_v^2}$, of camera #2. Error maps of camera #1 are in Figures C-1 – C-3 of Appendix C.

[1]The repeatability of the goniometer is so unsatisfactory that when the position comes back to $\gamma = 0$ and $\beta = 0$ during the calibration, the detector does not exactly give (u_o,v_o) again. This discrepancy may be overcome by adopting more precise translation stages to move the LED instead for the calibration.

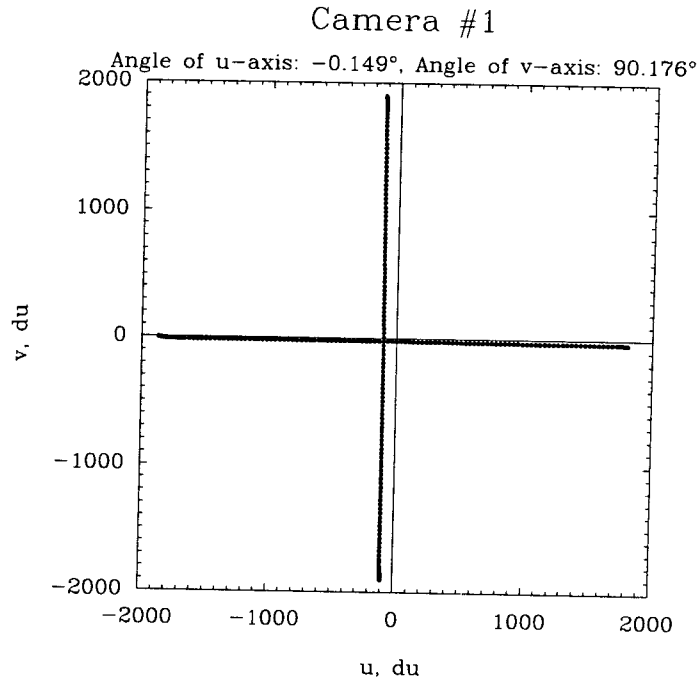

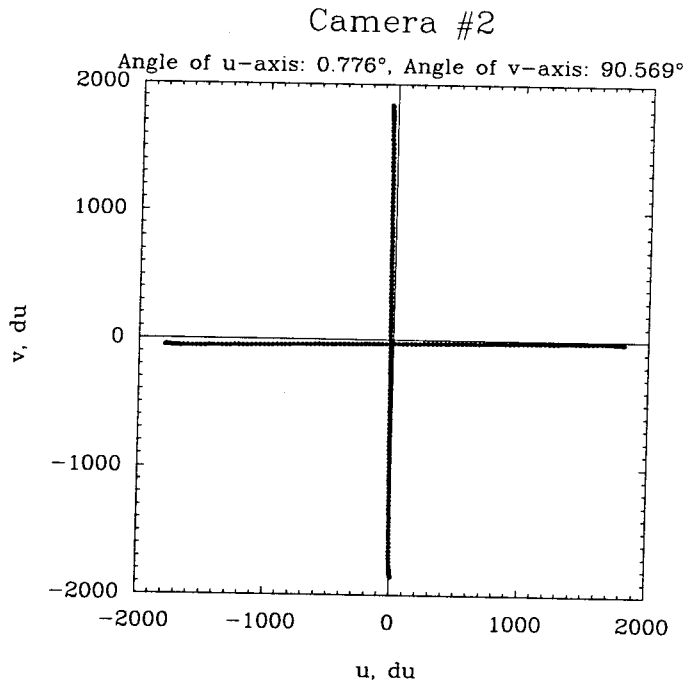

Figure 4-8: Checking detector mounting for both cameras

As we can see from the above error maps, some very large errors happen near the sides of the detectors. These errors are associated with high nonlinearities towards the sides of the lenses and LPED detectors, and they are too large to be compensated by error mapping. Therefore, trimming is done to simply neglect data coming from these areas.

Figure 4-13 shows trimmed E_u map for camera #2. The largest absolute error becomes 40.665 du, which is 1.21% of the length of the trimmed u-axis, 3343.263 du. Note that the scales shown here are different from those un-trimmed; errors are even more exaggerated. Figure 4-14 shows that the largest absolute E_v of camera #2 becomes 48.384 du, which is 1.45% of the length of the trimmed v-axis, 3336.786 du. Figure 4-15 shows combined errors. Figures C-4 – C-6 in Appendix C are for camera #1.

The trimmed error maps are used to generate look-up tables. To ensure linearity, u and v with absolute values greater than 1,600 du are cut off. Figure 4-16 shows the calibrated E_u map of camera #2 when calibration compensation is applied. The largest absolute error is reduced to 1.433 du, which is 0.05% of the length of u-axis shown, 3103.943 du. Figure 4-17 shows that the largest absolute E_v of camera #2 becomes 1.078 du, which is 0.03% of the length of v-axis shown, 3099.346 du. The above figures are drawn using the same scales as those in the trimmed error maps, Figures 4-13 and 4-14, so a comparison can be made. Figures C-7 and C-8 in Appendix C are for camera #1.

Table 4.1 lists the errors in detail.

The valid detector area after calibration is u: $-1{,}600$ to 1,600 du and v: $-1{,}600$ to 1,600 du, i.e., 3,201 du $\times$ 3,201 du, as shown in Figure 4-9. This reduces the field of view of each camera from 30° to about 25°.

	Un-trimmed	*Trimmed*	*Calibrated*
u_1	$-2010.442 \sim 1887.870$	$-1671.268 \sim 1722.522$	$-1567.379 \sim 1545.771$
v_1	$-1962.442 \sim 1953.202$	$-1706.869 \sim 1671.679$	$-1572.230 \sim 1529.715$
E_{u1}	$-135.584 \sim 284.666$ (7.27%)	$-11.071 \sim 12.442$ (0.37%)	$-0.886 \sim 1.270$ (0.04%)
E_{v1}	$-136.475 \sim 163.884$ (4.20%)	$-19.625 \sim 28.712$ (0.85%)	$-0.987 \sim 1.152$ (0.04%)
E_1	$0.143 \sim 284.864$	$0.037 \sim 30.758$	
u_2	$-1901.226 \sim 1904.434$	$-1653.288 \sim 1689.975$	$-1520.993 \sim 1582.950$
v_2	$-1907.701 \sim 1888.279$	$-1692.564 \sim 1644.222$	$-1560.637 \sim 1538.709$
E_{u2}	$-187.736 \sim 257.361$ (6.76%)	$-16.411 \sim 40.665$ (1.21%)	$-1.032 \sim 1.433$ (0.05%)
E_{v2}	$-164.143 \sim 192.202$ (5.06%)	$-31.355 \sim 48.384$ (1.45%)	$-0.785 \sim 1.078$ (0.03%)
E_2	$0.103 \sim 258.536$	$0.129 \sim 59.110$	

Table 4.1: Comparison of errors before and after calibration for camera #1 and #2. Units are all in du.

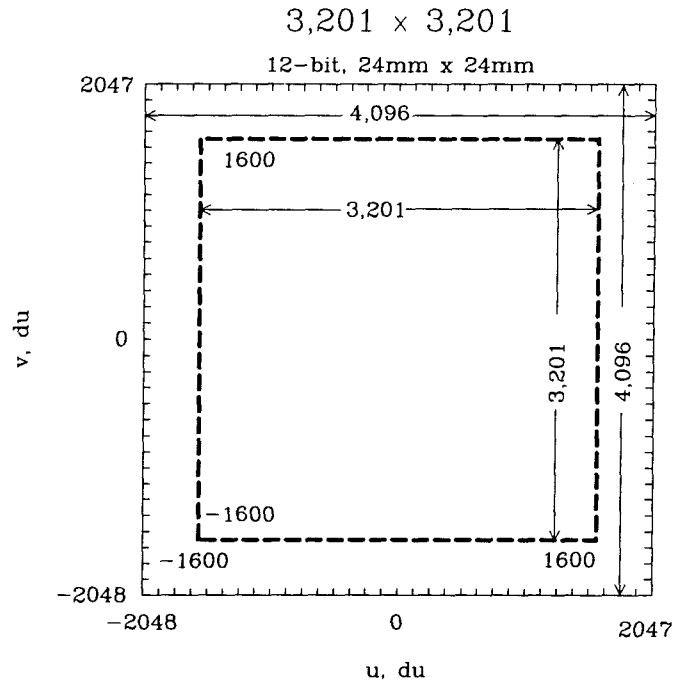

Figure 4-9: Valid detector area after calibration

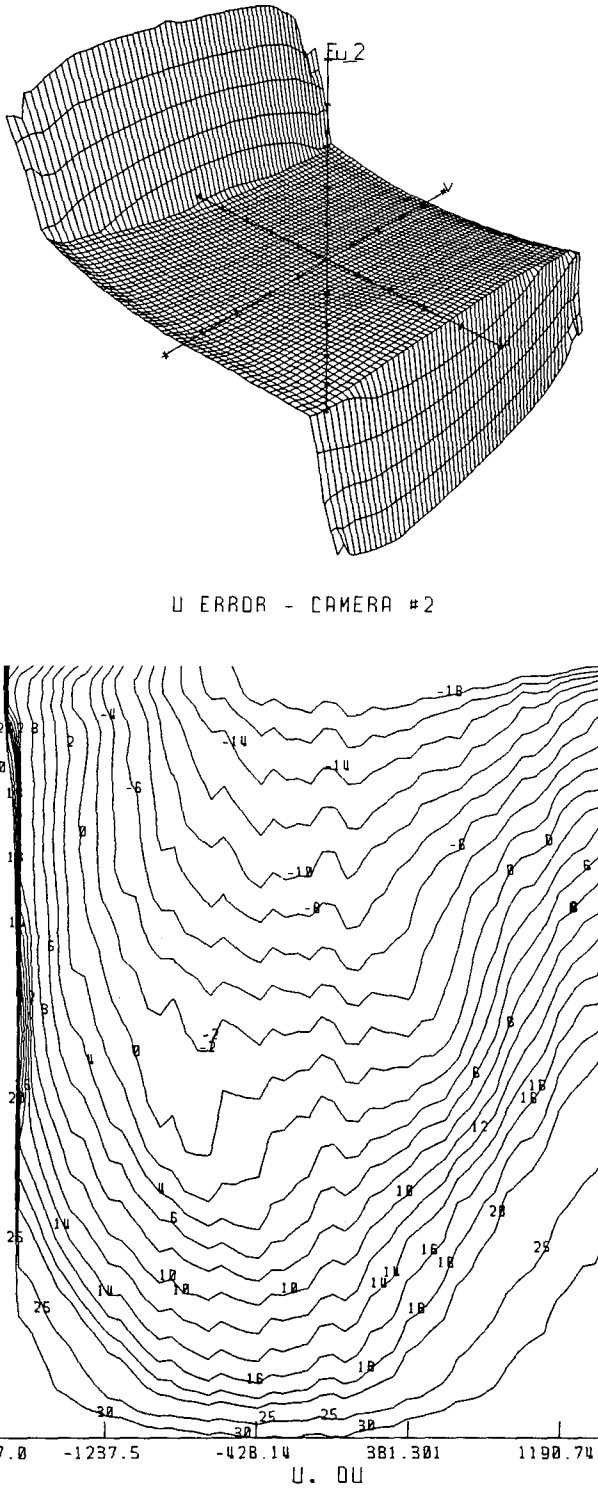

Figure 4-10: u *error map of camera #2. The upper one shows the error surface. The lower one is the contour map.* u: $-1901.226 \sim 1904.434$ *du,* v: $-1907.701 \sim 1888.279$ *du,* E_{u2}: $-187.736 \sim 257.361$ *du (6.76%).*

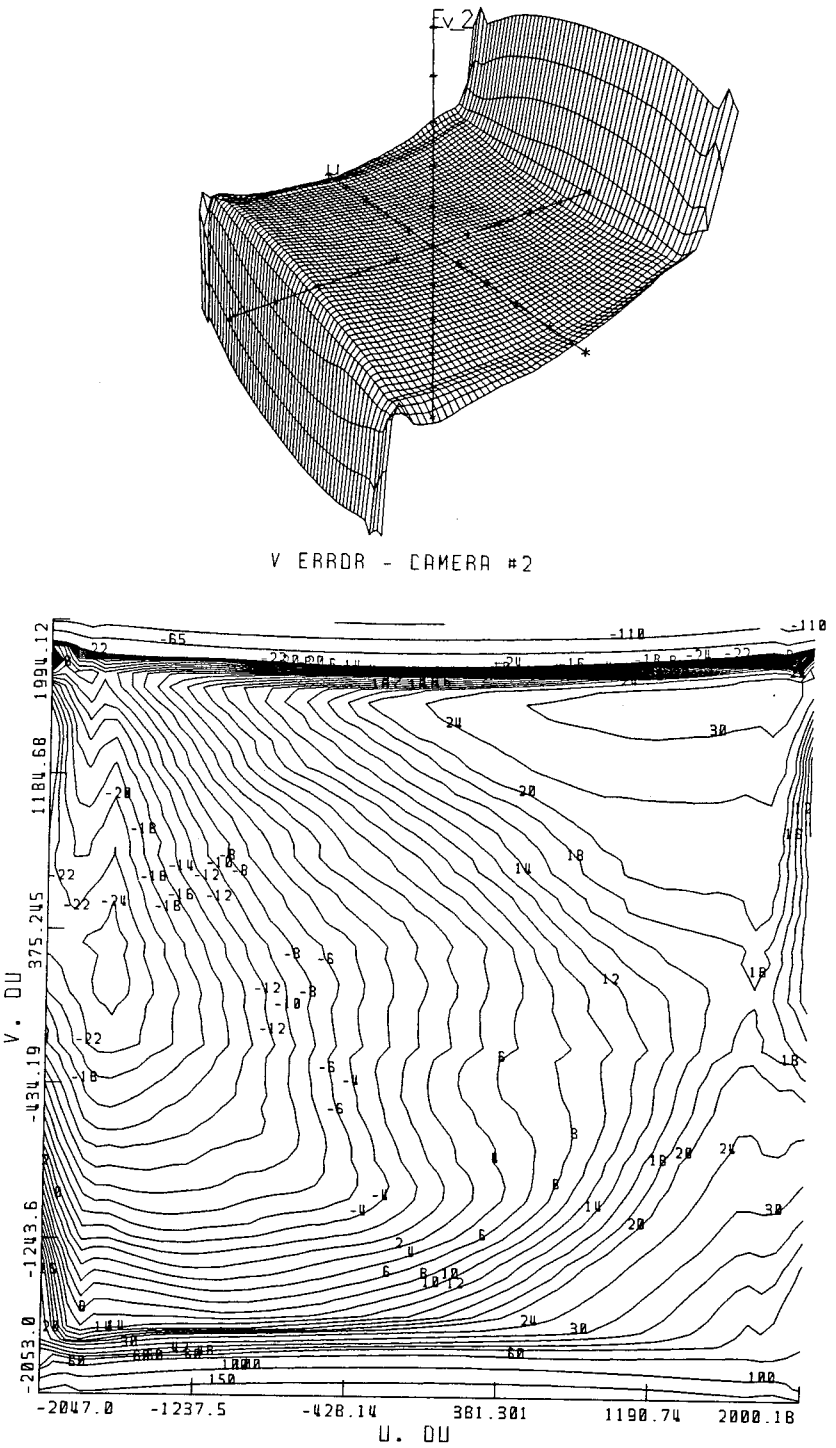

Figure 4-11: v *error map of camera #2. The upper one shows the error surface. The lower one is the contour map.* u*: −1901.226 ∼ 1904.434 du,* v*: −1907.701 ∼ 1888.279 du,* E_{v2}*: −164.143 ∼ 192.202 du (5.06%).*

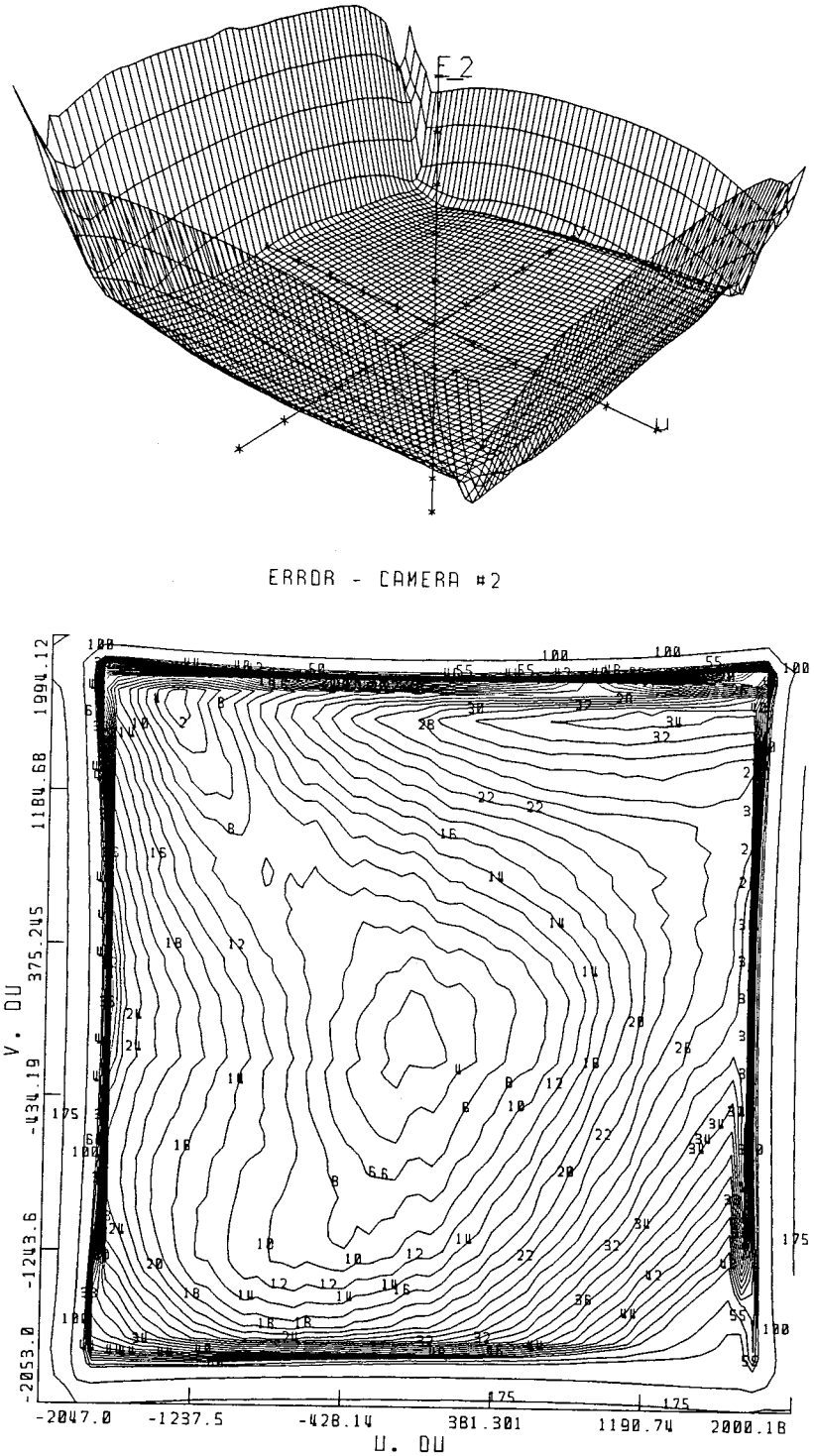

Figure 4-12: Combined error map of camera #2. The upper one shows the error surface. $E = \sqrt{E_u^2 + E_v^2}$. *The lower one is the contour map.* u: $-1901.226 \sim 1904.434$ *du,* v: $-1907.701 \sim 1888.279$ *du,* E_2: $0.103 \sim 258.536$ *du.*

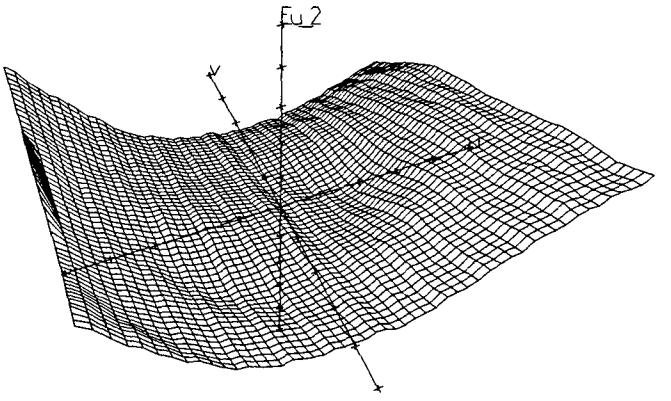

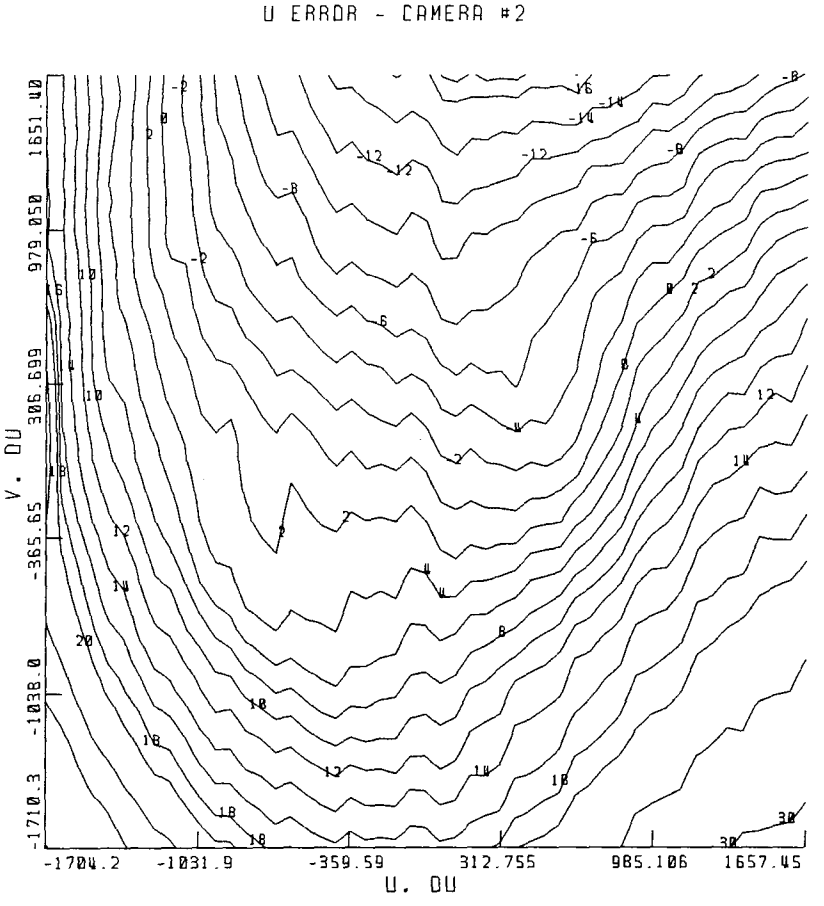

Figure 4-13: Trimmed u *error map of camera #2. The upper one shows the error surface. The lower one is the contour map.* u: $-1653.288 \sim 1689.975$ *du,* v: $-1692.564 \sim 1644.222$ *du,* E_{u2}: $-16.411 \sim 40.665$ *du (1.21%).*

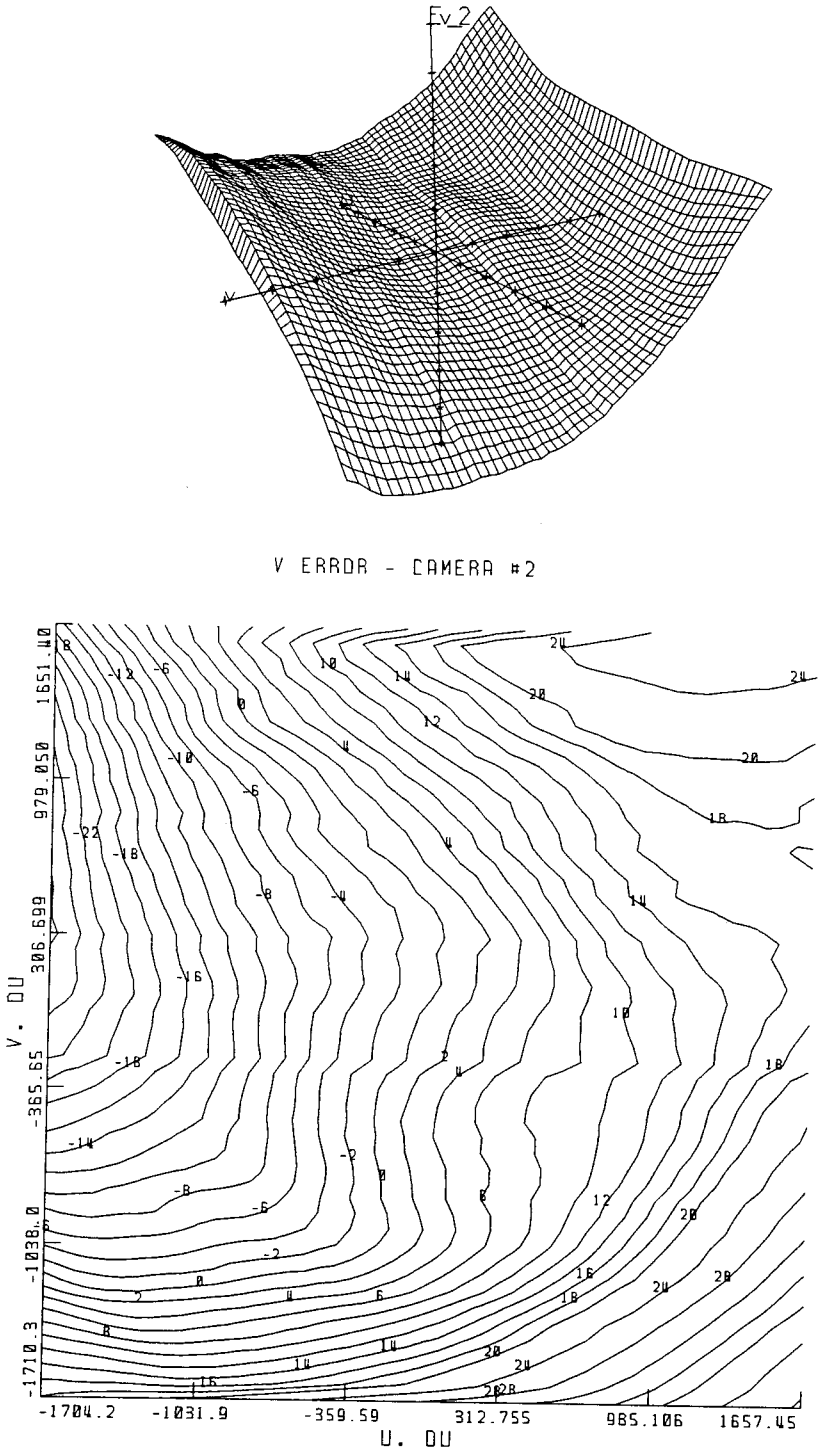

Figure 4-14: Trimmed v *error map of camera #2. The upper one shows the error surface. The lower one is the contour map.* u: $-1653.288 \sim 1689.975$ *du,* v: $-1692.564 \sim 1644.222$ *du,* E_{v2}: $-31.355 \sim 48.384$ *du (1.45%).*

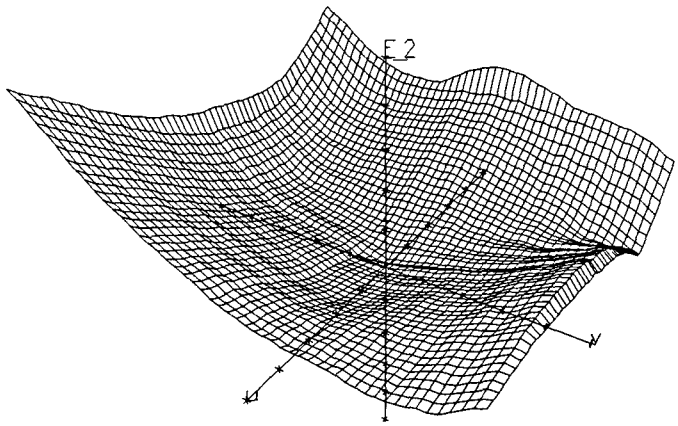

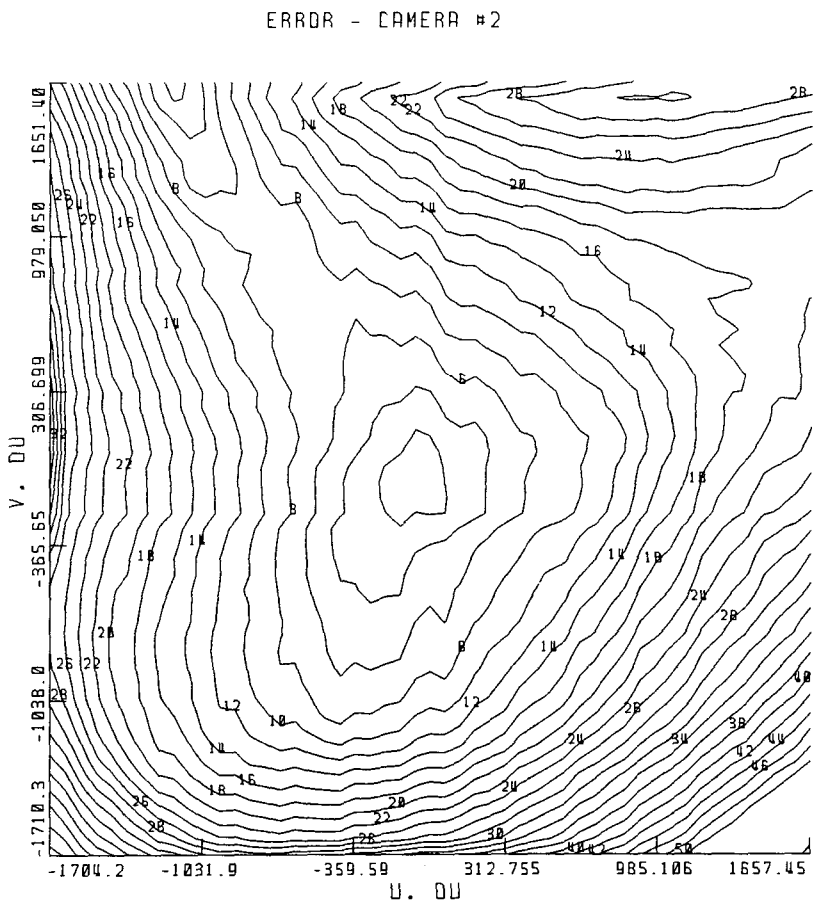

Figure 4-15: Trimmed combined error map of camera #2. The upper one shows the error surface. $E = \sqrt{E_u^2 + E_v^2}$. *The lower one is the contour map.* u: $-1653.288 \sim 1689.975$ *du,* v: $-1692.564 \sim 1644.222$ *du,* E_2: $0.129 \sim 59.110$ *du.*

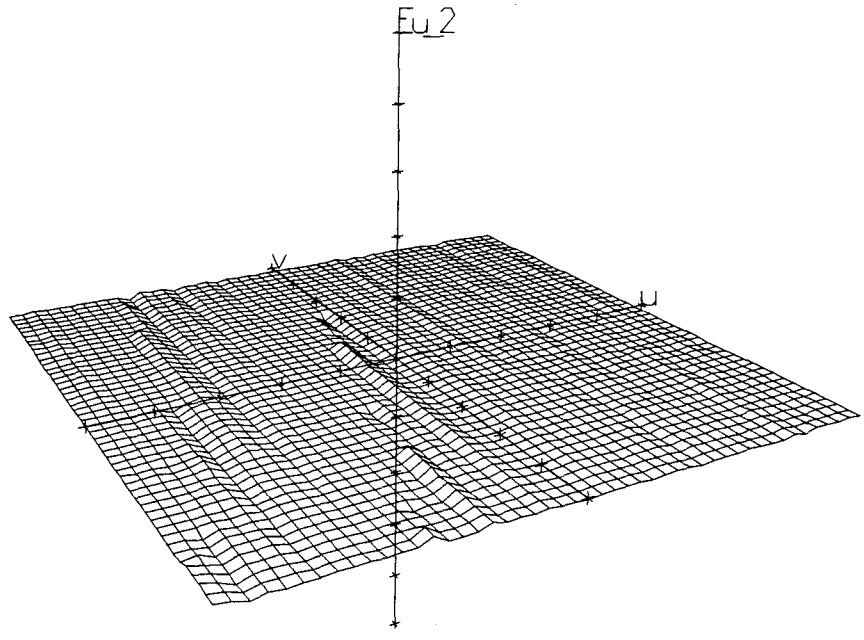

Figure 4-16: Calibrated u *error surface of camera #2.* u*: −1520.993 ∼ 1582.950 du,* v*: −1560.637 ∼ 1538.709 du,* E_{u2}*: −1.032 ∼ 1.433 du (0.05%).*

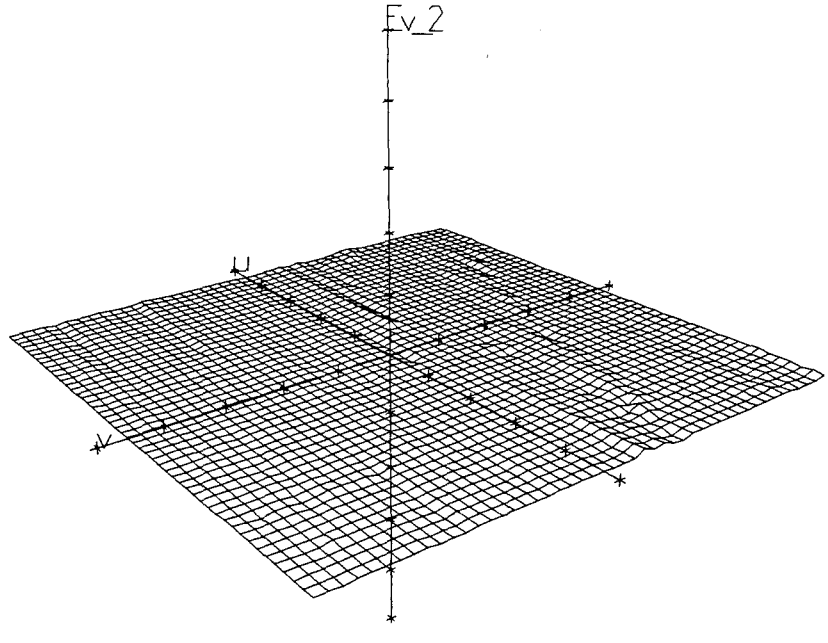

Figure 4-17: Calibrated v *error surface of camera #2.* u*: −1520.993 ∼ 1582.950 du,* v*: −1560.637 ∼ 1538.709 du,* E_{v2}*: −0.785 ∼ 1.078 du (0.03%).*

4.5 Verification of Camera Positions

After the *intrinsic* calibration, the cameras are set up in the stereo positions to perform their tasks. A verification should be done to check if they are in the correct positions.

In Figure 3-2, The angles $-\theta_1 = \theta_2 = \tan^{-1}(\frac{1}{2})$ are carefully fixed with high accuracy. The cameras sit on a precisely-manufactured horizontal aluminum beam. An LED was positioned close to the CCFOV and was carefully moved around in an attempt to locate the position where the cameras both report (u_o,v_o), i.e., when the light ray coincides with the principal axes. The photogrammetric reconstruction of the zeros will give the 3-D coordinates of CCFOV, whose X component = $|\vec{R}_d|/2$ (one half the inter-camera spacing), Y = 0, and Z = $|\vec{R}_d|$.

Because the levels of the cameras in the Y-direction are not adjustable separately, only three of the four image plane zero coordinates can be precisely maintained. The other one is off by about 10 du with $|\vec{R}_d|$ = 47 cm. That is to say the two principal axes do not intersect within tolerance using current hardware.

This misalignment results in "absolute" inaccuracy δX = 81 μm, δY = 46 μm, δZ = 473 μm at CCFOV with $|\vec{R}_d|$ = 47 cm, which is not satisfactory. With better mounting hardware, it is expected to improve. This error is currently absorbed by the skew vector $\vec{e}$ mentioned in Section 2.3. It has little effect, however, on the "relative" accuracy (Section 3.3.4), which is associated with the distance between two points instead of exact coordinates.

Chapter 5

Data Acquisition and Analysis

5.1 Data Acquisition

The system is now able to measure various shapes with good repeatability and with specifications mentioned in Chapter 3.

5.1.1 Finding the Rotation Center of the Object

Because multiple views are taken from all sides of an object by rotating the goniometer and the rotary table, the center of rotation (X_o, Y_o, Z_o) in Figure 5-1 is crucial in merging the views back together to form an overall description of the surface.

The axes of the rotary table and the goniometer intersect and are mounted perpendicular to each other. It is assumed that the axis of the rotary table is parallel to the world Y-axis, so the rotary table rotates on a plane parallel to the XZ plane and the goniometer rotates on another plane parallel to the YZ plane.

To find (X_o, Y_o, Z_o), it is convenient to follow the trajectory of a spot fixed on the rotary table. When the goniometer rotates, the center of the resulting arc gives (Y_o, Z_o). On the

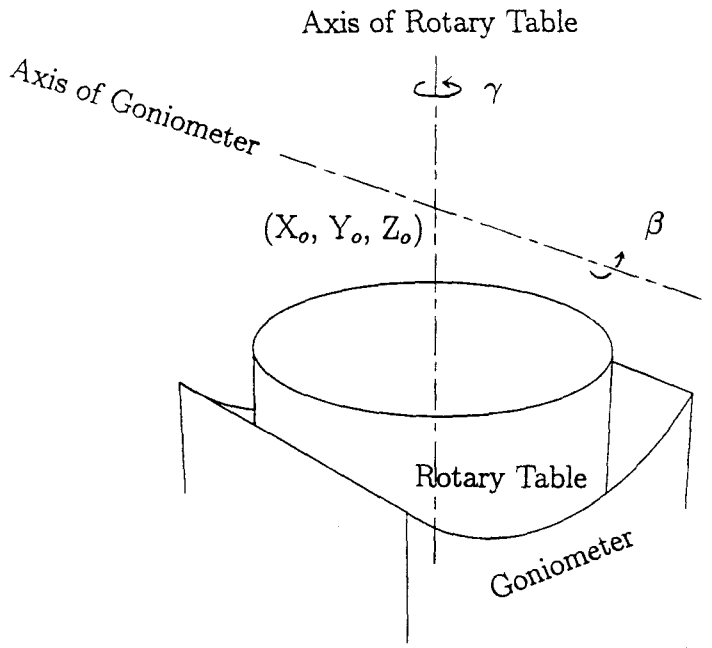

Figure 5-1: Center of rotary table and goniometer

other hand, if the rotary table rotates, the result gives (X_o, Z_o). The spot is generated by fixing a needle on the rotary table and adjusting the scanners so that the laser light always shines on the needle at the same position when the rotary table or goniometer moves.

The upper part of Figure 5-2 shows the data obtained by only rotating the rotary table when the inter-camera spacing is 47 cm. In this case, the data are on a plane parallel to the XZ plane. Therefore, their Y coordinates are the same. The data are thus fitted by a circle and the center of the circle is the rotation center of the rotary table. A similar experiment was done for the goniometer. In this case, because the goniometer travels only ±45°, only one quadrant of a circle can be obtained. The fitted circle is parallel to the YZ plane as shown in Figure 5-2. The center of the circle is the rotation center of the goniometer.

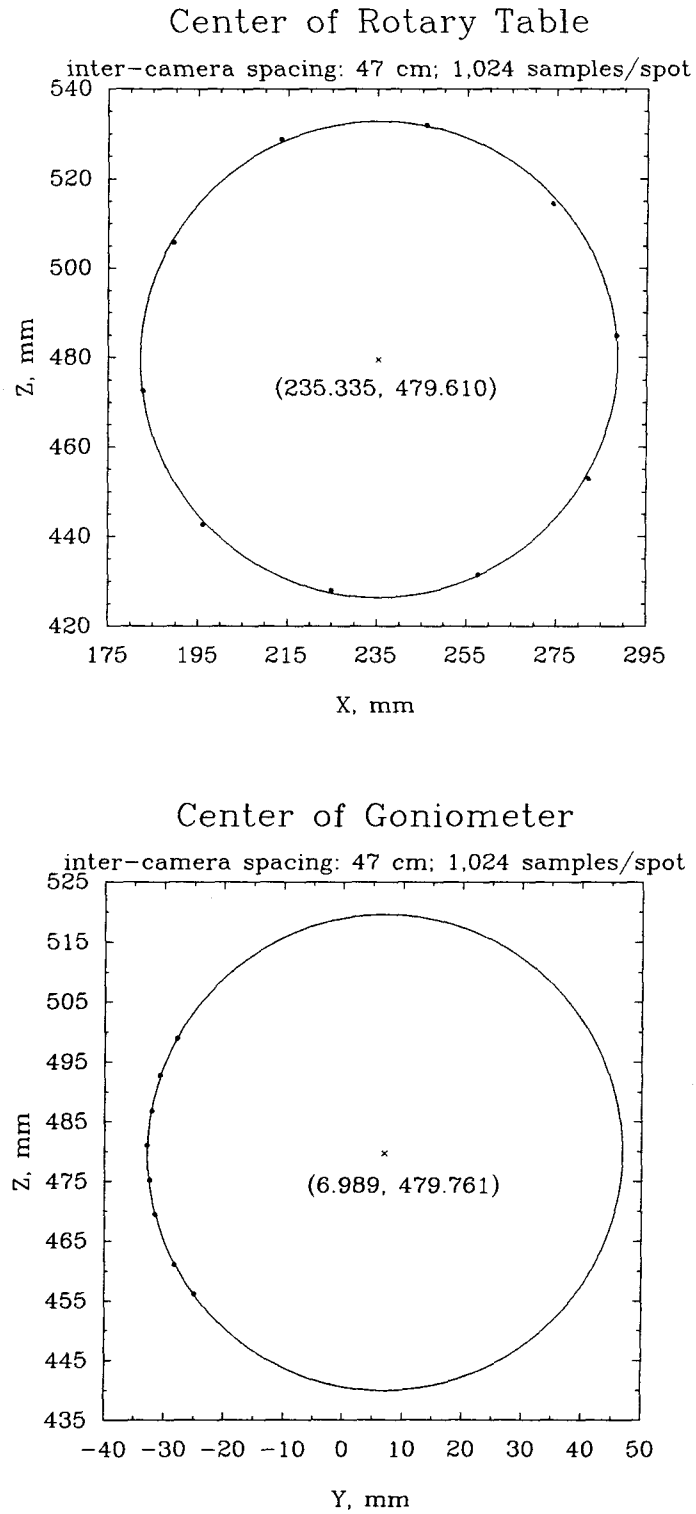

Figure 5-2: Centers of rotation of the rotary table and the goniometer

Note that the center of rotation is set close to CCFOV, because the region close to CCFOV has the best resolution (Section 3.1.4).

The Z coordinates of both measurements, however, are not exactly the same. This inaccuracy may result from one or more of the following: The mounting of the rotary table system may not be precise enough, so the axes do not intersect or are not perpendicular to each other. The plane of rotation of the rotary table may not be exactly parallel to the XZ plane, or the plane of the goniometer not parallel to the YZ plane. The laser light may not scan the needle at precisely the same position every time. These errors result in slight registration problems, but may be compensated by software (Section 5.4).

5.1.2 Real-Time Task Scheduling Data Acquisition

The camera system, the scanners, and the rotary table system are all controlled by the real-time task scheduling microcomputer. Because the camera system has its own CPU and FIFO buffer, we are able to collect and process the data in parallel in order to exploit the speed of the system.

Figure 5-3 shows a flow chart of a cycle of data acquisition which measures then calculates the 3-D coordinates of a single light spot. Collecting one sample for each stationary spot takes only 200 μsec for the cameras to finish, while the tasks taken care by the microcomputer take much more time to be done and thus slows down the measurement. With oversampling, the task that usually takes the longest time to finish is the camera data acquisition. The tasks that the microcomputer is performing may be done before the data array is filled, although decoding/averaging and looking up in the error maps take a non-negligible amount of time. This explains why the system speed of 1,024 oversampling is much closer

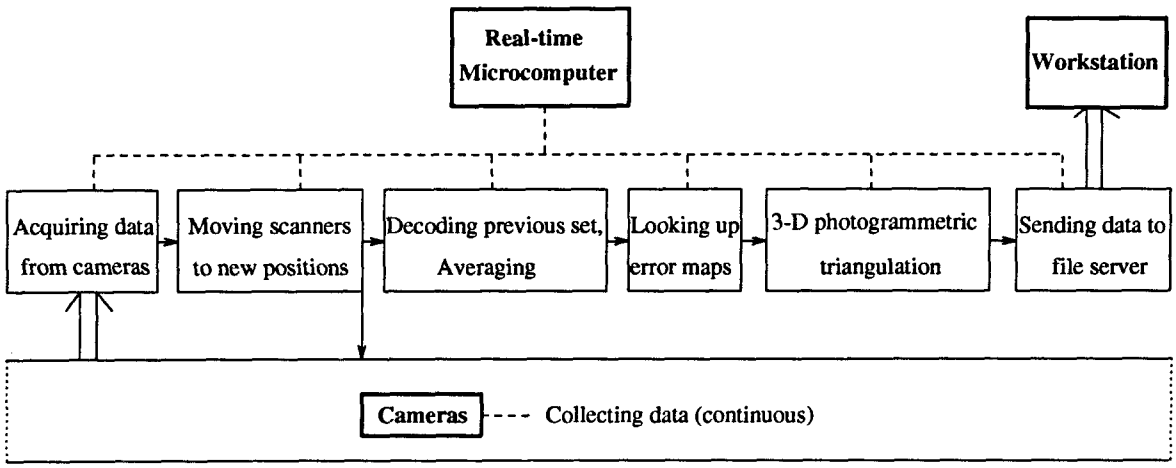

Figure 5-3: Flow chart of 3-D coordinates acquisition of a single light spot

to the sampling speed in Table 3.2, whereas without oversampling, the difference is very large.

In view of the "warm-up" effect mentioned in Section 3.5, the cameras run constantly collecting data. When the microcomputer does not need data from the cameras, the camera system puts the collected data into a "trash can," that is, the data collected are of no use except for keeping the system "warm." Unfortunately, the amount of trash data collected every time is as large as that of the real data which are to be averaged, because only one "sequence file" can be accepted by the camera system at a time, and reading in a new set of commands whenever the camera system switches between collecting useful data and trash data takes even more time. This explains why the system speed of 1,024-oversampling is still a little lower than the detector speed as shown in Table 3.2. This is limited by the commercial camera system and should be improved with smarter design.

5.1.3 Results

Different shapes, a model of a tooth, an automobile part, and a valve, have been measured with 47-cm inter-camera spacing and 1,024-oversampling.

Figure 5-4 shows an automobile part known as "the Renault part"[1] in computer vision. In Figure 5-5, ten views (15,055 points in total) taken from several sides of the automobile part are combined and displayed from different angles. Each display is a perspective view of 3-D data points on the surface of the object. There is an X-ray effect because data from all sides are displayed at the same time. Because the precision of the goniometer is far worse than that of the rotary table, only the rotary table is rotated to change views. Therefore, regions that can be covered only by rotations of the goniometer are not scanned. This explains why some regions in the figure do not have any data even though there should be. For future data collection, scanners can be mounted on a vertical translation stage in order to change the relative positions of the beam and the object to cover such areas. Some data-missing areas are due to the dark color of the Renault part, which may be improved if white coating is applied.

Figure 5-6 shows a plastic garden hose valve. In Figure 5-7, eight views (52,854 points) taken from all 360° of the valve are combined and displayed from different angles. Outliers are present due to the concave regions of the surface. The measurement of the shallow dimples, however, is visually very accurate.

To detect concave regions with high accuracy is by no means a trivial problem. To overcome this, one has to reduce the inter-camera spacing so that the cavity is not too much

[1] Courtesy of Professor Gérard Medioni of the University of Southern California

smaller than the combined FOV in order to cover details. Multiple views from all directions have to be taken in order to gather enough information to distinguish useful reflections from scattering within the cavity. Similar to human eyes, the system can accurately visualize the inside of a cavity only when it is close enough and/or that the object has made several rotations/translations for data coming from different corners to be collected.

Figure 5-8 shows a plaster model of a tooth[2]. It is a good shape to begin with, because the surface does not have too many discontinuous features, yet is complicated enough to test the sensitivity of the system. Besides, white plaster introduces a good combination of reflection and diffusion. Figure 5-10 shows data acquired from one view of the tooth. Figure 5-9 is a combination of eight views taken from all sides of the tooth, in which 46,831 points are displayed. The tooth data shall be analyzed in data merging and registration shortly.

[2]Courtesy of Professor Medioni

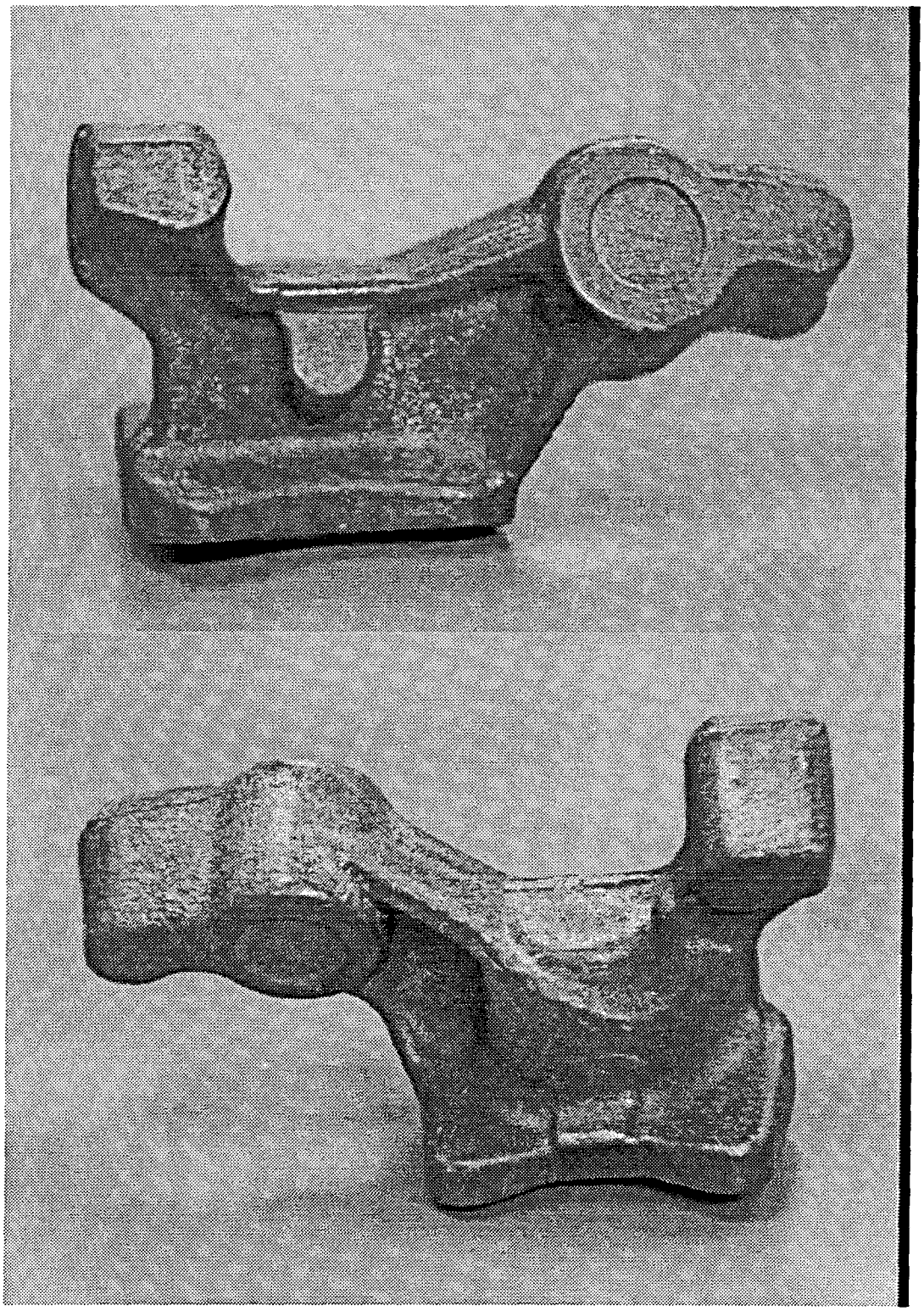

Figure 5-4: Images of the Renault part. Dimensions: 18 cm × 7 cm × 10 cm.

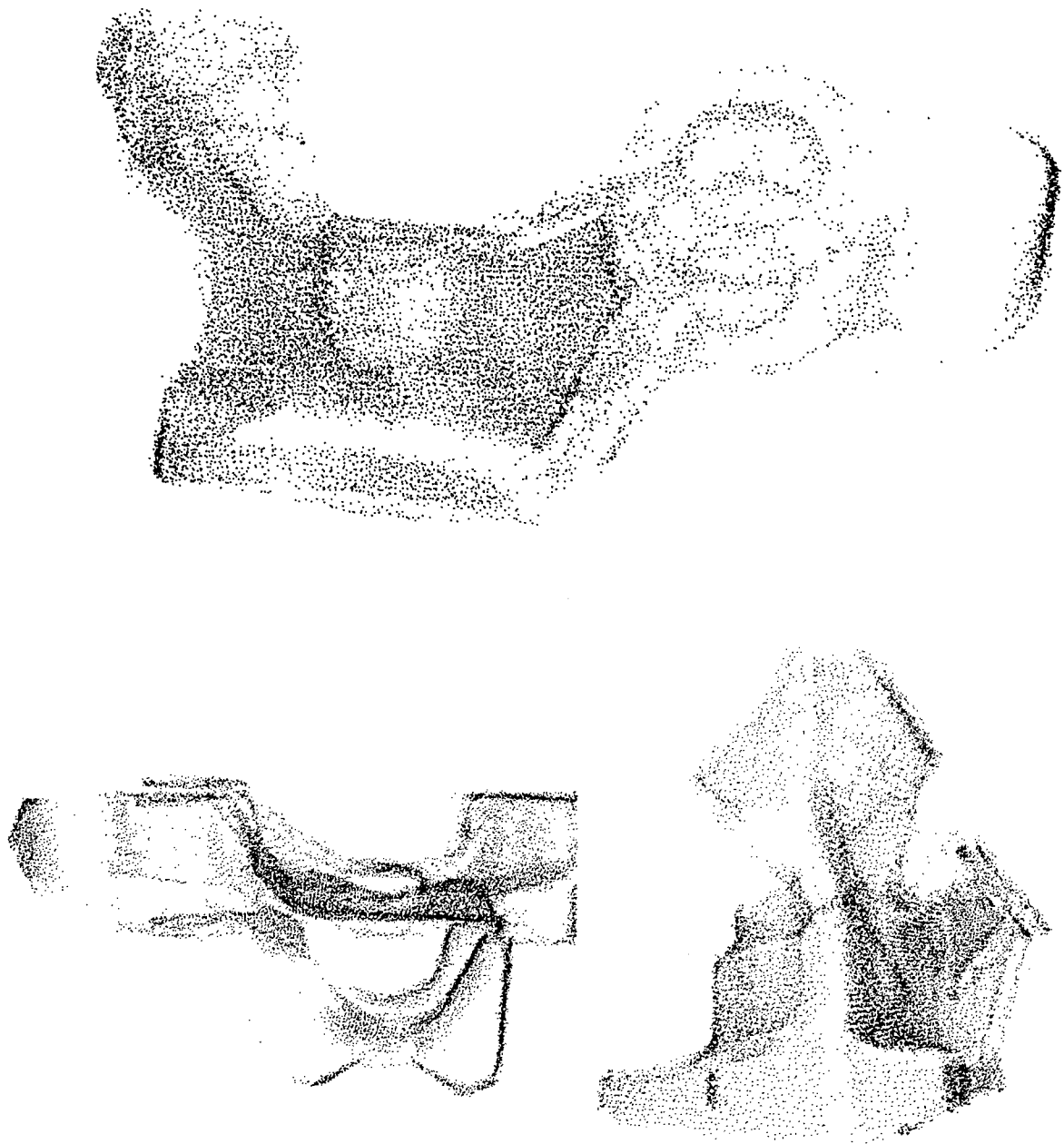

Figure 5-5: Combination of ten views taken from all sides of a Renault part. All three display the same 15,055 data from different angles.

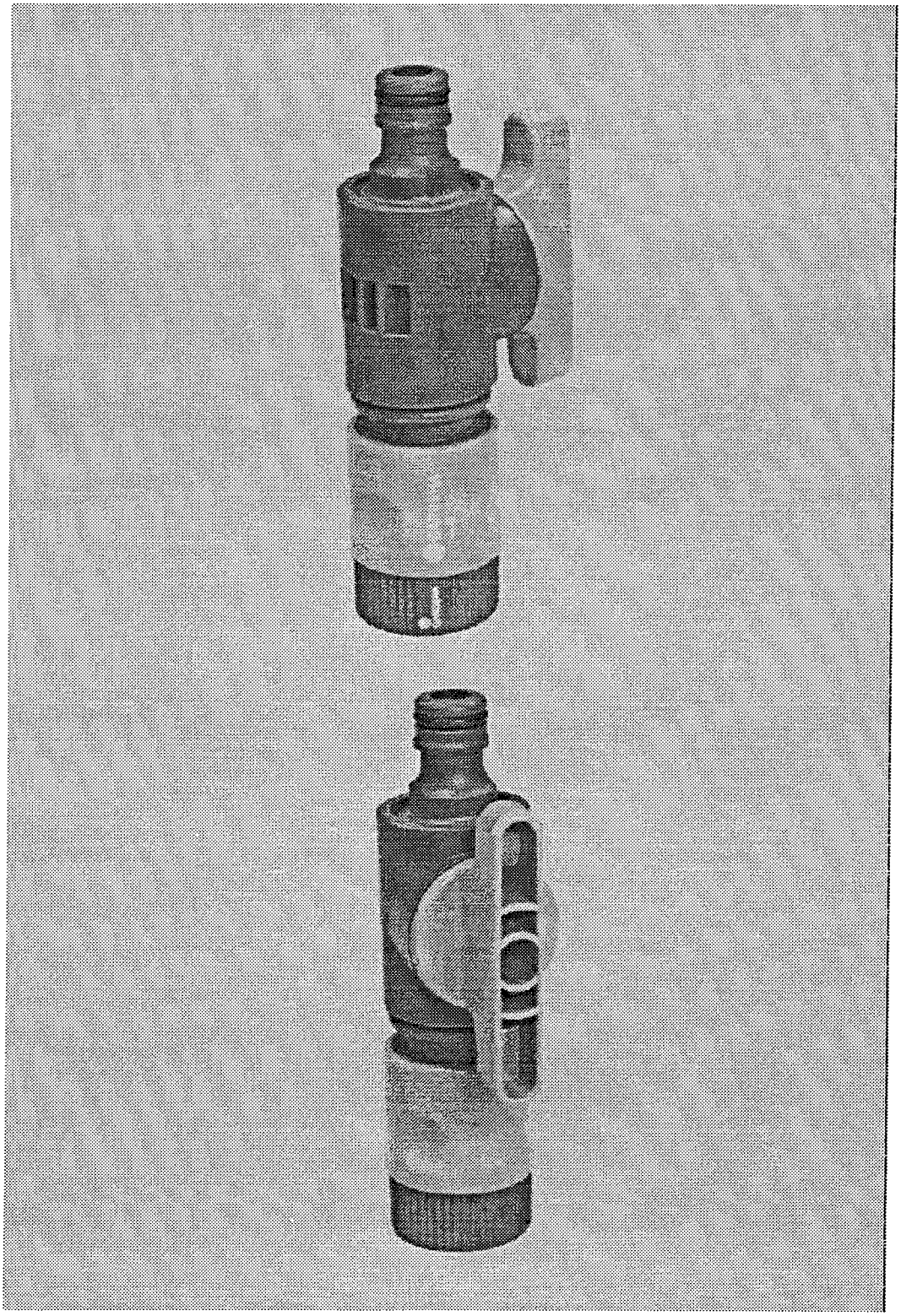

Figure 5-6: Images of the valve. Dimensions: 13 cm × 6 cm × 3 cm.

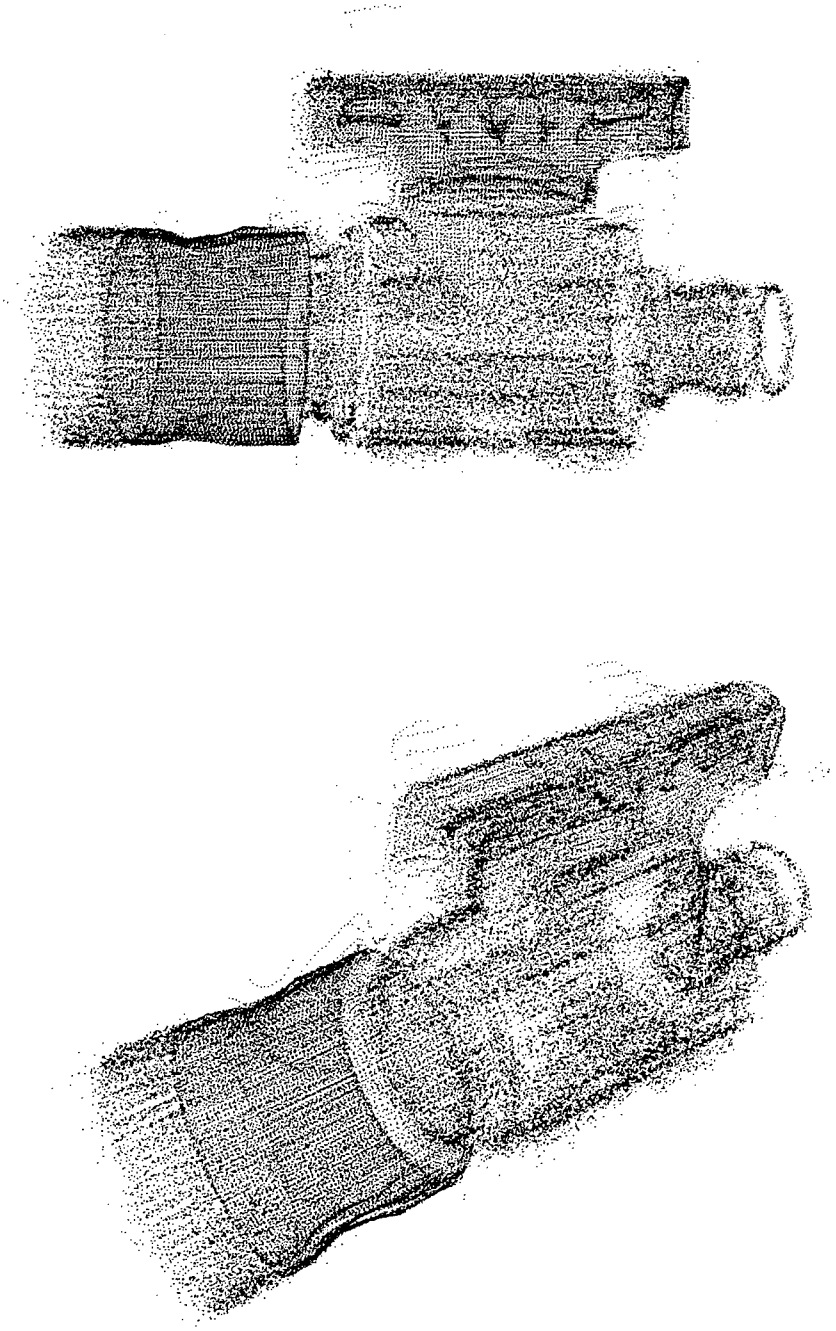

(Continued on next page)

(Continued from last page)

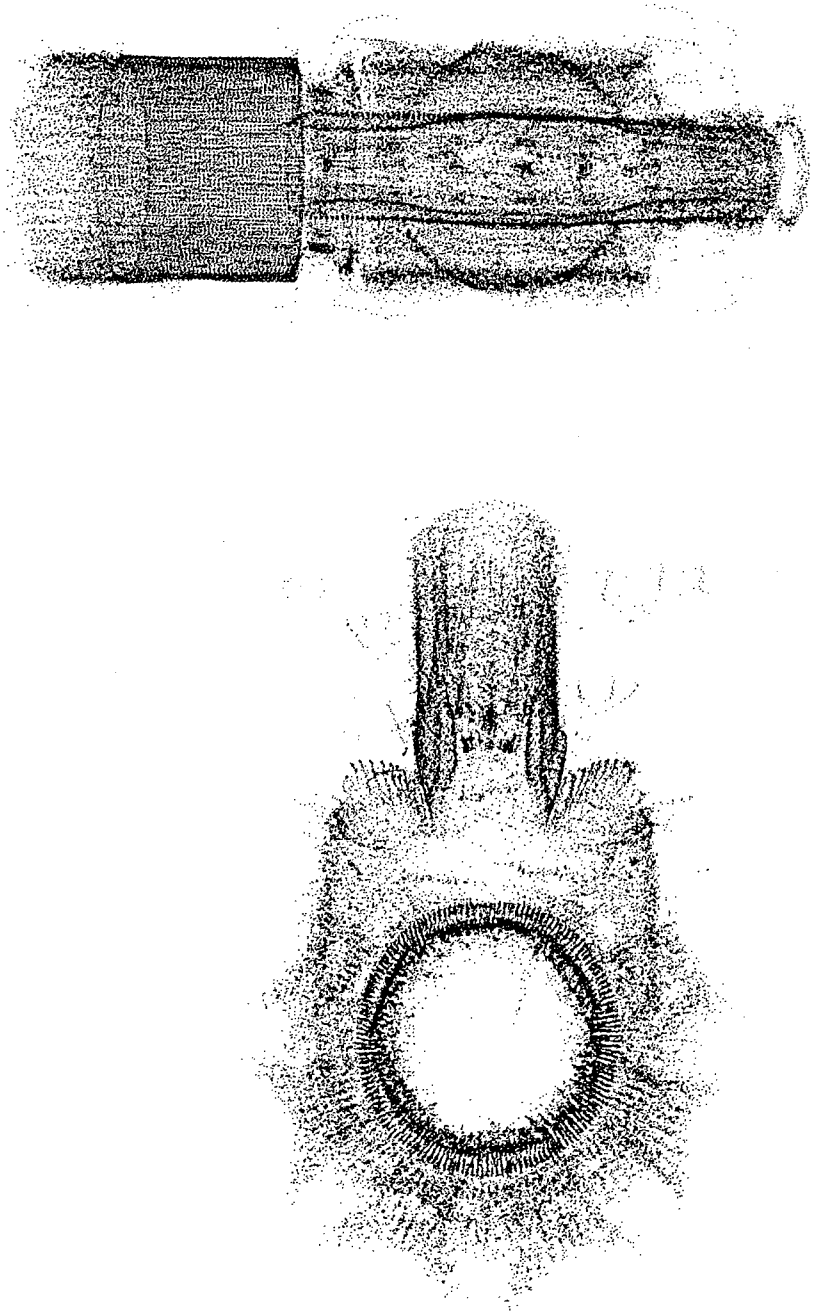

Figure 5-7: Combination of eight views taken from all sides of a valve. All display the same 52,854 data from different angles.

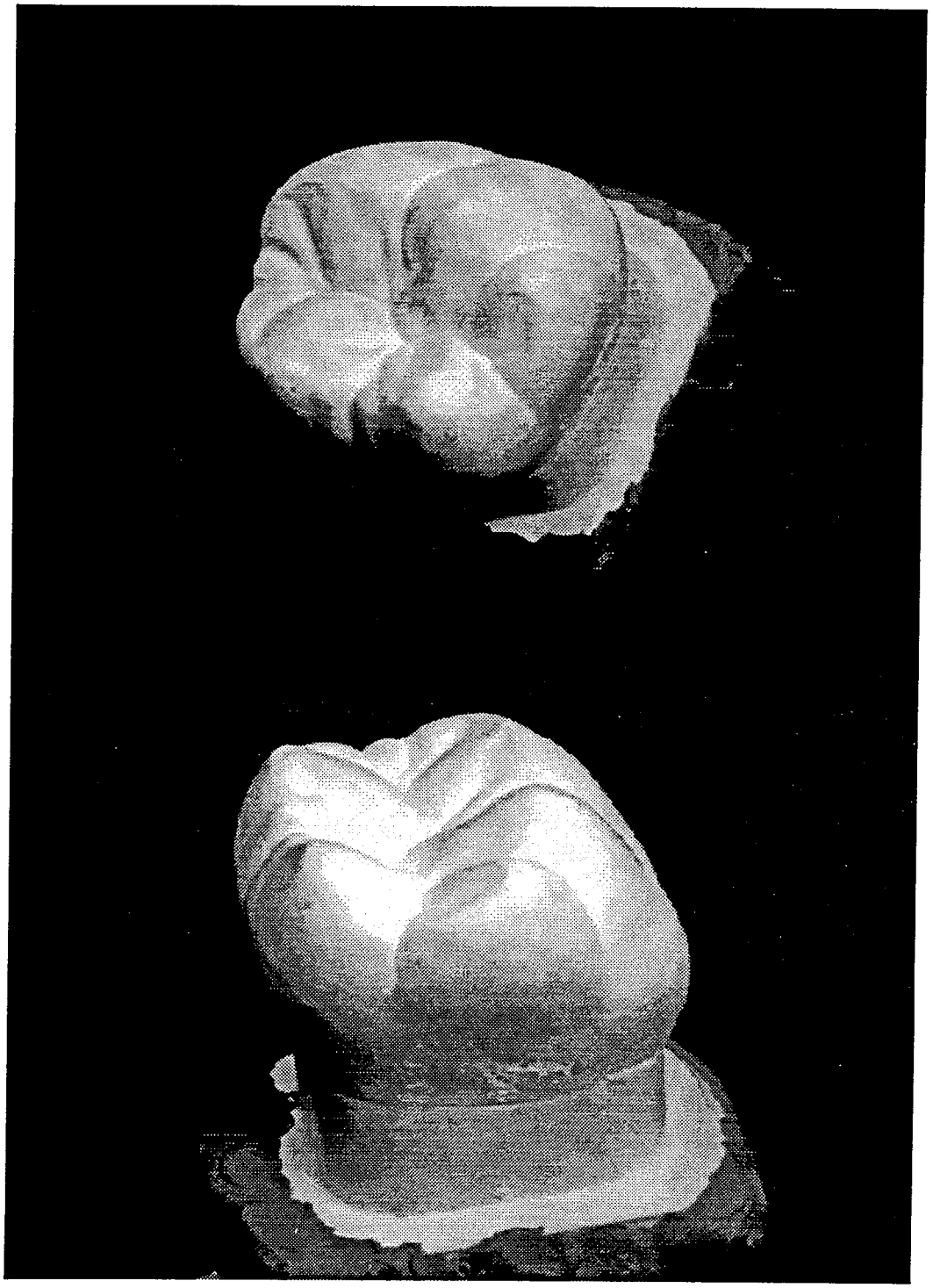

Figure 5-8: Images of the tooth model. Dimensions: 6 cm × 6 cm × 6 cm.

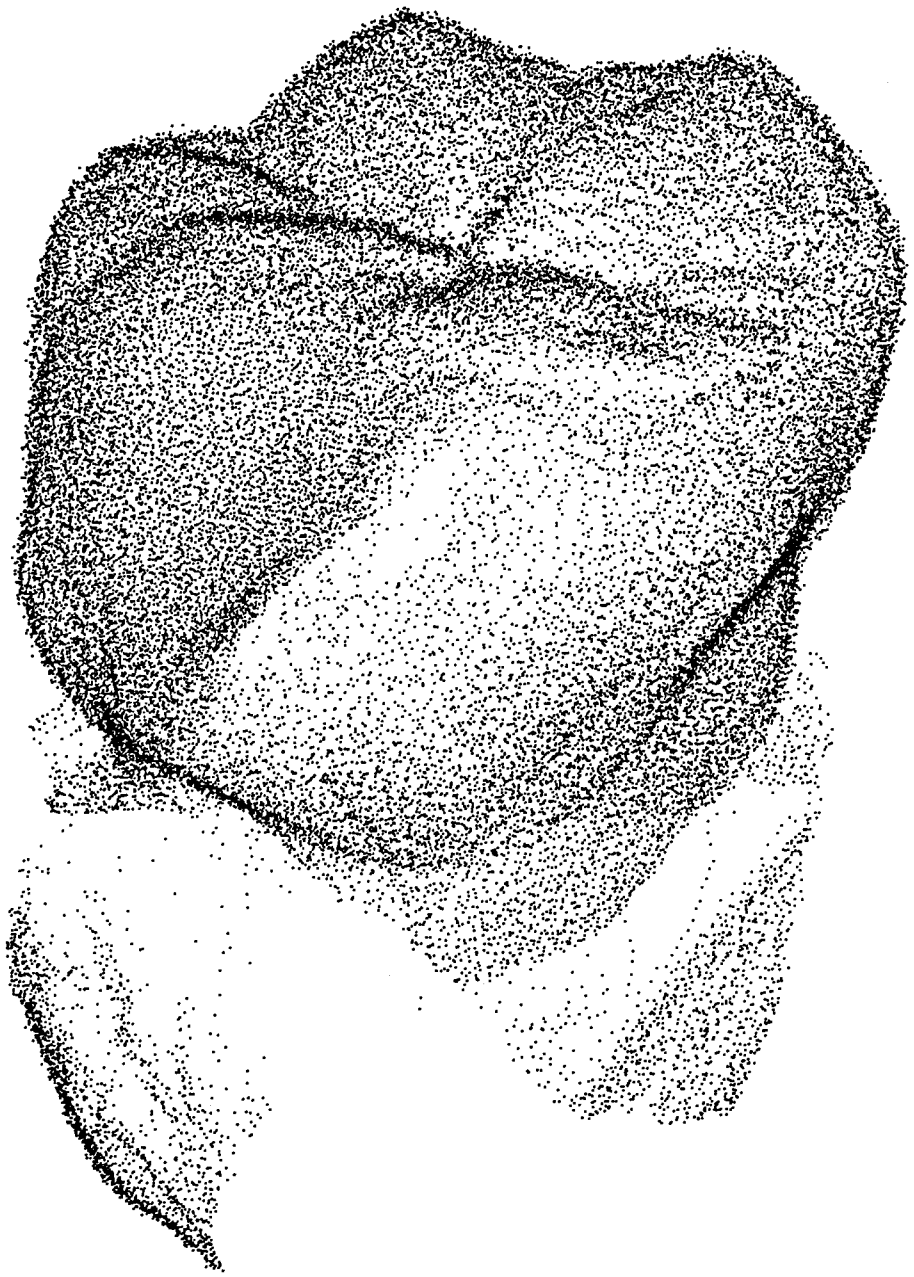

Figure 5-9: Combination of eight views (46,831 data) taken from all sides of the tooth model.

5.2 B-Spline Approximation

Figure 5-11 is a B-spline [39] approximation of Figure 5-10. Figure 5-12 is a shaded rendering of the B-spline approximation in Figure 5-11.

The B-spline approximation is adopted in displaying the data because local shapes of surfaces are not affected by data points farther away from the area. Because of this advantage, the B-spline approximation has been considered as a reasonable way to treat highly irregular and unpredictable surfaces (e.g., [28]), even though it has a tendency to smooth out the surface. A number of studies have been done on implementing the B-spline method to treat discontinuous surfaces. Some references can be found in [46].

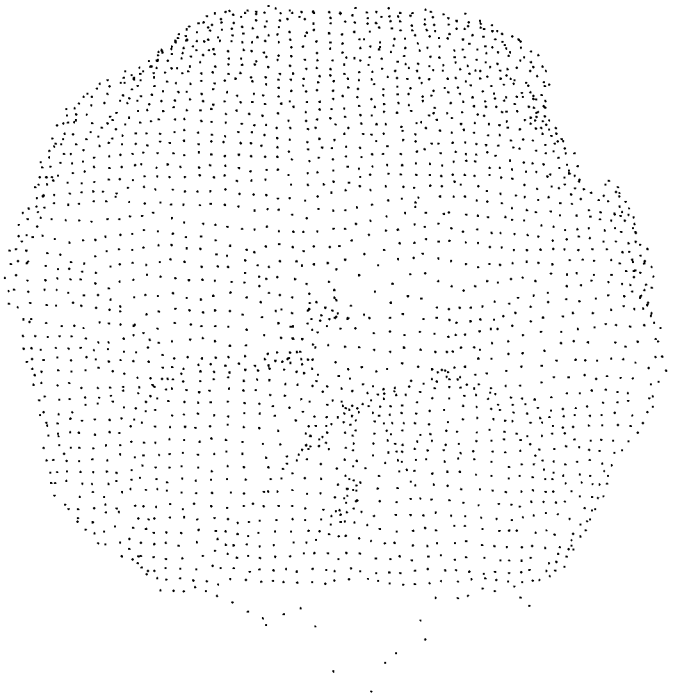

Figure 5-10: 3-D data acquired from one view of a tooth model

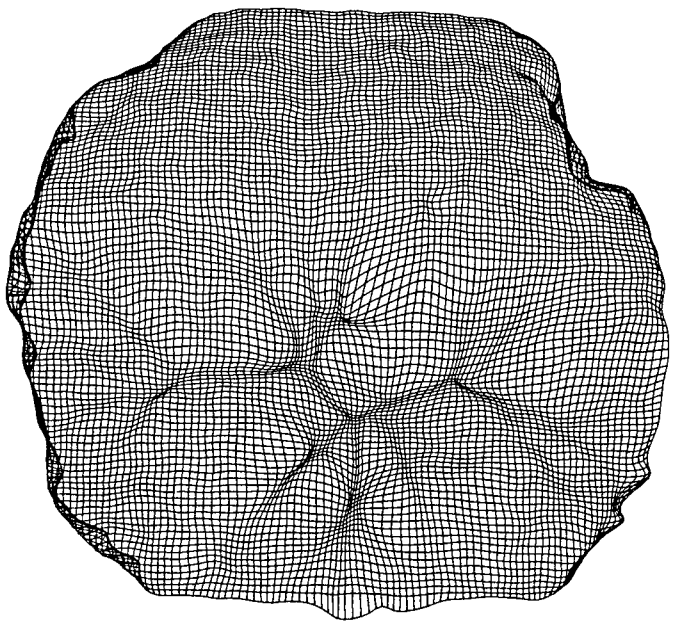

Figure 5-11: B-spline approximation of one view of the tooth in Figure 5-10

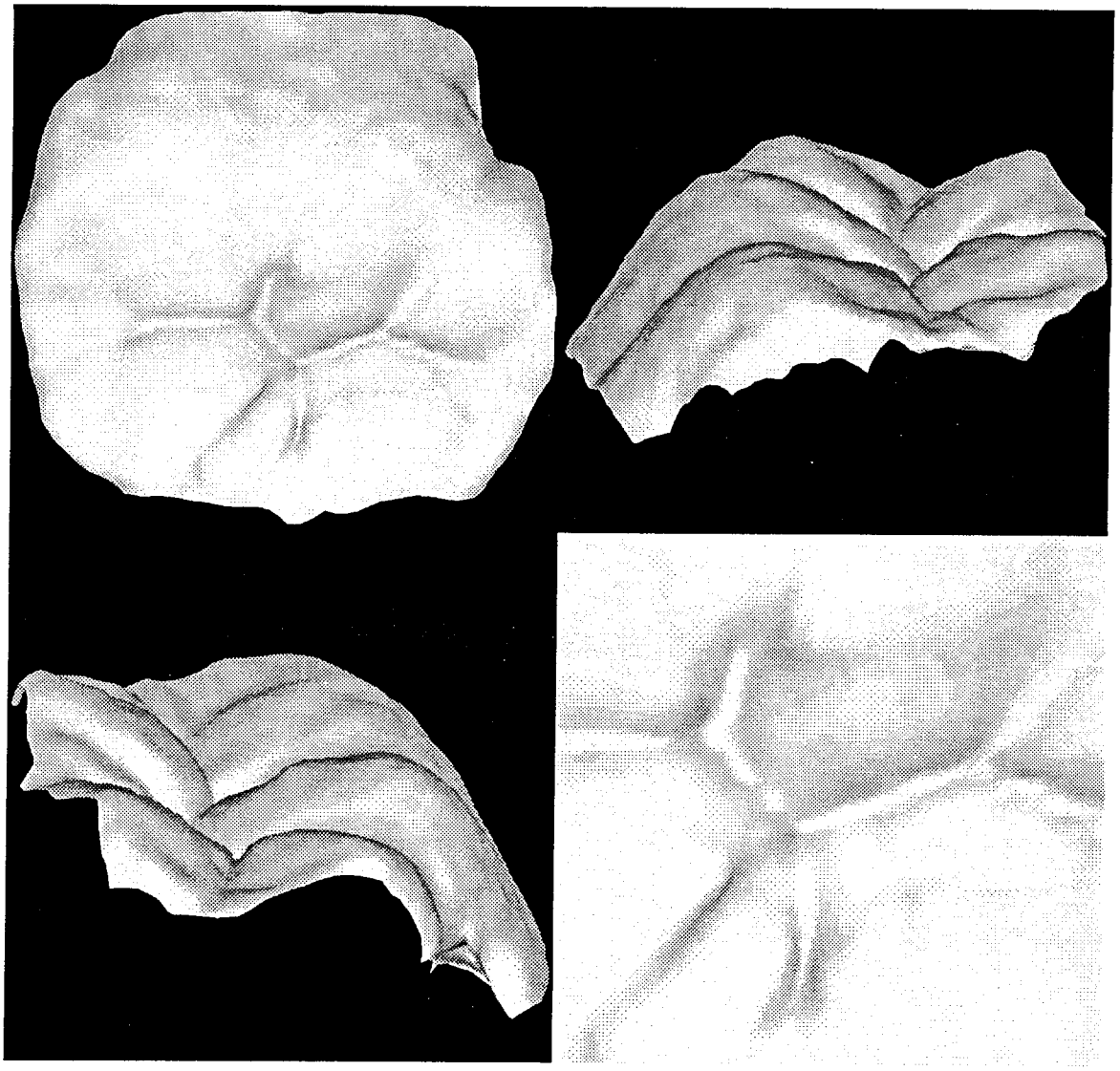

Figure 5-12: Shaded rendering of the B-spline approximation in Figure 5-11. All display the same shaded image but from different angles. The lower right is a close-up in the valley area of the upper left.

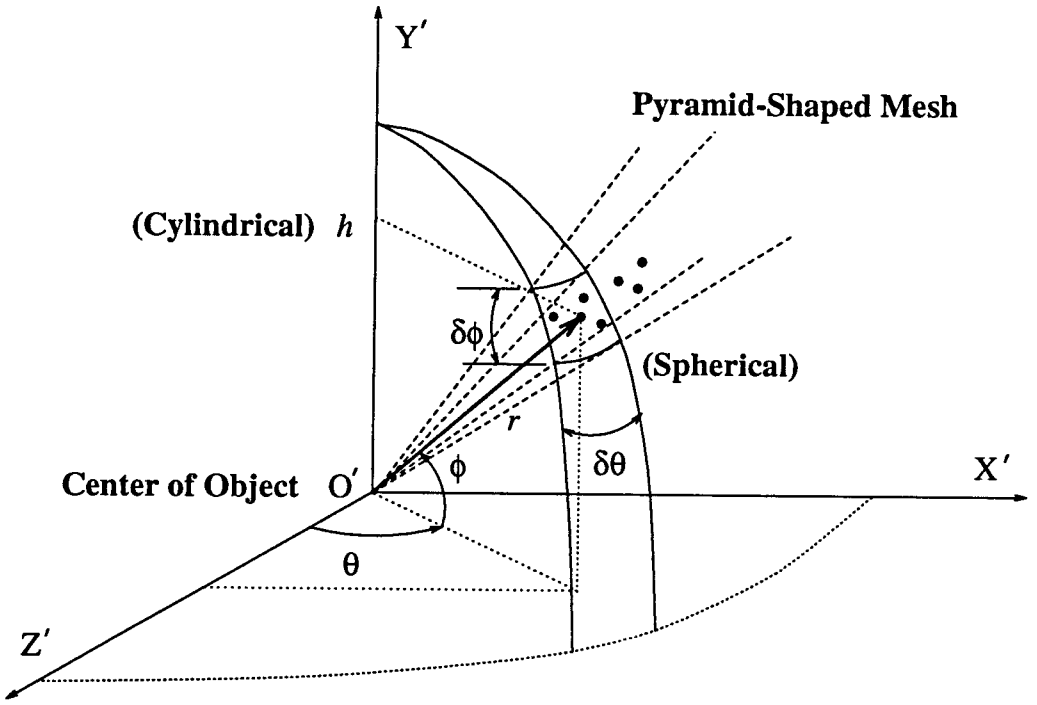

Figure 5-13: Spherical or cylindrical coordinate system used to solve merging problems

5.3 Multiple-View Merging

To get the whole set of data from different views organized appropriately to describe the object, one needs to solve the problem of multiple-view merging.

A straightforward method is adopted in this analysis. Either a spherical (r, θ, ϕ) or a cylindrical (r, θ, h) coordinate system (Figure 5-13) can be introduced with respect to the center of the object, whose world coordinates can be taken as the average of all data. Steps in azimuth (θ) and elevation (ϕ or h) can then be used to define pyramid-shaped meshes in which data are averaged to get a "representative" of the coordinates of the mesh, if the object is convex. It is obvious that the smaller the meshes, the better the details are preserved. The B-spline approximation is then applied to the resulting organized data.

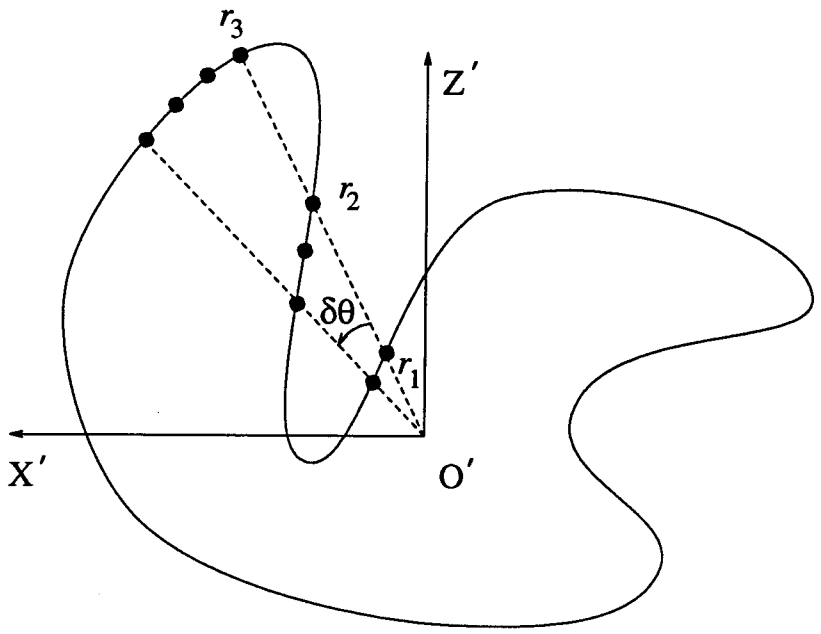

Figure 5-14: Concavity in merging problems

Concavity problems may be addressed by utilizing the information encoded in the radial coordinate r (Figure 5-14). The meshes are assumed to be so small and the data are so dense that the distances between two neighboring data are at the order of the system resolution. If the r coordinates of two data points with approximately equal θ coordinates are different from each other over several times of the system resolution, and there is no data between them, it is then either a sharp discontinuous case or the two data are on different sides of a concave surface (e.g., r_1 and r_2 in Figure 5-14). The former is less probable because the data are dense at the order of the system resolution, and anything in between the two data points may have been spotted already. The latter can be verified if other pairs of data similar to them exist. It is a nontrivial and interesting problem worth pursuing more rigorously.

Figures 5-15 and 5-16 show solid rendering of the complete tooth model. The hole on the top of the tooth is a residual effect from the B-spline approximation which may be eliminated by further programming. Because the meshes are very small near $\phi = 0$ or 180° compared to other regions, the B-spline approach becomes very sensitive to the noise present in the data, and therefore shows rugged appearance near the hole atop the tooth model. That region can do its B-spline approximation separately to give better surface simulation.

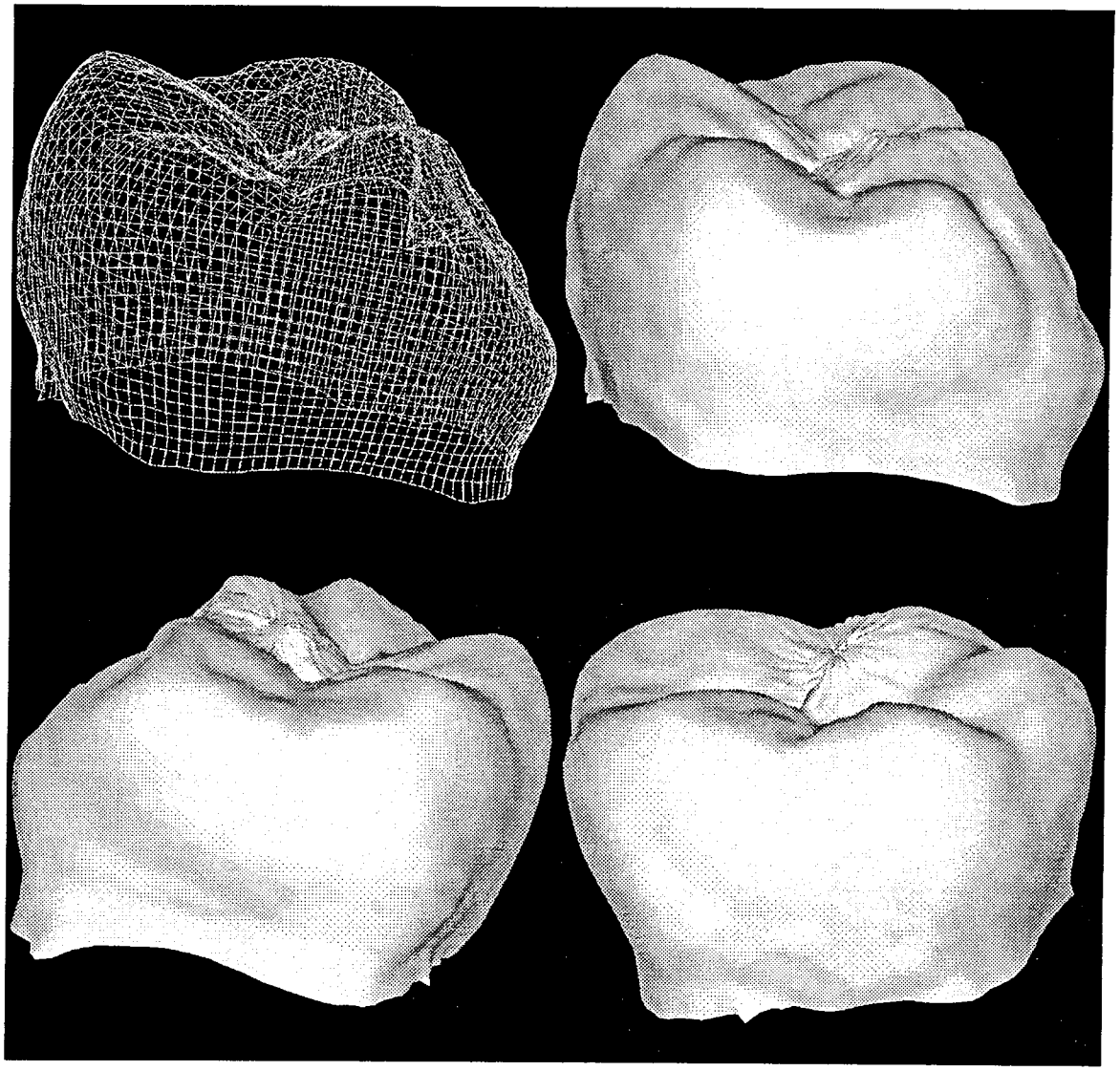

Figure 5-15: Shaded rendering of merged B-spline approximation of Figure 5-9. The upper left is a wire frame display of the solid model. The rest are the same shaded image looking from different angles.

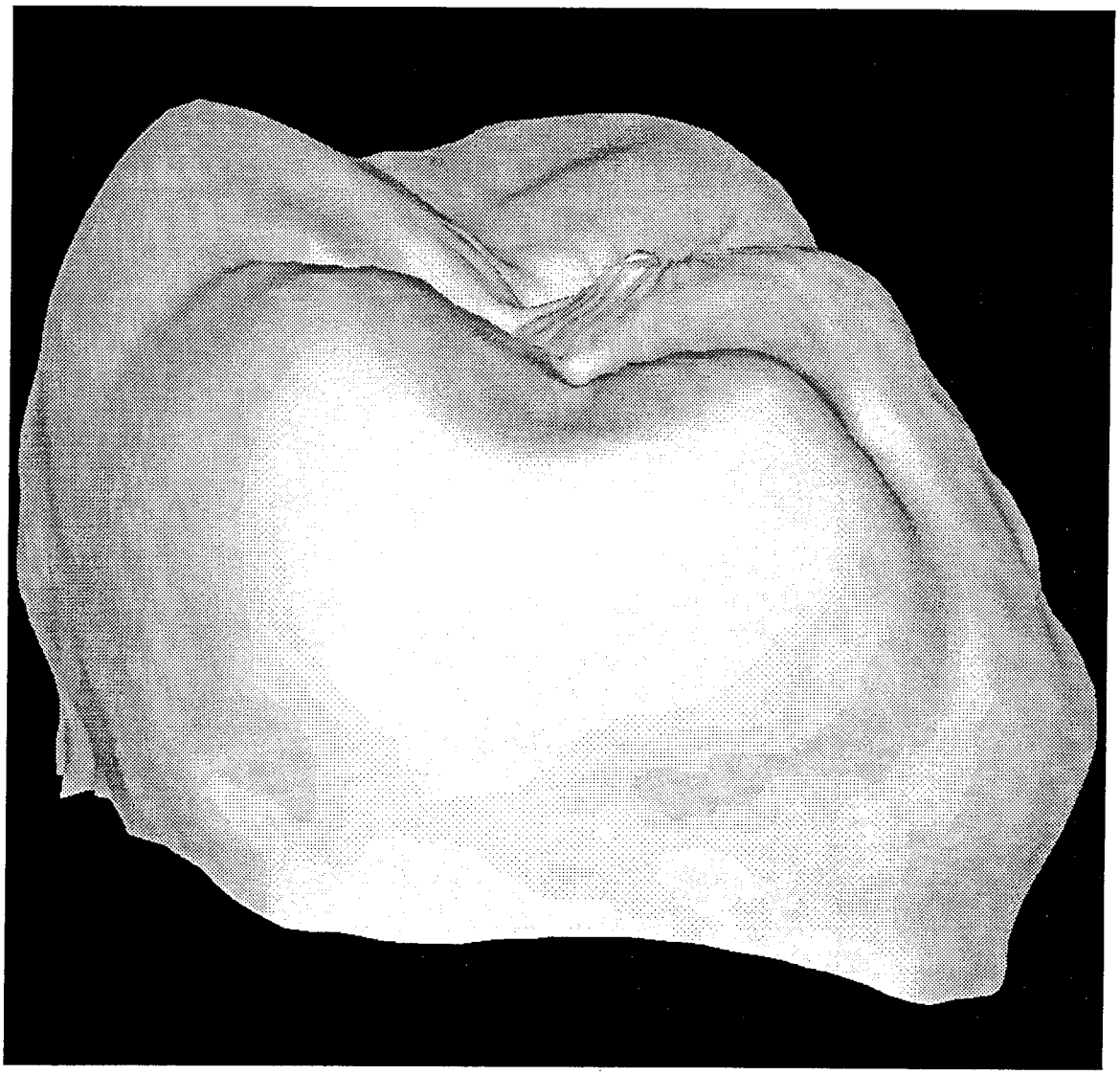

Figure 5-16: A blow-up of Figure 5-15

5.4 Multiple-View Registration

The finding of the rotation center (Section 5.1.1) does not solve the problem of registration completely due to the uncertainty in the directions of the rotation axes and the imprecision in the hardware. Some details of the tooth model are lost in Figures 5-15 and 5-16 due to the blur generated by unsatisfactory registration.

Researchers have proposed several approaches in solving the problem [10, 9, 22, 42, 49]. Chen and Medioni [13] propose an approach to treat the registration problem of range data. They find the rigid-body transformation between different views by minimizing a functional which does not require point-to-point matches. This algorithm is feasible for the SGA system, because in its 3-D shape measuring, it is highly improbable that the exact same small spot on the object can be scanned more than twice in different views. Even though a spot is scanned more than twice, it is very difficult to pin-point such data in an irregular crowd.

They consider matching two digital surfaces P and Q as shown in Figure 5-17, which are acquired from different views, by a rigid body transformation T with six unknowns. Initial guesses, however, are preferred in order to bring the surfaces in close proximity. The idea is to minimize a functional which is the sum of distances between $\vec{p}_k$, a data point on P, and an unknown point $\vec{q}_\ell$ on Q, which is also on the normal line of P at $\vec{p}_k$, to solve for the six unknowns. Finding $\vec{q}_\ell$, however, is an optimization problem itself. It is a problem of finding the intersection of a line and a digital surface. Writing $\vec{q}_\ell$ and $\vec{n}$ in parametric forms, $\vec{q}(i,j)$ and $\vec{n}(t)$, presents the problem more clearly.

$$\vec{q}(i,j) - \vec{n}(t) = 0,$$

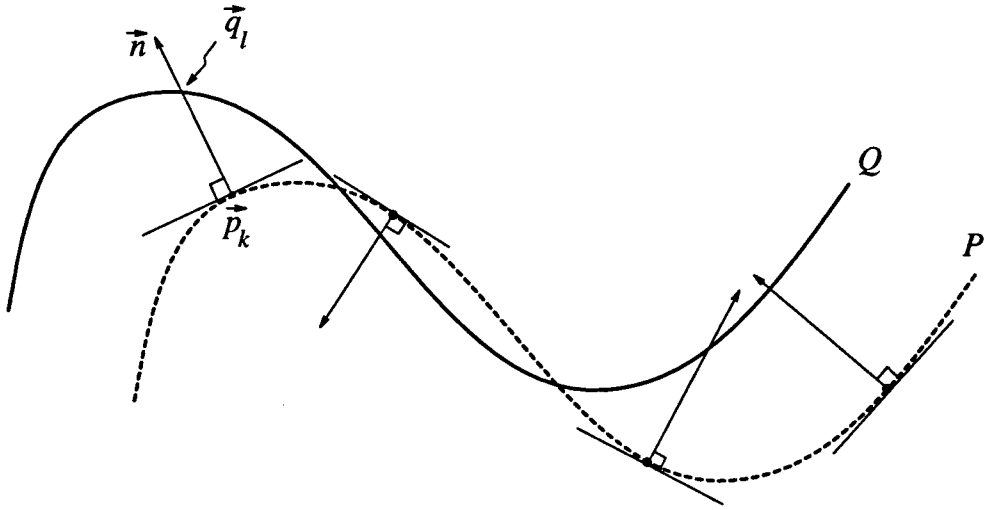

Figure 5-17: Matching two surfaces

which represents three simultaneous and nonlinear equations in three unknowns [40]. An iterative method is proposed in [13] based on Newton's method to speed up the process. It is a promising method, although it may have problems treating mostly discontinuous surfaces.

If the surface cannot be directly put into parametric form, the problem gets even more complicated. The following describes the problem the SGA system has when dealing with parameterizing surfaces.

5.4.1 Scanned Data vs. Range Images

Range data are similar to the data acquired by the SGA system — both of them contain XYZ information. However, they have a fundamental difference described below. Even if the scanner can be programmed so that it projects regular meshes on any surface, the light spots generated on the object are unlikely to be regular because the shape of the object

surface is unknown beforehand.

The following is a convenient way to look at the difference.

(1)

$$\text{Given } i,j \quad \Rightarrow \quad \begin{cases} X = f_x(i,j) \\ Y = f_y(i,j) \\ Z = f_z(i,j), \end{cases}$$

(2)

$$\text{Given } X,Y,Z \quad \Rightarrow \quad \begin{cases} i = f_i(X,Y,Z) \\ j = f_j(X,Y,Z), \end{cases}$$

where i and j are two parameters used to parameterize the surface. For image data, i and j can be the two axes on the CCD array, so both relationships are automatically available because of the *digital* nature of the cameras. In the SGA system, 3-D data are generated by the two *analog* detectors. After oversampling and photogrammetric triangulation, relationship (2) is not immediately obtainable because of the highly irregular data formation. Therefore, the 3-D data acquired by the SGA system are different in nature from those in image format widely adopted in robot/computer vision.

Without the inverse relationship (2), data processing becomes cumbersome. Most algorithms designed for image format have to be modified extensively and thus run much more slowly for these unstructured data. It is therefore highly desirable to transform them into a format similar to that of an image where both (1) and (2) are available, so that a link between the SGA system and the world of computer vision may be established.

Transforming SGA data format into that of image-based systems does not mean the SGA system is inferior. It is adopted simply because of the ease in processing huge amounts of

data and the availability of the algorithms. On the contrary, the SGA system is superior in acquiring 3-D data because only real-time measurements and simple calculations are involved as mentioned in Chapter 2, while some range finding systems require time-consuming image acquiring and matching processes to generate 3-D information yet only lower resolutions are sustained.

A parameterization process is discussed below to show that SGA data can be successfully transformed to fit into image processing algorithms once the correlation problem (2) is resolved.

5.4.2 Pseudo Range Image Parameterization

To parameterize the irregular 3-D data view by view, it is useful to define a plane of parameterization, onto which all data in a view can be projected with a 1-to-1 correspondence. This plane is defined through the Y scanner which scans on the YZ plane, as shown in Figure 5-18, and the X scanner which scans on the XZ plane. For any object, a mid-scan line can be found, which bisects the total viewing angle of scanners for the object. The plane of parameterization is then defined as any plane that is perpendicular to the mid-scan line, and is parameterized by equally-spaced (regular) points that have (i, j) as parameters.

The next step is to interpolate to get the XYZ coordinates of regular grid points on the plane of parameterization from the available irregular experimental data (Figure 5-19).

A simple way to look at the problem is to rotate the parametric plane and the object so that the mid-scan line is parallel to the Z axis (Figure 5-18, Y scanner position #2), i.e., $\zeta = 0$ and $\eta = 0$. The parameterization is thus simplified to be an orthogonal projection with respect to the Z-direction for the irregular data. The Z coordinates are found by

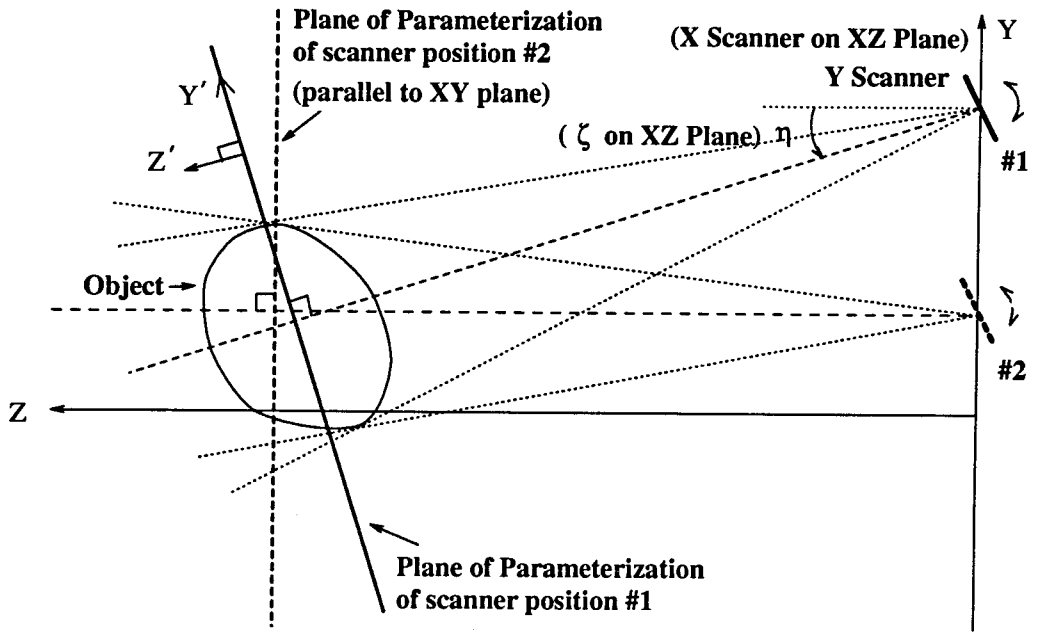

Figure 5-18: Relative positions between the Y scanner and the object to be scanned. A similar relationship can be found on the XZ plane, where ζ is in place of η, and the X scanner controls the direction of the light beam.

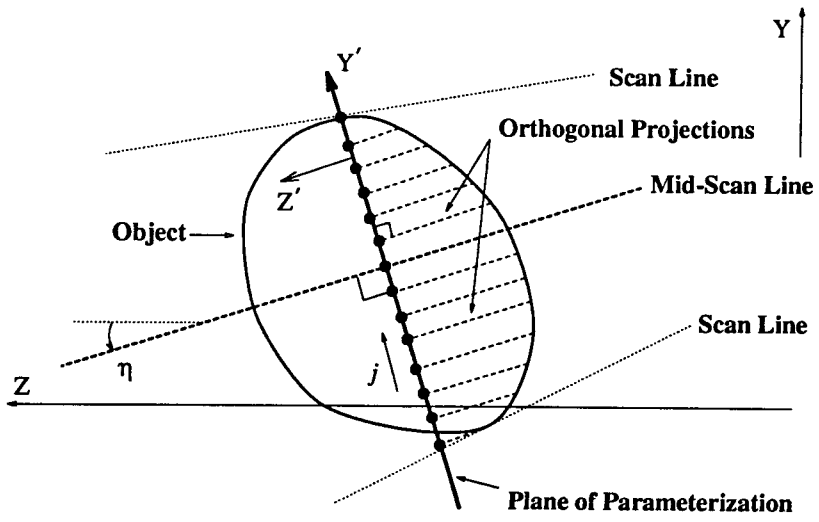

Figure 5-19: Parameterization of irregular data

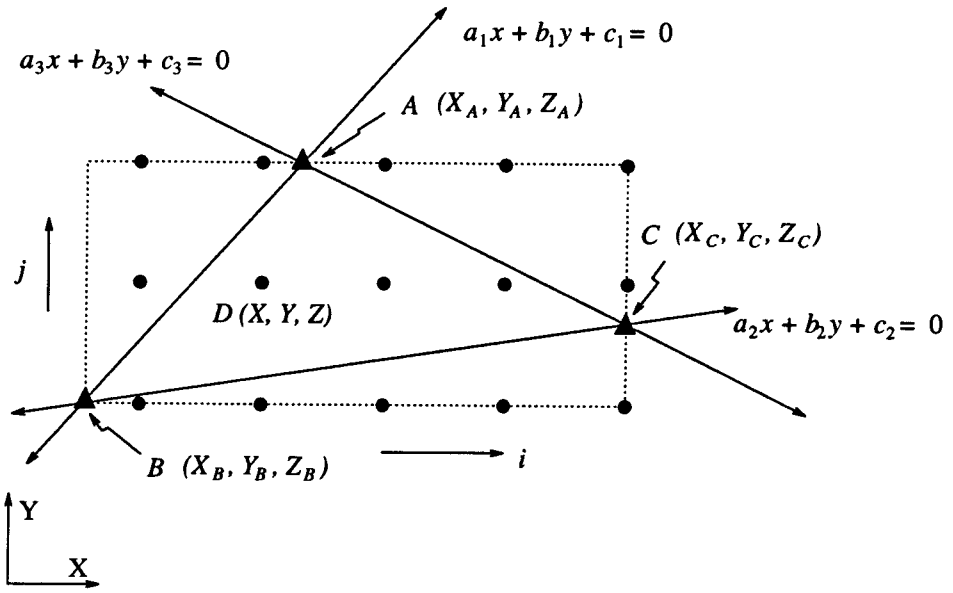

Figure 5-20: Relationship between regularized and experimental data

interpolating the regularized (X, Y) points. In Figure 5-20, considering all triangles formed by neighboring irregular experimental data, if any of the regular points $D(X, Y, Z)$ falls inside of $\triangle ABC$, the following three inequalities must be true:

$$\begin{aligned}
&(a_1X + b_1Y + c_1) \cdot (a_1X_C + b_1Y_C + c_1) \geq 0, \\
&(a_2X + b_2Y + c_2) \cdot (a_2X_A + b_2Y_A + c_2) \geq 0, \\
&(a_3X + b_3Y + c_3) \cdot (a_3X_B + b_3Y_B + c_3) \geq 0.
\end{aligned} \tag{5.1}$$

The Z coordinate of D is then interpolated from A, B and C by noting that they are co-planar:

$$\begin{vmatrix}
X - X_A & Y - Y_A & Z - Z_A \\
X_B - X_A & Y_B - Y_A & Z_B - Z_A \\
X_C - X_A & Y_C - Y_A & Z_C - Z_A
\end{vmatrix} = 0. \tag{5.2}$$

In case that the plane of parameterization is not parallel to XY plane, irregular data are orthogonally projected onto the plane which is tilted away from the Z direction by ζ on the XZ plane and η on the YZ plane, as shown in Figure 5-18. The interpolations are done similarly but with more tedious calculations. Rotation $\mathcal{R}(\zeta, \eta)$ is applied to the experimental (irregular) data A_{XYZ} to put them in the X'Y'Z' coordinate system. Equations 5.1 and 5.2 are then used on $A'_{X'Y'Z'}$ to parameterize the tilted plane by calculating $D'_{X'Y'Z'}$. $\mathcal{R}^{-1}(\zeta, \eta)$ is then applied to regularized points $D'_{X'Y'Z'}$ to get D_{XYZ} in XYZ coordinate system.

$$A'_{X'Y'Z'} = \mathcal{R}(\zeta, \eta)\ A_{XYZ} \quad \text{(irregular)},$$

$$D'_{X'Y'Z'}: \text{ Interpolate } A'_{X'Y'Z'} \text{ by Equation 5.1 and 5.2},$$

$$D_{XYZ} = \mathcal{R}^{-1}(\zeta, \eta)\ D'_{X'Y'Z'} \quad \text{(regular)},$$

where

$$\mathcal{R}(\zeta, \eta) = \begin{bmatrix} \cos\zeta & 0 & -\sin\zeta \\ -\sin\zeta\cos\eta & \sin\eta & -\cos\zeta\cos\eta \\ \sin\zeta\cos\eta & \cos\eta & -\cos\zeta\sin\eta \end{bmatrix}.$$

The reliability of this scheme depends on knowing the angles between the mid-scan line and the Z direction, i.e., η in the YZ plane and ζ in the XZ plane, which means it depends on the precision and accuracy of the scanners. Also, for an object with concave areas, the scheme can get very complicated because the orthogonal projections in Figure 5-19 may no longer be a 1-to-1 correspondence. In this case, orthogonal projection is not applicable any more, and projections parallel to the individual light beams may have to be considered.

Figure 5-21 shows a comparison between irregular experimental data and the "pseudo range image" data computed according to the above scheme.

The parameterization process is made easier if the original irregular data are in a 2-D array in which neighboring points are in real life close to each other. Otherwise, an extra process of "nearest neighbor spatial search" is necessary before interpolations are conducted. This problem is not trivial, but has been studied extensively. Delaunay triangulation (also known as Voronoi tessellation) [43], for example, has been used in dealing with similar problems in computer vision [21].

Any form of interpolation more or less reduces the fidelity of the data. The accuracy of the regularized data cannot exceed that of the original data and is limited by the distances between the original data. Therefore, the fidelity of the regularization depends on the sizes of the original irregular meshes. The denser the original data, the better the fidelity is preserved.

Parameterization is only a means to expedite the processing of data. To reduce the loss of fidelity, the original data may still be used in relationship (1) mentioned in Section 5.4.1, while the regularized ones serve in relationship (2).

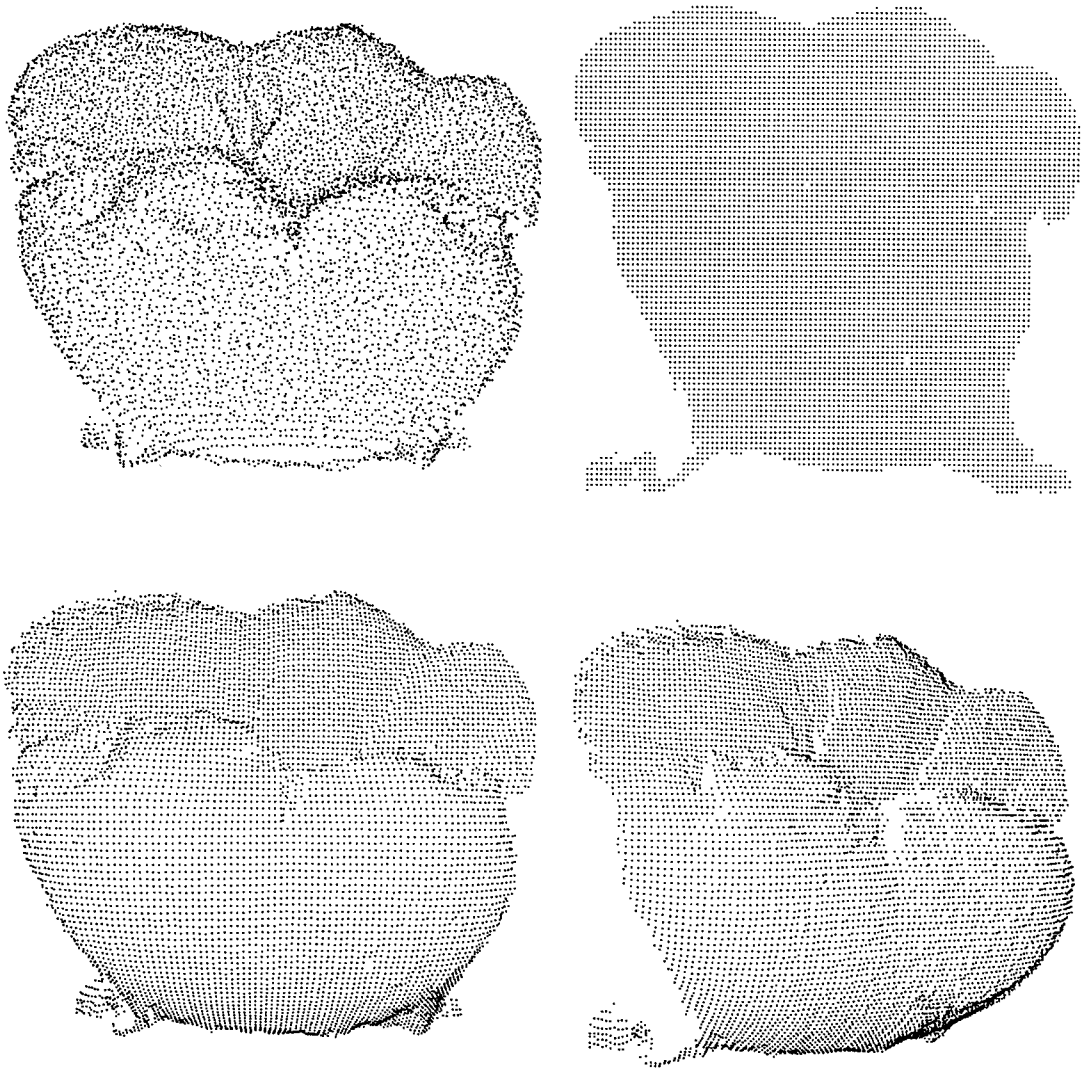

Figure 5-21: Comparison of experimental data and "pseudo range image" data of the tooth model. The upper left shows one view of the irregular experimental data obtained from the tooth. The upper right displays the orthogonal projection of the regularized data on XY plane. The lower left is a perspective display of the same regularized data. The lower right is a display from a slightly different angle to show some more details.

5.5 Future Work

- The use of a developed computer vision algorithm [13] to register the regularized data is underway. It is expected to give satisfactory results since the data can fit directly into the program and are high-quality 3-D (pseudo) range image data. Once good results are obtained, the next step is to develop a module program for directly processing the original data while using the regular ones as a look-up table to preserve the fidelity in the data as much as possible.

- It would be interesting to find a way to compare the difference between calculated output surfaces using all regularized data and using original data while making the regular ones serve as a look-up table. This may provide a way to define the degree of loss of fidelity and thus indicate the reliability of the registration process.

- The XY scanner is in fact not a point source. The outlet of the laser beam on the Y mirror may vary as the X mirror changes its orientation. Good optical alignment, however, can make it approach a point source. The position of this point source can be measured with more accuracy to define the plane of parameterization more appropriately if the scanners are attached to a vertical precision translation stage.

- It is assumed, when considering the registration and merging problem, that only rigid body transformations are involved. Since the light spots that are projected close to the edges of the lenses and/or the detectors may be seriously distorted, the deformation of data may cause the consideration of rigid body transformations to be insufficient. In this case, the deformation of data may be taken into account by, for example, weighting the data according to their locations or intensities. This should have been

compensated by the intrinsic calibrations of cameras, had the variations of intensities and other effects mentioned in Sections 3.4 and 3.5 been included. Although it makes the error maps much more complicated and harder to access, it is a necessary next step to make the data more reliable.

- The total amount of data this system is going to acquire and process in the future can be much more than was shown in Figures 5-5, 5-7, and 5-9. Since the parameterization is available, it is interesting to study the feasibility of existing feature extraction techniques in reducing the amount of data. Feature extraction is also helpful in providing geometric information for CAD/CAM processes.

Chapter 6

Conclusion

6.1 Summary

A non-contact 3-D surface geometry measuring system has been developed using an optoelectronic and photogrammetric technique based on stereo lateral-photoeffect diode detectors sensitive in the infrared range. An infrared beam is focused and scanned onto the surface of an object, thus a very small light spot is generated. The diffuse reflected light induces photocurrents in the detectors that are transformed into 2-D position signals at a rate of 10 KHz. The 3-D coordinates of the spot can be obtained by a photogrammetric triangulation with simple calculations. The stereo-correspondence problem is thus solved in real time. The resolution is based on a 12-bit A/D converter that digitizes 2-D photocurrents into 4,096×4,096. Oversampling is confirmed to help improve the resolution and repeatability significantly, up to eight times.

After camera intrinsic calibration, detector errors reduce to a maximum of 0.05% from the original 1.45% maximum. With an inter-camera spacing of 47 cm (1.5 ft) and a valid detector area of 3,201×3,201 du (25° viewing angle), the nominal viewing volume of this

system is approximately (22 cm)^3. Averaging 1,024 samples improves the repeatability and resolution eight times on the detector, thus the system resolves less than 9 μm (0.0004 in) from 47 cm away and maintains a 4.9 spots/sec sampling speed, while without oversampling the resolution is 57 μm (0.0022 in) from 47 cm away with a 5,000 spots/sec sampling speed. With the present hardware, a relative accuracy of $\pm$ 45 μm (0.0018 in) is maintained with 47 cm inter-camera spacing, while absolute accuracy is measured to be δX = 81 μm, δY = 46 μm, and δZ = 473 μm at the center of combined field of view. Both accuracies can be improved with appropriate hardware. Placing the cameras closer together, resolution less than 9 μm can be obtained, while larger volumes than (22 cm)^3 can be measured by increasing the inter-camera spacing.

Surface geometries of several objects have been measured and very high quality data are obtained. Methods of merging and regularizing the output data have been proposed, thus establishing a link between this system and the world of computer vision.

The performance of the system is comparable to the best aspects of each existing system, while maintaining high repeatability and high speed at the same time, which is not achievable by other systems. An important advantage is its adaptive scanning capability. Since the system can determine the 3-D coordinates of a point anywhere in the combined fielf of view, and can measure points in any order, it is possible to analyze the data stream from the system during acquisition and adaptively scan the light spot in response. By adopting photogrammetry, the 3-D reconstruction is only a function of the inter-camera spacing and the binocular convergence angles, which are static. The system is non-contact, so it can be used during the manufacturing process, and it is able to resolve more detail at comparatively large stand-off distances.

The limitations of the system are as follows. The reflection and diffuse properties of the surface of the object to be measured are crucial for this system, as for the other optoelectronic range finders. Therefore, there are certain surfaces that the system cannot measure, e.g., very specular surfaces. Very dark surfaces are hard to measure, too, because the system needs a bright enough light spot to make the measurement. In addition, this system does not give color information about an object. Because only one spot is measured at a time, the system cannot measure dynamic objects if the motion is faster than the total scan rate. Some internal reflections may generate more than one spot on the object, so that incorrect intensity-weighted centroid may be rendered, but the skew vector calculated by the photogrammetric triangulation is able to filter most of them out.

6.2 Outlook

With the system being able to routinely take measurements and to put data into "pseudo range image" format, a number of data acquisition and processing problems are waiting to be explored. Multiple-view registration, outlier detection, feature extraction, and concave or discontinuous surface measurement and data interpretation are topics that have been studied by researchers for many years. It will be interesting to study the application of data generated by the system to these existing computer-vision methods.

A "smart" scanning algorithm that saves time by tracing object boundaries instead of blindly searching for good reflections needs to be developed to reduce the measuring time, especially when very dense data are to be acquired.

The intrinsic calibration process still leaves something to be desired. The mechanical

and optical alignments can be improved by more precise and easily adjustable hardware. Some uniform noise patterns in the error maps may be traced back to the electronics. Any systematic bias should be eliminated. The incorporation of effects from intensity variations into the error maps will provide further understanding of the system and contribute to higher reliability.

An extrinsic calibration process is in order. The current triangulation algorithm used depends on an accurate inter-camera spacing and precise information about the orientations of the cameras. Using the many acquired 3-D data enables an optimization process to back-calculate the above information, thus making the system more flexible in acquiring 3-D data with various camera orientations.

The high resolution of the system should be tested further by measuring smaller objects at closer range. The surface features, e.g., scattering and material, are important factors for a good measurement and thus are worth exploring in more detail.

It is expected that the general problem will not yield the same levels of accuracy achievable with the carefully prepared experimental specimens. The capability to automatically acquire high-resolution quantitative measures of surface geometries for a wide variety of shapes, however, will have a significant impact on design and manufacturing processes.

Appendix A

Besl's Figure of Merit Comparison

Besl [8] has compared 59 different range measurement systems. He defines a figure of merit, that strongly depends on the sampling speed of each system but is independent of application-specific factors such as stand-off distances and the field of view:

$$M \equiv \frac{1}{\sqrt{T}} \; \frac{L_r \; [\mathrm{m}]}{\sigma_r \; [\mathrm{m}]}, \tag{A.1}$$

where T is the pixel dwell time, L_r is the depth of field, and σ_r is the "range accuracy."[1]

The SGA system is not pixel-based, so T is re-defined to be the time required to sample one light spot:

$$T \; [\mathrm{sec/spot}] = 0.0002 \; [\mathrm{sec/sample}] \cdot (\mathrm{number \; of \; samples/spot}).$$

The depth of field, L_r, is the diagonal of the approximately cubic viewing volume in the Z-direction. In the following calculations, the inter-camera spacing is set at 47 cm, which

[1] σ_r in Besl's paper is in fact the standard deviation of oversampling. It is *not* a kind of "accuracy"; it is a measure of "repeatability."

results in a viewing volume of $(23.5\text{ cm})^3$. Because of the cut-off on the detectors due to nonlinearity, the viewing volume is reduced to approximately $(22\text{ cm})^3$. Therefore,

$$L_r = 0.22\sqrt{2}\ \text{[m]}.$$

σ_r is in fact the standard deviation of the range measurement:

$$\sigma_r\ \text{[du]} = \frac{\sigma_u\ \text{[du]}}{\sqrt{5}},$$

$$\sigma_r\ \text{[m]} = \sigma_r\ \text{[du]}\ \ \frac{L_r\ \text{[m]}}{3,201\ \text{[du]}}, \tag{A.2}$$

where σ_u is the standard deviation of oversampling on the detector u-axis (average of σ_u's of both cameras in Table 3.3), and 3,201 du is the total valid detector units on u-axis. Combining Equations A.1 and A.2,

$$M = \frac{1}{\sqrt{T}}\ \ \frac{3,201\ \text{[du]}}{\sigma_r\ \text{[du]}}. \tag{A.3}$$

Table A.1 lists the results of the above calculations for 1, 16, 128 and 1,024 samples/spot measurements.

Figure A-1 shows a comparison of the SGA system to others. This diagram (without the data for the SGA system) was first shown in [8]. It shows figures of merit against range accuracies for 59 systems. A higher figure of merit and a smaller range accuracy indicate a better system. Thus the highest quality systems are those closest to the upper-left corner.

The envelope on the figure indicates how the SGA system performs for inter-camera

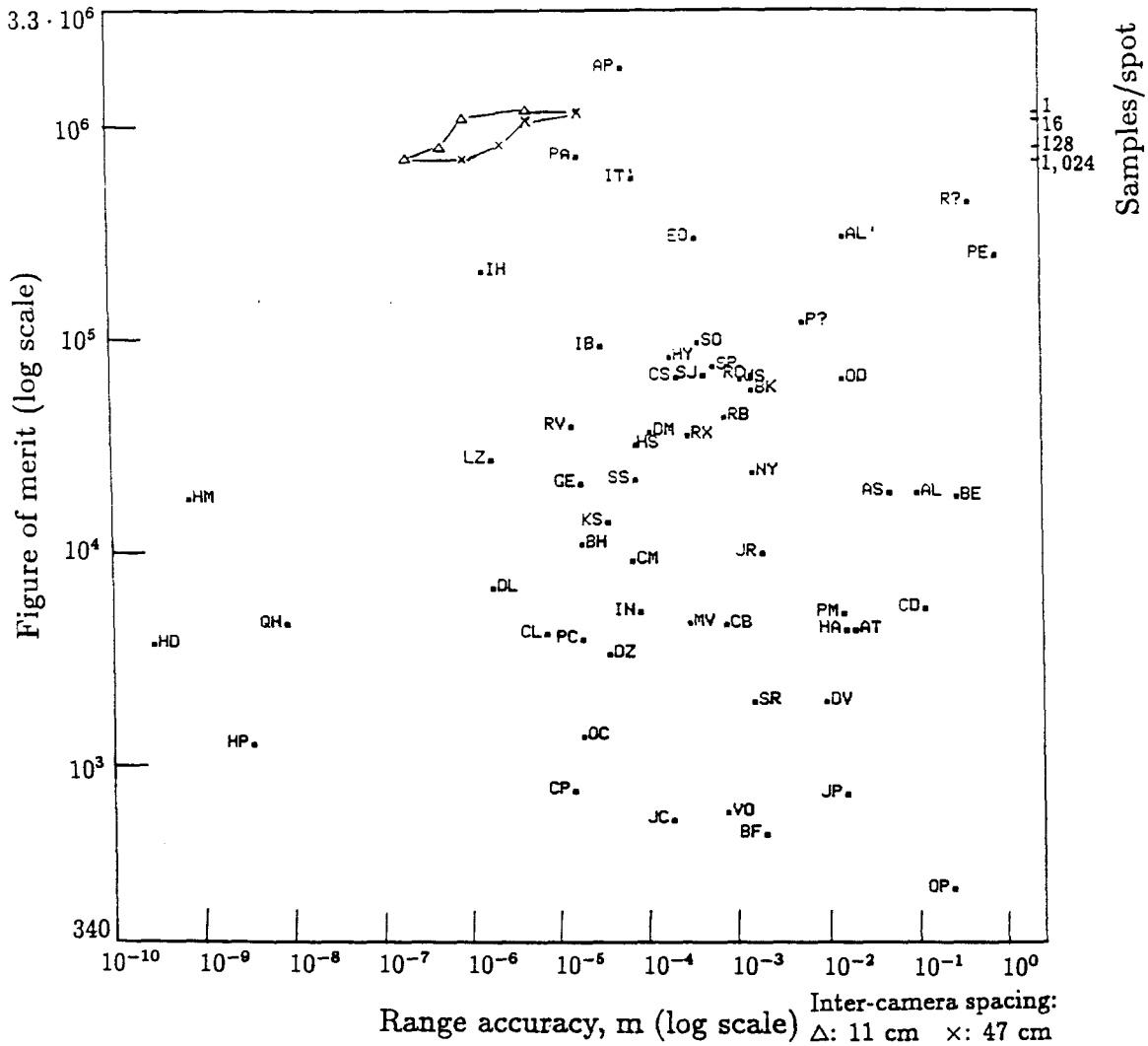

AL - Erim-ALV
AL'- New-Erim-ALV
AP - RVSI-APOMS
AS - Erim-ASV
AT - ATT:Miller,Wagner
BE - Boulder-EO
BF - Beheim-Fritsch
BH - Bickel-et-al
BK - Boyer-Kak-Color
CB - Cotter-Batch
CD - Cathey,Davis
CL - CyberOptics-LRS
CM - CMU:Kanade-Fuhrman
CP - CyberOptics-PRS
CS - Chavel-Strand
DL - Diffracto-LaserProbe
DM - Hersman-DO-Metrol
DV - Hersman-DO-Vision
DZ - Diffracto-Z-Series
EO - EOIS:Fitts
GE - GE:Mundy-Porter
HA - Heikkinen,Ahola
HD - Dandliker-Thalmann
HM - Matthews-et-al
HP - Pantzer-et-al
HS - NYIT:Halioua-Srini
HY - Hymarc-Hyscan
IB - ITI:Boehnlein-Harding
IH - ITI:Harding-Goodson
IN - Forstner-Indusurf
IT'- New-Erim-ITA
JC - Jalkio-Kim-Case
JP - JPL:Lewis-Johnston
JR - Jarvis-83
KS - Kern-SPACE
LZ - Lorenz
MV - Mapvision-Haggren
NY - NYU:Intensity-Ratio
OC - Octek-Eyechrometer
OD - Odetics-Inc
OP - Optech:Larsen500
P? - Perceptron-Radar
PA - Photonic-Automation
PC - Perceptron-Contour
PE - Perkin-Elmer
PM - Pipitone-Marshall
QH - Hariharan
R? - RVSI-Ross
RB - NRCC:Rioux-Blais
RC - RCA:Rosenfeld-Tsiks
RV - RVSI-other
RX - NRCC:Rioux
SJ - ServoRobot-Jupiter
SO - Selcom-Optocator
SP - Solid-Photography
SR - SRI:Nitzan,et-al
SS - ServoRobot-Saturn
VO - Vuylsteke,Oosterlinck
WS - Tech-Arts-White

Figure A-1: Besl's diagram [8]

Number of samples	1	16	128	1,024
Depth of Field, L_r [m]	$0.22\sqrt{2}$			
Time, T [sec/spot]	0.0002	0.0032	0.0256	0.2048
Standard deviation, σ_u [du]	0.444	0.117	0.057	0.023
Range accuracy, σ_r [m]	1.93e-5	5.09e-6	2.48e-6	1.00e-6
Figure of merit, M	1.14e6	1.09e6	8.00e5	6.87e5

Table A.1: Calculations of figure of merit

spacings between 11 cm and 47 cm. Note that the range accuracy varies with the inter-camera spacing (Equation A.2), but the figure of merit is not affected by it (Equation A.3). This envelope can expand towards larger range accuracy because the SGA system is capable of measuring much larger ranges than 47 cm.

It is obvious that the SGA system out-performs all other systems included in Besl's analysis in the combination of figure of merit and range accuracy. Some systems have much better range accuracies but operate at a much slower speed or with a very short depth of field. There is one with a higher figure of merit due to high speed or large depth of field, but has a worse range accuracy.

Appendix B

Rotary Table and Goniometer Motion

In this appendix I will discuss the trajectories of signals on the detector due to motions of the rotary table and goniometer in the camera intrinsic calibration (Section 4.1).

In Figure 4-2, when the rotary table rotates between $-15°$ and $15°$ with the goniometer fixed, a section of half of a hyperbola is generated on the detector, as shown in Figure B-1. β is the angle of the goniometer which is fixed on the trajectory. γ is the angle that the rotary table travels. f is the principal distance of the camera. The hyperbolic trajectory can be understood by noting that

$$\frac{\mathrm{u}}{f} = \tan\gamma, \quad \frac{\mathrm{v}}{d} = \tan\beta, \quad d = \frac{f}{\cos\gamma}.$$

Combining them gives

$$\left(\frac{\mathrm{v}}{f\tan\beta}\right)^2 - \left(\frac{\mathrm{u}}{f}\right)^2 = 1.$$

Therefore, in order to generate horizontal straight lines on the detector for error mapping, β has to keep changing as γ sweeps across $-15° \sim 15°$. In Figure B-1, let β' be the

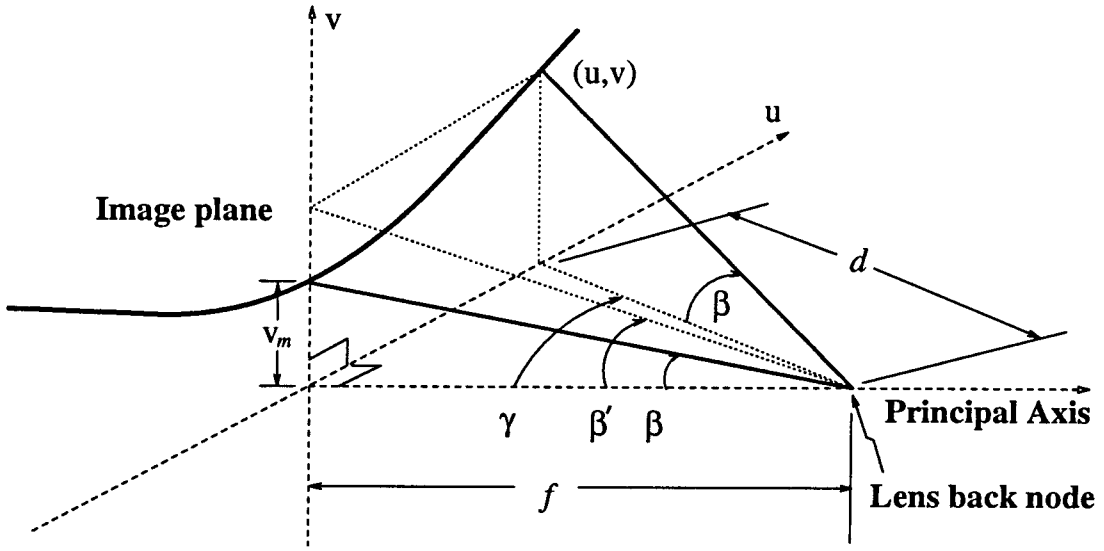

Figure B-1: Relationship of β', β and γ

regular angular step assigned by the calibration program,

$$\tan\beta' = \frac{v}{f},$$

$$\beta = \tan^{-1}\frac{v_m}{f} = \tan^{-1}\frac{v}{f'} = \tan^{-1}\frac{v\cos\gamma}{f} = \tan^{-1}(\tan\beta'\cos\gamma).$$

Thus the goniometer angle β must change with γ if β' is to be fixed in order to generate error maps with meshes enclosed by straight lines.

Appendix C

Error Maps of Camera #1

In this appendix error maps of camera #1 are shown. Those of camera #2 are displayed in Section 4.4.

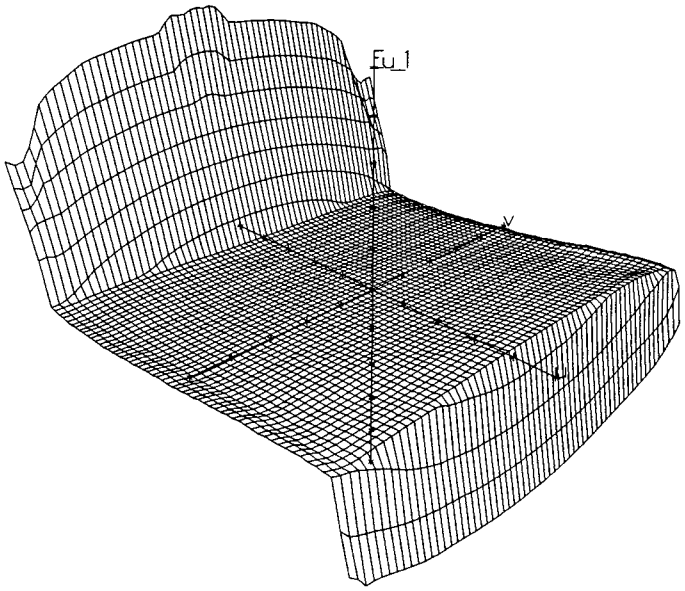

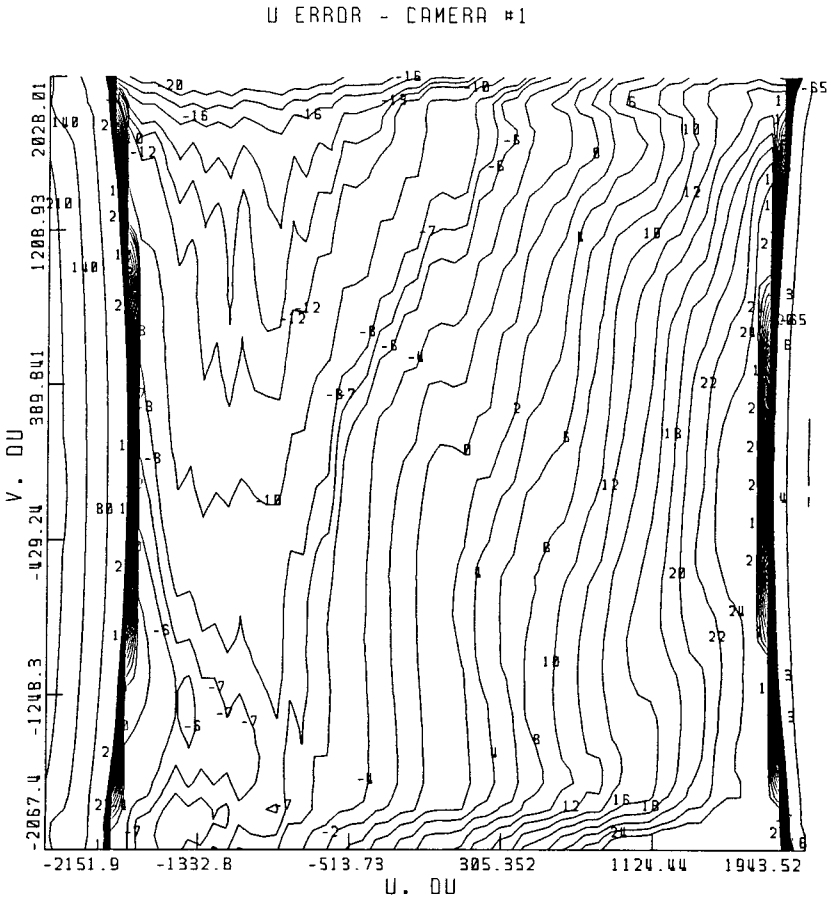

Figure C-1: u *error map of camera #1. The upper one shows the error surface. The lower one is the contour map.* u*: −2010.442 ∼ 1887.870 du,* v*: −1962.442 ∼ 1953.202 du,* E_{u1}*: −135.584 ∼ 284.666 du (7.27%).*

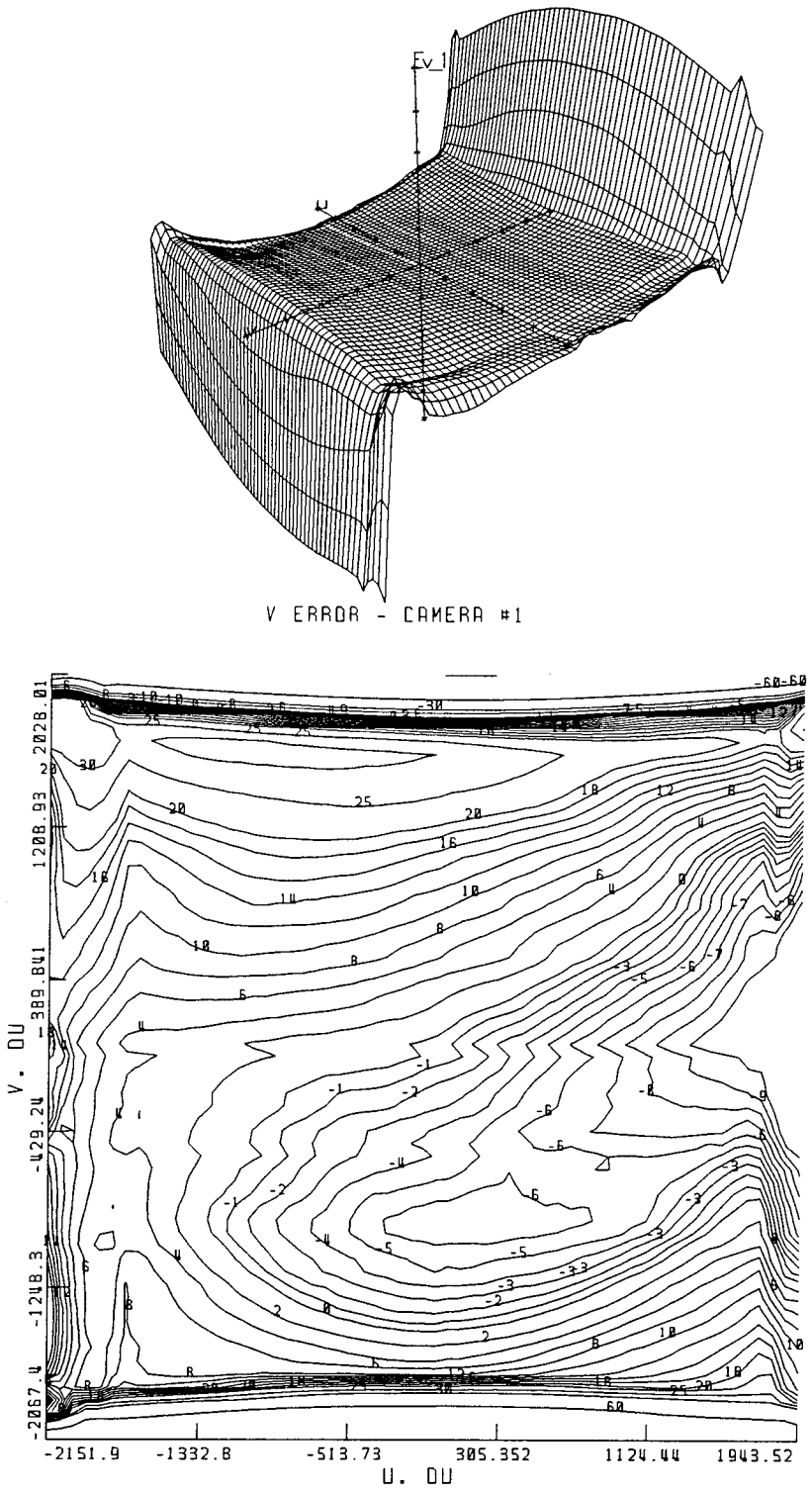

Figure C-2: v *error map of camera #1. The upper one shows the error surface. The lower one is the contour map.* u*: −2010.442 ∼ 1887.870 du,* v*: −1962.442 ∼ 1953.202 du,* E_{v1}*: −136.475 ∼ 163.884 du (4.20%).*

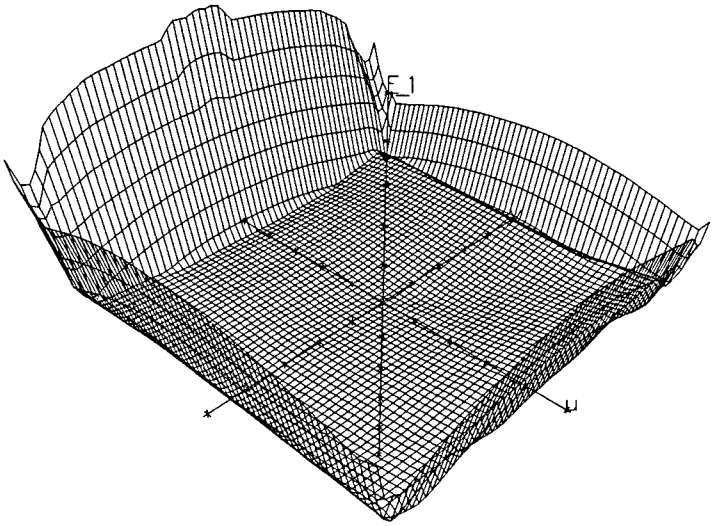

ERROR - CAMERA #1

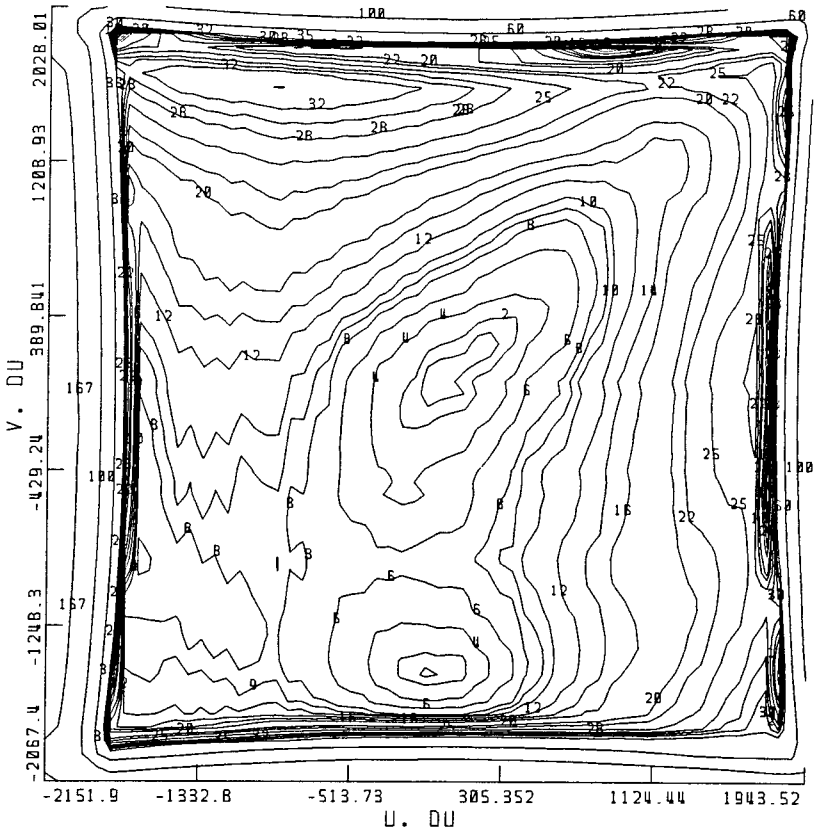

Figure C-3: Combined error map of camera #1. The upper one shows the error surface. $E = \sqrt{E_u^2 + E_v^2}$. *The lower one is the contour map.* u: $-2010.442 \sim 1887.870$ *du,* v: $-1962.442 \sim 1953.202$ *du,* E_1: $0.143 \sim 284.864$ *du.*

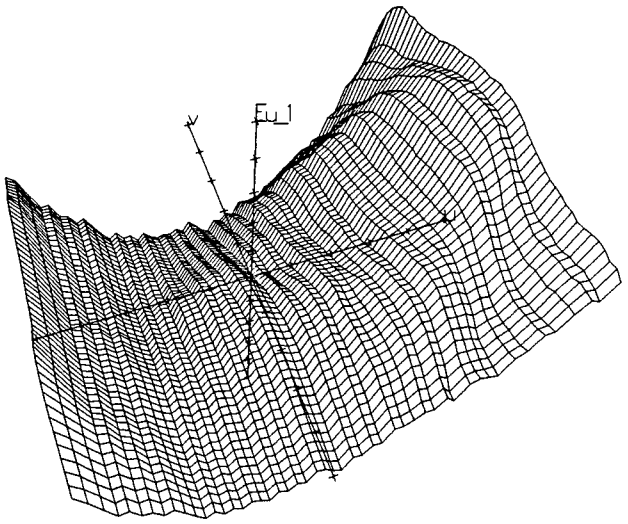

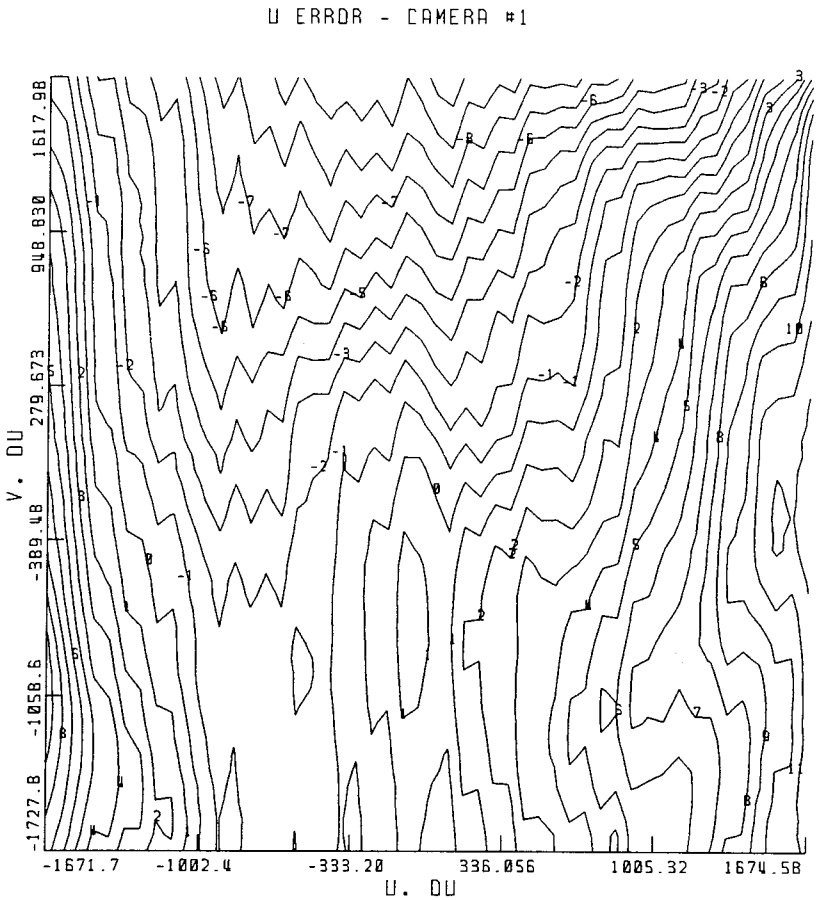

Figure C-4: Trimmed u *error map of camera #1. The upper one shows the error surface. The lower one is the contour map.* u*: −1671.268 ∼ 1722.522 du,* v*: −1706.869 ∼ 1671.679 du,* E_{u1}*: −11.071 ∼ 12.442 du (0.37%).*

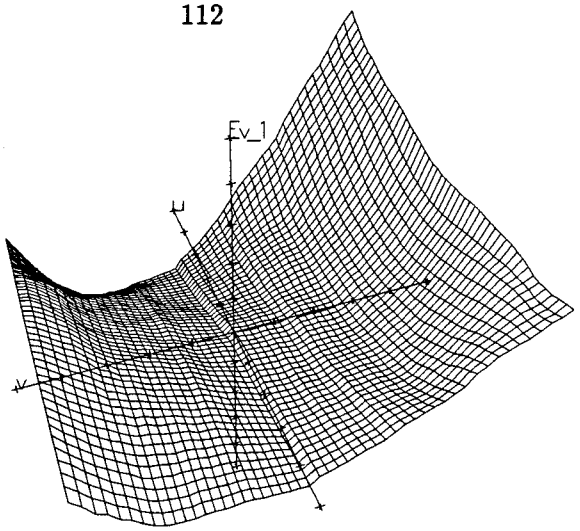

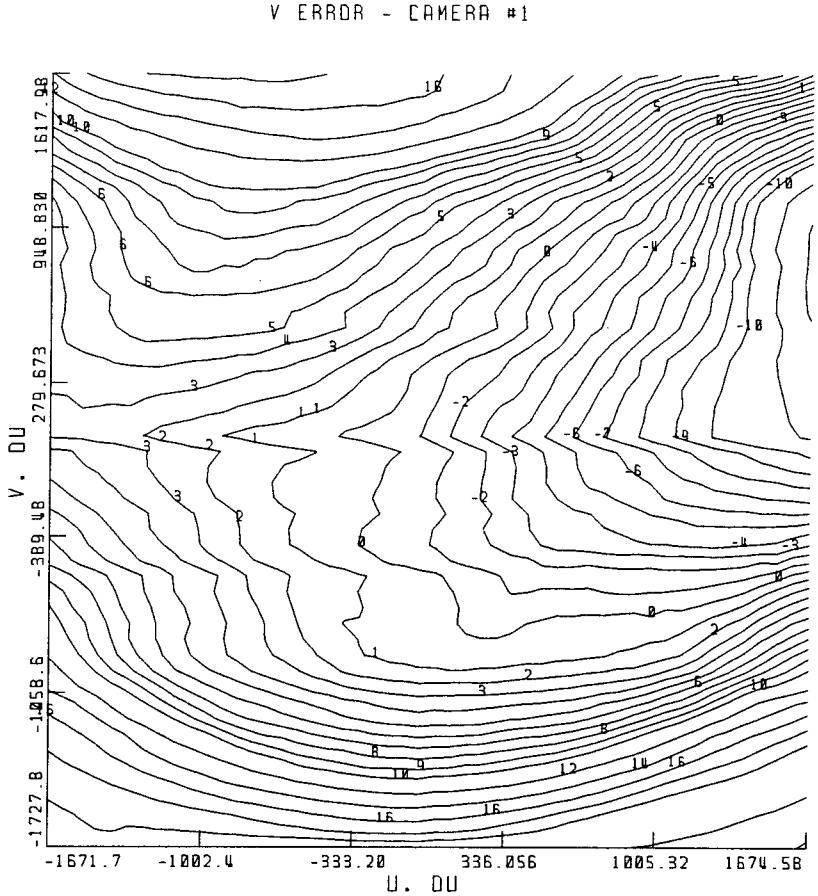

Figure C-5: Trimmed v *error map of camera #1. The upper one shows the error surface. The lower one is the contour map.* u*: −1671.268 ∼ 1722.522 du,* v*: −1706.869 ∼ 1671.679 du,* E_{v1}*: −19.625 ∼ 28.712 du (0.85%).*

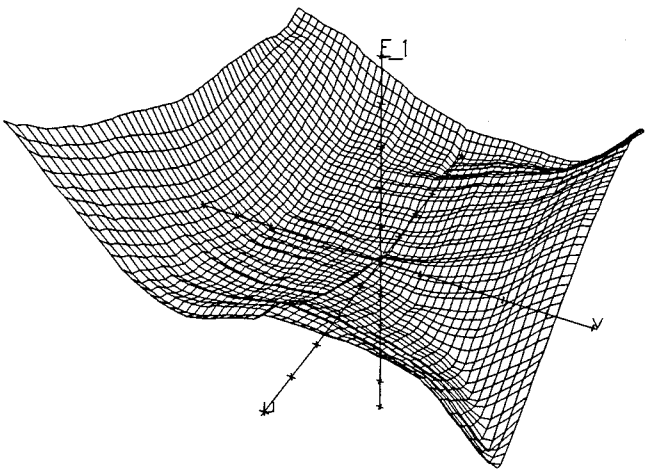

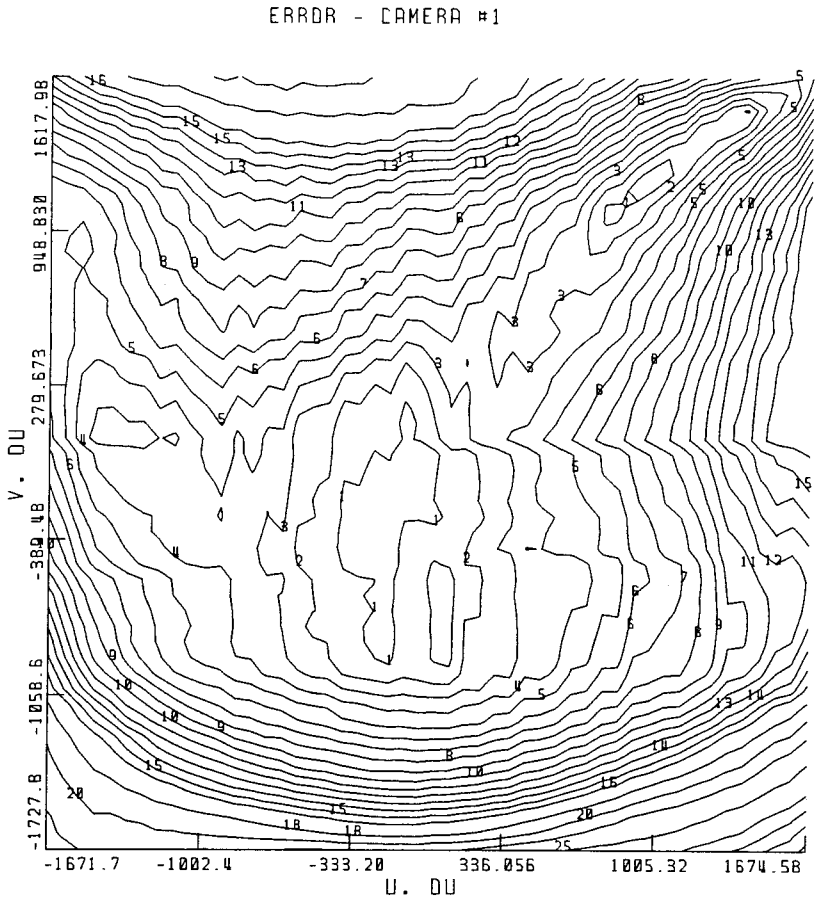

Figure C-6: Trimmed combined error map of camera #1. The upper one shows the error surface. $E = \sqrt{E_u^2 + E_v^2}$. *The lower one is the contour map.* u: $-1671.268 \sim 1722.522$ *du,* v: $-1706.869 \sim 1671.679$ *du,* E_1: $0.037 \sim 30.758$ *du.*

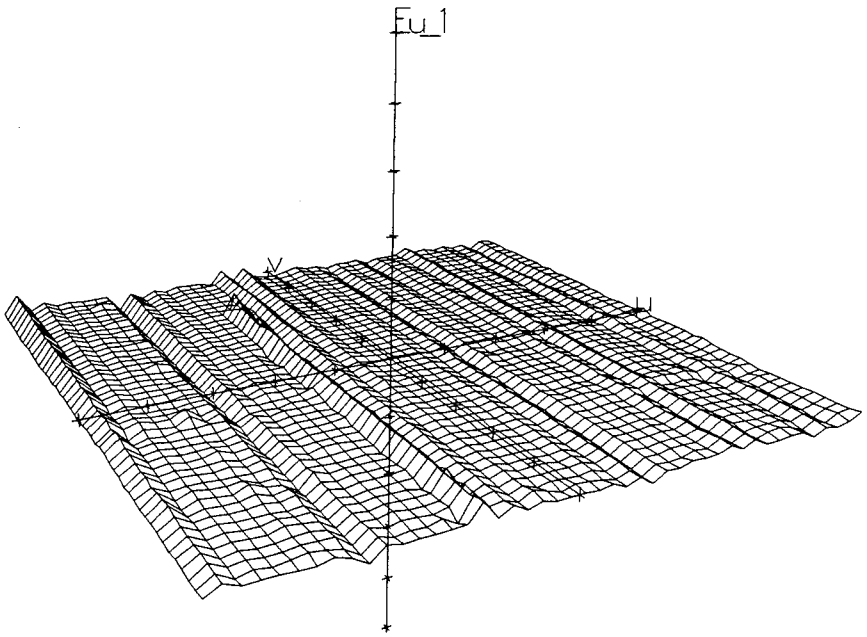

Figure C-7: Calibrated u *error surface of camera #1.* u*: −1567.349 ∼ 1545.771 du,* v*: −1572.230 ∼ 1529.715 du,* E_{u1}*: −0.886 ∼ 1.270 du (0.04%).*

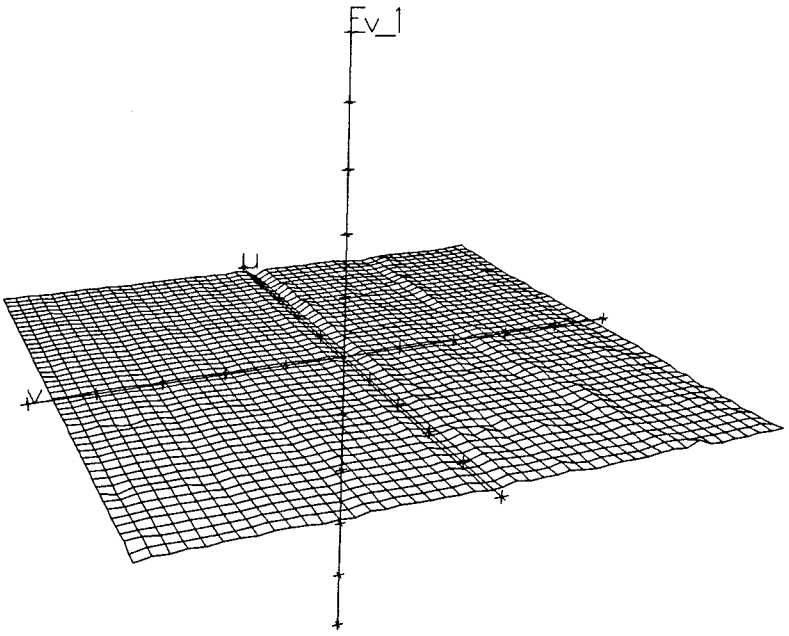

Figure C-8: Calibrated v *error surface of camera #1.* u*: −1567.349 ∼ 1545.771 du,* v*: −1572.230 ∼ 1529.715 du,* E_{v1}*: −0.987 ∼ 1.152 du (0.04%).*

Appendix D

Glossary

θ_1, θ_2: binocular convergence angles of the cameras (see Figure 2-5).

A/D converter: analog-to-digital converter.

accuracy: maximum translational or rotational error that can occur when comparing the measured quantity to the desired quantity (see Figure 3-1).

CAD/CAM: computer-aided design and computer-aided manufacturing.

CCD: charge-coupled device.

CCFOV: center of combined FOV of two cameras, intersection of the two principal axes (see Figure 2-5).

CMM: coordinate measuring machine (see Page 1).

du: detector units (see Figure 2-4).

FOV: field of view of a camera (see Figure 2-5).

inter-camera spacing: $|\vec{R}_d|$, distance between front nodes of the two camera lenses (see Figure 2-6).

LED: light-emitting diode.

LPED: lateral-photoeffect diode (see Section 2.2).

$|\vec{R}_d|$: inter-camera spacing, distance between front nodes of the two camera lenses (see Figure 2-6).

$|\vec{R}_d|/2$: length of one side of the approximately cubic viewing volume, half the inter-camera spacing (see Figure 3-2).

repeatability: difference between the maximum and the minimum measured values (see Figure 3-1).

resolution: smallest step a system can measure (see Figure 3-1 and Section 3.1.4).

SGA system: the surface geometry acquisition system being proposed in this thesis.

sampling frequency: the rate at which detectors take measurements.

sampling speed: product of the sampling frequency and the number of samples taken for each stationary light spot.

stand-off distance: distance between the two cameras and the object that gives the best resolution, distance between the CCFOV and the X-axis (see Figure 2-5).

system speed: number of data points corresponding to different surface locations acquired by the SGA system per second.

u,v: 2-D image plane coordinates (see Figure 2-3).

viewing volume: intersection of the two cameras' FOVs (combined FOV), approximated by a cube (see Figure 3-2).

X,Y,Z: 3-D world coordinates (see Figure 2-5).

X′,Y′,Z′: 3-D coordinate system attached on the object to be measured or the plane of parameterization.

References

[1] D. Allen, I. Weiman, and J. Winslow. Radiation tracking transducer. *IRE Trans. Instrumentation*, pages 336–341, December 1960.

[2] D. A. Allen. An analysis of the radiation tracking transducer. *IRE Trans. Electron Devices*, ED-9:411–416, September 1962.

[3] E. K. Antonsson. *A Three-Dimensional Kinematic Acquisition and Intersegmental Dynamic Analysis System for Human Motion.* Ph.D. thesis, Massachusetts Institute of Technology, Cambridge, Massachusetts 02139, June 1982. Department of Mechanical Engineering.

[4] E. K. Antonsson. 3-D surface geometry measurement and analysis. Engineering Design Research Laboratory Report EDRL-TR 90b, California Institute of Technology, Pasadena, California 91125, 1990.

[5] E. K. Antonsson. Apparatus for measuring three-dimensional surface geometries. Application filed January, 1989. Patent number 4,957,369, September 1990.

[6] E. K. Antonsson and R. W. Mann. Automatic 6-D.O.F. kinematic trajectory acquisition and analysis. *ASME Journal of Dynamic Systems, Measurement and Control*, 111(1):31–39, March 1989.

[7] ASME. *Methods for performance evaluation of coordinate measuring machines*, volume B89.1.12M-1990. ASME, New York, 1990. American National Standard.

[8] P. J. Besl. Active, optical range imaging sensors. *Machine Vision and Applications*, 1(2):127–152, March 1989.

[9] P. J. Besl. *The free-form surface matching problem*, pages 25–71. Academic Press, New York, 1990. H. Freeman editor.

[10] B. Bhanu. Representation and shape matching of 3-D objects. *IEEE Trans. PAMI*, 6(3):340–351, May 1984.

[11] J. G. Broerman. Nonlinear background-to-signal coupling in lateral photoeffects. *IEEE Trans. Electron Devices*, ED-15(11):860–864, November 1968.

[12] Brown & Sharpe, North Kingstown, Rhode Island 02852. *Coordinate Measuring Machines product information*, 1992.

[13] Yang Chen and Gérard Medioni. Object modeling by registration of multiple range images. *Image and Vision Computing*, 10(3):145–155, April 1992.

[14] W. P. Connors. Lateral photodetector operating in the fully reverse-biased mode. *IEEE Trans. Electron Devices*, ED-18(8):591–596, August 1971.

[15] Cyberware Laboratory Inc., Monterey, California 93940. *Color 3D Digitizer product information*, 1992.

[16] A. Dainis and M. Juberts. Accurate remote measurement of robot trajectory motion. In *Proc. IEEE Int. Conf. on Robotics and Automation*, pages 92–99, St. Louis, Missouri, March 1985.

[17] L. W. Davies. Semiconductor junctions as positional indicators of radiation. In *Proc. IRE Australia*, pages 509–512, August 1961.

[18] P. N. J. Dennis. *Photodetectors — An Introduction to Current Technology*, chapter 2, pages 14–24. Plenum Press, New York, 1986.

[19] Digibotics Inc., Austin, Texas 78759. *Digibotics product information*, 1992.

[20] Faro Technologies Inc., Lake Mary, Florida 32796. *Metrecom product information*, 1992.

[21] O. D. Faugeras, E. Le Bras-Mehlman, and J. D. Boissonnat. Representing stereo data with the Delaunay triangulation. *Artificial Intelligence*, 44:41–87, 1990.

[22] F. P. Ferrie and M. D. Levine. Integrating information from multiple views. In *Proc. IEEE Workshop on Comput. Vision*, pages 117–122, Miami Beach, Florida, December 1987.

[23] J. Fieret, A. Kwakernaak, and S. Middelhoek. Large linear area light-spot-position-sensitive photodiode. *Electron. Lett.*, 13(14):422–424, July 1977.

[24] C. M. Groden and J. A. Richards. On the non-uniformly illuminated p^+-n junction – I. *Solid-State Electronics*, 11:997–1004, 1968.

[25] C. M. Groden and J. A. Richards. On the non-uniformly illuminated p^+-n junction – II. *Solid-State Electronics*, 12:813–821, 1969.

[26] W.-J. Hsueh and E. K. Antonsson. An optoelectronic and photogrammetric 3-D surface geometry aquisition system. In *Proc. ASME Winter Annual Meeting on Instrumentation and Components for Mechanical Systems.* ASME, November 1992. EDRL-TR 92a.

[27] L. D. Hutcheson. Practical electro-optic deflection measurements system. *Optical Engineering*, 15(1):61–63, 1976.

[28] H. Inoue. A least squares smooth fitting for irregularly spaced data: Finite element approach using the cubic B-spline basis. *Geophysics*, 51(11):2051–2066, November 1986.

[29] D. E. Ioannou and D. Panagiotopoulos. A fine-line-spot-position (FLSP) sensitive photodetector. *IEEE Trans. Electron Devices*, ED-34(4):778–781, April 1987.

[30] R. A. Jarvis. A perspective on range finding techniques for computer vision. *IEEE Trans. Pattern Analysis and Machine Intelligence*, PAMI-5(2):122–139, March 1983.

[31] T. Kanade and H. Asada. Noncontact visual three-dimensional ranging devices. *SPIE 3-D Machine Perception*, 283:48–53, 1981.

[32] B. O. Kelly and R. I. Nemhauser. Techniques for using the position sensitivity of silicon photodetectors to provide remote machine control. In *Proc. 21st IEEE Machine Tool Conf.*, Hartford, Connecticut, 1973. Paper #C73970-11A.

[33] Peter Krzystek. Real-time photogrammetry with lateral-effect photodiodes: State of the art and recent investigations. In *Proc. Close-Range Photogrammetry Meets Machine Vision, SPIE volume 1395*, pages 30–37, Bellingham, Washington, 1990.

[34] Laser Design Inc., Minneapolis, Minnesota 55431. *Surveyor product information*, 1992.

[35] G. Lucovsky. Photoeffects in nonuniformly irradiated *p-n* junctions. *J. of Applied Physics*, 31(6):1088–1095, 1960.

[36] Saroj Manandhar. 3-d surface geometry acquisition: Developing the optical system and designing the setup. Summer undergradute research fellowship (SURF) report, California Institute of Technology, Pasadena, California 91125, 1987.

[37] P. K. Mansfield. *A Large Volume Close-Range Photogrammetric System.* Ph.D. thesis, Massachusetts Institute of Technology, Cambridge, Massachusetts 02139, 1990.

[38] M. Merriam and T. Barth. 3D CFD in a day: The laser digitizer project. In *Proc. AIAA 22nd Fluid Dynamics, Plasmadynamics & Lasers Conf.*, June 1991. AIAA-91-1654.

[39] M. E. Mortenson. *Geometric Modeling*, chapter 2.15 and 3.18. John Wiley & Sons, New York, 1985.

[40] M. E. Mortenson. *Geometric Modeling*, chapter 7.1. John Wiley & Sons, New York, 1985.

[41] Perceptron Inc., Farmington Hills, Michigan 48335. *Lasar product information*, 1992.

[42] M. Potmesil. Generating models for solid objects by matching 3D surface segments. In *Proc. Int. Joint Conf. on Artif. Intell.*, pages 1089–1093, Karlsruhe, Germany, August 1983.

[43] F. Preparata and M. I. Shamos. *Computational Geometry: An Introduction.* Springer-Verlag, New York, 1986.

[44] B. Scheffer. Geometric control and calibration method of an industrial robot. In *12th Int. Symp. on Industrial Robots, 6th Int. Conf. on Industrial Robot Technology*, pages 331–339, Paris, France, June 1982.

[45] W. Schottky. Über den entstehungsort der photoelektronen in kupfer-kupferoxydul-photozellen. *Physikalische Zeitschrift*, 31(21):913–925, November 1930. Leipzig.

[46] S. S. Sinha and B. G. Schunck. A two stage algorithm for discontinuity-preserving surface reconstruction. *IEEE Trans. Pattern Analysis and Machine Intelligence*, 14(1):36–55, January 1992.

[47] A. H. Slocum. *Precision Machine Design*, chapter 2, pages 58–60. Prentice Hall, New Jersey, 1992.

[48] UBM Corporation, Rochelle, Illinois 61068. *Optical Surface Measurement Station technical information*, 1992.

[49] B. C. Vemuri and J. K. Aggarwal. 3-D model construction from multiple views using range and intensity data. In *Proc. Conf. on Comput. Vision & Pattern Recogn.*, pages 435–437, Miami Beach, FL, 1986.

[50] J. T. Wallmark. A new semi-conductor photocell using lateral photoeffect. In *Proc. IRE 45*, pages 474–484, 1957.

[51] H. J. Woltring. New possibilities for human motion studies by real-time light spot position measurement. *Biotelemetry*, 1:132–146, 1974.

[52] H. J. Woltring. Single- and dual- axis lateral photodetectors of rectangular shape. *IEEE Trans. Electron Devices*, ED-22:581–590, and 1101, August 1975.

[53] Wyko Corporation, Tucson, Arizona 85706. *Rough Surface Tester product information*, 1992.

[54] Zygo Corporation, Middlefield, Connecticut 06455. *Noncontact Surface Profiler product information*, 1992.